AEROSPACE REPORT NO.
ATR-2002(8407)-1

Detection and Quantification of Gases in Industrial-Stack Plumes Using Thermal-Infrared Hyperspectral Imaging

10 February 2002

Prepared by

S. J. YOUNG
Space Science Applications Laboratory
Laboratory Operations

Prepared for

VICE PRESIDENT
Laboratory Operations

Engineering and Technology Group

PUBLIC RELEASE IS AUTHORIZED

THE AEROSPACE CORPORATION
El Segundo, California

LABORATORY OPERATIONS

The Aerospace Corporation functions as an "architect-engineer" for national security programs, specializing in advanced military space systems. The Corporation's Laboratory Operations supports the effective and timely development and operation of national security systems through scientific research and the application of advanced technology. Vital to the success of the Corporation is the technical staff's wide-ranging expertise and its ability to stay abreast of new technological developments and program support issues associated with rapidly evolving space systems. Contributing capabilities are provided by these individual organizations:

Electronics and Photonics Laboratory: Microelectronics, VLSI reliability, failure analysis, solid-state device physics, compound semiconductors, radiation effects, infrared and CCD detector devices, data storage and display technologies; lasers and electro-optics, solid state laser design, micro-optics, optical communications, and fiber optic sensors; atomic frequency standards, applied laser spectroscopy, laser chemistry, atmospheric propagation and beam control, LIDAR/LADAR remote sensing; solar cell and array testing and evaluation, battery electrochemistry, battery testing and evaluation.

Space Materials Laboratory: Evaluation and characterizations of new materials and processing techniques: metals, alloys, ceramics, polymers, thin films, and composites; development of advanced deposition processes; nondestructive evaluation, component failure analysis and reliability; structural mechanics, fracture mechanics, and stress corrosion; analysis and evaluation of materials at cryogenic and elevated temperatures; launch vehicle fluid mechanics, heat transfer and flight dynamics; aerothermodynamics; chemical and electric propulsion; environmental chemistry; combustion processes; space environment effects on materials, hardening and vulnerability assessment; contamination, thermal and structural control; lubrication and surface phenomena.

Space Science Applications Laboratory: Magnetospheric, auroral and cosmic ray physics, wave-particle interactions, magnetospheric plasma waves; atmospheric and ionospheric physics, density and composition of the upper atmosphere, remote sensing using atmospheric radiation; solar physics, infrared astronomy, infrared signature analysis; infrared surveillance, imaging, remote sensing, and hyperspectral imaging; effects of solar activity, magnetic storms and nuclear explosions on the Earth's atmosphere, ionosphere and magnetosphere; effects of electromagnetic and particulate radiations on space systems; space instrumentation, design fabrication and test; environmental chemistry, trace detection; atmospheric chemical reactions, atmospheric optics, light scattering, state-specific chemical reactions and radiative signatures of missile plumes.

Center for Microtechnology: Microelectromechanical systems (MEMS) for space applications; assessment of microtechnology space applications; laser micromachining; laser-surface physical and chemical interactions; micropropulsion; micro- and nanosatellite mission analysis; intelligent microinstruments for monitoring space and launch system environments.

Office of Spectral Applications: Multispectral and hyperspectral sensor development; data analysis and algorithm development; applications of multispectral and hyperspectral imagery to defense, civil space, commercial, and environmental missions.

AEROSPACE REPORT NO.
ATR-2002(8407)-1

DETECTION AND QUANTIFICATION OF GASES IN INDUSTRIAL-STACK PLUMES USING THERMAL-INFRARED HYPERSPECTRAL IMAGING

Prepared by

S. J. YOUNG
Space Science Applications Laboratory
Laboratory Operations

10 February 2002

Engineering and Technology Group
THE AEROSPACE CORPORATION
El Segundo, CA 90245-4691

Prepared for

VICE PRESIDENT
Laboratory Operations

PUBLIC RELEASE IS AUTHORIZED

AEROSPACE REPORT NO.
ATR-2002(8407)-1

DETECTION AND QUANTIFICATION OF GASES IN INDUSTRIAL-STACK PLUMES USING THERMAL-INFRARED HYPERSPECTRAL IMAGING

Prepared

S. J. Young
Remote Sensing Department

Approved

D. W. Pack, Director
Remote Sensing Department
Space Science Applications Laboratory

J. A. Hackwell, Principal Director
Space Science Applications Laboratory
Laboratory Operations

Abstract

Measurements of effluent gases in the plumes of hot industrial emission stacks are reported. Overhead data were collected on a refinery using the SEBASS (Spatially Enhanced Broadband Array Spectrograph System) thermal-infrared, hyperspectral imaging sensor. Ammonia, sulfur dioxide, ethylene, methane, water vapor, carbon dioxide, and nitrogen dioxide were identified in the imagery. Methods of data analysis are formulated and demonstrated. Principal-component projection and spectral matched filtering are used for detection. Principal-component projections constructed from the spectral clutter covariance matrix of the data are superior to projections constructed from correlation or noise-adjusted matrices in revealing plume activity. Linear least-squares regressions are used for quantitative gas analysis. The regression model is formulated as a linear expansion of pixel spectra in terms of gas-absorption spectra and a basis set of background spectra. The absorption spectra for water vapor, carbon dioxide, and methane are adjusted to account for line correlation between the plume emission and atmospheric attenuation spectra. Basis sets of mean cluster spectra are used in most of the analyses. A fast, single-pass clustering algorithm with a single adjustable parameter is formulated. It forgoes the minimization of the total within-cluster sum-of-squares implemented in clustering algorithms such as K-Means or ISODATA. Basis sets consisting of eigenvectors of the scene clutter covariance matrix are also investigated. Basis sets constructed with endmember extraction algorithms are not considered owing to the current inability of these algorithms to handle thermal variation in the data. Unconstrained regression is shown to be inadequate for quantitative estimation of gas concentration. Underpredictions up to a factor of ~3 are obtained for some gases. The failing of unconstrained regression is its unbridled power to fabricate unrealistic emission spectra for the surface underlying the plume. Quantitative results are obtained with constrained regression in which all gas contrast radiance coefficients are required to have the same sign, and the background basis set is required to consist of physically meaningful spectra represented by non-negative expansion coefficients. Statistical tests are used to assess the significance of all gas measurements. A method is formulated to extract gas column density and plume temperature from the gas contrast radiance. The method employs a spatial degradation of the data to circumvent the indeterminacy inherent to the problem. Downwind variations of ammonia column density and plume temperature for the largest plume at the site are fit to a simple cone-expansion plume model to extract the ammonia flow rate. Estimated concentrations for carbon dioxide and water vapor within the plume are 900 ± 400 and 21000 ± 6000 ppm, respectively. These values account for both stack emission and entrainment of ambient air. Nitrogen dioxide, ammonia, sulfur dioxide, ethylene, and methane are detected at concentrations of order 0.1 to 10 ppm.

Acknowledgment

High-resolution gas absorption spectra were obtained from Dr. Steven W. Sharpe of the Pacific Northwest National Laboratory (PNNL). Measurement of these spectra was funded by the Department of Energy (DOE). SEBASS data were collected under the direction of Eric Keim. The following people reviewed all or portions of the manuscript: Kevin Mitchell, Kerry Buckland, Niel Schulenburg, Carlton Nealy, Carl Rice, and John Hackwell.

Contents

1. Introduction 1
2. Data Collection 3
3. Gas Spectra 7
4. Radiance Model 11
   - 4.1 Derivation 11
   - 4.2 Spectral Correlation 13
   - 4.3 Atmospheric Compensation 17
5. Detection Analyses 21
   - 5.1 Principal Components 21
   - 5.2 Spectral Matched Filtering 23
6. Regression Analyses 29
   - 6.1 Manual Background Selection 30
   - 6.2 Background Endmember Extraction 31
   - 6.3 Background Cluster Construction 31
   - 6.4 Eigenvectors as Background Basis Functions 35
   - 6.5 Spectral Extractions 36
   - 6.6 Significance Tests 41
   - 6.7 Pixel Amalgamation 45
   - 6.8 Column Density and Plume Temperature Extraction 50
   - 6.9 Plume Gas Properties 53
7. Summary and Discussions 57

References 61

Appendix 1—Linear Least-Squares Regression 65

Appendix 2—Statistical Tests of Regression 73

Figures

1. Temperature dependence of carbon dioxide, water vapor, and nitrogen dioxide spectral absorption coefficients. 8
2. Spectral absorption coefficients for ammonia, methane, sulfur dioxide, and ethylene 8
3. Spectral absorption coefficients for water vapor, carbon dioxide, nitrous oxide, and nitrogen dioxide 9
4. Effective spectral absorption coefficients for water vapor. 16
5. Effective spectral absorption coefficients for carbon dioxide. 16
6. Atmospheric compensation spectra obtained with ISAC for Shot 96 17
7. Example compensation of a graybody pixel spectrum from Shot 96. 18
8. Plume detection in Shot 6 22
9. Plume spectra from Shot 6 23
10. Ethylene spectra in Shot 6 24
11. Spectral matched filter detection images for shots 76, 83, and 96 25
12. Unconstrained regression detection of ammonia in Shot 96 26
13. Methane spectra in Shot 83 27
14. Basis set of 15 manually-selected backgrounds from Shot 96 30
15. $(OP)^2$ Clustering Algorithm. 32
16. Variation of number of clusters and regression residual with cluster dispersion parameter θ for Shot 96. 32
17. Variation of cluster population distribution with cluster dispersion parameter θ for Shot 96. 33
18. $(OP)^2$ mean cluster spectra for $\theta = 85$ μf in Shot 96. 33
19. K-Means clusters obtained with the $(OP)^2$ clusters for $\theta = 85$ μf as the initiating clusters 34
20. Eigenvector expansion coefficients for ammonia spectral absorption coefficient. 35

21. Off-plume background subtraction on a single pixel in Plume 4 of Shot 96 37

22. Unconstrained regression on a single pixel in Plume 4 of Shot 96 39

23. Constrained regression on a single pixel in Plume 4 of Shot 96 40

24. Unconstrained regression on a single pixel in Plume 4 of Shot 96 with no target gases included in the regression 40

25. onstrained regression on a single pixel in Plume 4 of Shot 96 with no target gases included in the regression 41

26. Cumulative probability distributions in unconstrained regression on a single pixel in Plume 4 of Shot 96 42

27. Cumulative probability distributions in constrained regression on a single pixel in Plume 4 of Shot 96 42

28. Cluster analysis regions for Shot 83 47

29. Pixel amalgamation on Plume 1 of Shot 83 using unconstrained regression 48

30. Pixel amalgamation on Plume 1 of Shot 83 using constrained regression 50

31. Gas contrast versus underlying surface radiance for a 7 x 7 spatial region around a selected example pixel in Plume 1 of Shot 96 52

32. Spectra within a 7 x 7 sub-region around example pixel in Plume 1 of Shot 96 52

33. Ammonia column-density and plume-temperature extractions for Shot 96 53

34. Downwind variation of ammonia mean column density and mean plume temperature across the transverse dimension of Plume 1 in Shot 96 54

35. Cone-Dispersion Plume Model. 55

Tables

1. SEBASS Refinery Collection Summary 4

2. Characteristic Gas Absorption and Detection Parameters 7

3. Spectral Correlation Parameters and Results 15

4. Single-Pixel Contrast Coefficients for Plume 4 in Shot 96 38

5. Absorption Spectra Correlation Matrix 43

6. Test for Significant Gases in Constrained Regression for Plume 4 in Shot 96 44

7. Test for Significant Gases in Unconstrained Regression for Plume 4 in Shot 96 44

8. Test for Significant Background Basis Functions in Regressions for Plume 4 in Shot 96... 45

9. Pixel Amalgamation Contrast Coefficients for Plume 1 in Shot 83 49

10. Gas Concentrations in Plume 1 56

43
44
44
45
49
56

1. Introduction

Hyperspectral imaging in the mid-wave infrared (MWIR) and long-wave infrared (LWIR) atmospheric window bands provides the capability for remote sensing of both the spatial distribution of gas plumes and the identification of trace gases within the plumes. Measurements of effluent gases in the plumes of hot emission stacks are reported here. Data were collected with the SEBASS (Spatially Enhanced Broadband Array Spectrograph System) hyperspectral imaging spectrometer owned and operated by The Aerospace Corporation. A series of overhead collections was made in the spring of 2001 as part of a corporate-funded research and development program to address the issue of anthropogenic point-source emission of carbon dioxide in analysis of natural carbon-cycle data. This report establishes the general capabilities of plume gas detection in hyperspectral imagery by applying various analysis methods to data collected on a commercial refinery. Eight regions of hot-stack plume activity within the refinery imagery were investigated. Ammonia, sulfur dioxide, ethylene, water vapor, carbon dioxide, methane, nitrogen dioxide, and (possibly) nitrous oxide were detected.

Measurement of trace gases in plumes using passive, non-imaging spectroscopy at hyperspectral resolution ($\Delta\lambda$ ~0.01 to ~0.1 μm) is well established. *Carlson et al.* [1988] and *Polak et al.* [1995] cite several investigations. Thermal-infrared imaging of gas plumes at resolutions ranging from single-band radiometry to hyperspectral resolution has been reported. *Bennett et al.* [1995] report full hyperspectral imaging of ammonia and sulfur hexafluoride in a hot-stack plume viewed against both sky and terrestrial backgrounds. *Gittins and Marinelli* [1998] and *Marinelli et al.* [1999] report imaging of sulfur hexafluoride and dimethyl methylphosphonate using Fabry-Perot etalon spectroradiometry. Gas-correlation spectroscopy has been employed to image methane, nitrous-oxide, and carbon-dioxide flows [*Sandsten et al.*, 1996] and fugitive releases of ammonia, ethylene, and methane [*Edner et al.*, 1999 and *Sandsten et al.*, 2000]. Other reports of gas plume imaging, or analysis of measured imagery, are made by *Carr et al.* [1990], *Carter et al.* [1993], *Althouse and Chang* [1995], *Lisowski and Cook* [1996], *Kulp et al.* [1997], *Hinnrichs* [2000], *Lucey et al.* [2000], *Ifarraguerri and Chang* [2000] and *Kuo et al.* [2000].

A description of the sensor and summary information on the refinery data collections are provided in Section 2. Gas absorption spectra are presented in Section 3. The spectral radiance model used in the study is derived in Section 4. The model is a linear expansion of pixel radiance spectra in terms of gas absorption spectra and a basis set of background spectra. Accounts of spectral correlation effects and atmospheric compensation are also treated in Section 4. Detection of plumes using principal-component projections and spectral matched filtering is presented in Section 5. Detection and quantification of plume gases using linear least-squares regression are presented in Section 6. Both unconstrained and constrained regressions are considered. Regression implementations are discussed in Appendix 1. Regressions were performed on the spectral radiance model described in Section 4. Example analyses are presented using background basis sets consisting of spectra drawn directly from the imagery, cluster spectra constructed from the imagery, and eigenvectors of the spectral clutter covariance matrix. The inability of current endmember extraction algorithms to pro-

vide a suitable basis set is addressed. Statistical test results that assess the significance of gas detections are presented. These tests are discussed in Appendix 2. Quantitative estimates are presented for gas flow rates and concentrations. A summary of results and added discussions are provided in Section 7.

A finding of this study is that unconstrained regression cannot be trusted to provide quantitative information on plume gases. The recommended method for quantitative analysis is constrained regression in which all gas contrast coefficients are required to have the same sign, and the background basis set is required to consist of physically meaningful spectra (*e.g.*, not eigenvectors) represented by non-negative expansion coefficients. Single-pass clustering, without within-cluster minimization, provides a practical method for constructing a basis set of background spectra.

2. Data Collection

Data were collected on a commercial refinery with the SEBASS hyperspectral imaging spectrometer. The sensor was mounted in a Twin Otter aircraft and configured for nadir viewing. The instrument operates simultaneously in the MWIR atmospheric window band from ~2.9 to ~5.2 μm and in the LWIR window band from ~7.5 to ~13.6 μm. The spectral resolution is ~0.025 μm in the MWIR and ~0.05 μm in the LWIR. Only the LWIR data were used in the current study. The spectrometer is discussed by *Warren et al.* [1997]. Its use in aircraft collections is discussed by *Hackwell et al.* [1996], *Collins et al.* [1997], and *Young et al.* [2002]. Briefly, a collection is carried out by scanning the projection of the instrument entrance slit along the ground with the aircraft motion (pushbroom mode). The slit projection is perpendicular to the flight direction. This motion provides spatial information in the flight *scan* direction. A prism-dispersed image of the slit is focused onto two 128 × 128 focal-plane arrays—one for each window band. One dimension of an array provides the *cross-scan* spatial information along the slit direction; the other dimension provides the spectral information. For these collections, the last four spectral channels of the LWIR array were not operational. The spectral span of the data is 7.67 to 13.42 μm in $J = 124$ spectral channels. The angular resolution of the instrument is 1.1 mrad per pixel. The aircraft altitude was ~6000 ft (~2000 m) above the collection site. The ground sample distance in the cross-scan direction is then GSD_X ~2 m. The focal-plane arrays were operated at 244 frames per second. Sequential frames were coadded so that the ground sample distance in the scan direction (GSD_S) was approximately the same as GSD_X. The data comprise a three-dimensional *datacube* that may be envisioned either as a set of J images or as a collection of spectra arranged into an image.

Radiometric calibration was made against blackbody sources. Calibration data were collected inflight immediately before and after each collection run across the target site. A standard wavelength calibration was made against a set of polymer films. In these collections, ammonia is present in all of the imagery. The sharp spectral features of this gas (see Section 3) provided the opportunity to adjust the wavelength calibration to even higher accuracy than obtained with the polymer films. Using unconstrained regressions for ammonia contrast coefficients, the wavelength array was adjusted until the residuals of the regressions were minimized. The adjustment was a simple translation and scaling of the form

$$\lambda(j) = A + B\lambda_0(j) \qquad j = 1,2,\ldots,J\ , \tag{1}$$

where $\lambda_0(j)$ is the polymer film calibration. The net effect was a modest upward shift of the spectral channel centers by ~0.034 μm at $j = 1$ and ~0.014 μm at $j = 124$. The mean regression residual across the spectrum was decreased by a factor of ~2 to 3, but the decrease near some of the peaks in the residual spectrum was more than 2 orders of magnitude. The transformed array (1) was used for all of the results reported here.

The working unit of spectral radiance for the SEBASS sensor is $\mu W/cm^2/sr/\mu m = 0.01\ W/m^2/sr/\mu m$ and is denoted in this report by the symbol μf. Radiance spectra are displayed as *brightness temperature* spectra. The Planck radiation function is

$$B(\lambda,T)=\frac{c_1}{\lambda^5\left(e^{c_2/\lambda T}-1\right)}, \tag{2}$$

where $c_1 = 1.191 \times 10^{10}$ μf-μm^5 and $c_2 = 14388$ μm-K are the first and second radiation constants. The brightness temperature spectrum for a radiance spectrum $L(\lambda)$ is obtained from the inverse Planck function by

$$T_B(\lambda)=\frac{c_2}{\lambda \ln\left(1+\frac{c_1}{\lambda^5 L(\lambda)}\right)}. \tag{3}$$

(For calculations, temperature is in K. Reported values are in °C.) Spectral subtleties are more readily apparent in brightness temperature spectra than in radiance spectra. In addition to conversion between radiance and temperature, some analyses require conversion between radiance and temperature differences (*e.g.*, radiance contrasts and radiance error estimates). This conversion for any variable ΔX is

$$\Delta X_{\mathrm{K}} = \frac{\Delta X_{\mu\mathrm{f}}}{\partial B/\partial T}, \tag{4}$$

where

$$\frac{\partial B(\lambda,T)}{\partial T} = B(\lambda,T)\left(\frac{c_2}{\lambda T^2}\right)\left(1-e^{-c_2/\lambda T}\right)^{-1}. \tag{5}$$

Collection parameters are summarized in Table 1. All collections were made in mid to late afternoon, local time. Collections are identified in the text by Shot number. *Frames* is the number of pixel image rows in the scan direction. The number of pixel image columns is always 128. *NESR* is

Table 1. SEBASS Refinery Collection Summary

Date	Time (PDT)	Shot	Frames	*NESR* (μf)	T_{max} (°C)	*Z* (ft)	*GSD* (m)
3 April	17:06	6	1000	0.5	80	5400	1.8
5 April	15:23	76	500	0.7	140	6000	2.0
5 April	15:29	83	500	0.8	140	6000	2.0
5 April	15:35	96	500	0.8	140	6000	2.0

the sensor noise equivalent spectral radiance for a 310K blackbody source averaged over the focal-plane array. In anticipation of high thermal clutter at the refinery site, provisions were made for collecting with various dynamic-range settings. After reviewing the data, it was decided to use only the collections revealing the greatest thermal sensitivity near ambient temperatures. Consequently, data collected over the hottest regions of the site (generally directly over hot emission stacks) are saturated. T_{max} are the saturation temperatures. Care is taken not to use data from these regions in analysis. Z is the altitude of the sensor above the site. *GSD* is the ground sample distance (pixel footprint on the ground). No supporting ground-based data were collected at the site. Nothing is known about processes occurring at the site. Wind speed and direction at the site were estimated with the *Eta Data Assimilation System* (EDAS) [*NOAA*; *Rolph,* 1998]. These data are available only at 3-h intervals and are reported without error estimates. Nevertheless, reported wind directions are within ~30° of observed plume directions. Wind speed data are used in estimating gas flow rates.

3. Gas Spectra

Gas species considered in analysis of the data are listed in Table 2. With the exception of nitrous oxide, all of these gases were unambiguously detected within the imagery. High-resolution spectral absorption coefficients k for all of the gases except carbon dioxide and water vapor were obtained from measurements made at the Pacific Northwest National Laboratory (PNNL) (see Acknowledgments). Data were provided for a spectral resolution of 0.12 cm^{-1}, a total sample pressure of 1 atm and temperatures of 5, 25, and 50°C. The 25°C spectra were used here. High-resolution spectra for carbon dioxide and water vapor were constructed from line-strength, line-width, and partition-function parameters available in the HITRAN spectral-line database [*Rothman et al.*, 1998]. Spectra were generated on a 0.01-cm^{-1} grid and employed the Lorentzian line-shape. The reference temperature was 20°C. The total pressure was 1 atm The column-density unit employed in this study is *parts-per-million-meter* (ppmm). The unit of k is 1/ppmm.

With the exception of carbon dioxide, water vapor, and nitrogen dioxide, the spectral absorption coefficients are independent of temperature in the range relevant to this study (~15 to ~80°C). The temperature variations for carbon dioxide, water vapor, and nitrogen dioxide are shown in Figure 1. Only the magnitudes of the coefficients are affected. The shapes of the spectra are relatively insensitive to temperature. The consequence of this insensitivity is that all detection analyses can be carried out with spectra for a fixed temperature. Whatever quantitative gas results are obtained using the spectra can be scaled to their proper values once the gas temperature is determined.

The high-resolution spectra were resampled onto the shifted wavelength array (1) using a triangular slit function. The function peaks at the center of a spectral channel and falls to zero at the centers of the two adjacent channels. Resampled spectra are shown in Figures 2 and 3.

Table 2. Characteristic Gas Absorption and Detection Parameters

Species		μ (g/mole)	k_c (1/ppmm)	$\bar{\lambda}$ (μm)	$\delta\lambda$ (μm)	MDC (ppmm-μf)	MDC (ppmm-°C)
Methane	CH_4	16	1.3×10^{-4}	7.86	0.30	2.3×10^{4}	1300
Nitrous Oxide	N_2O	44	3.5×10^{-4}	7.86	0.36	8.8×10^{3}	490
Water Vapor	H_2O	18	3.6×10^{-7}	9.22	0.96	3.8×10^{6}	220000
Carbon Dioxide	CO_2	44	1.7×10^{-6}	12.94	0.39	6.6×10^{5}	63000
Nitrogen Dioxide	NO_2	46	1.5×10^{-4}	11.11	1.21	5.6×10^{3}	400
Ammonia	NH_3	17	5.1×10^{-4}	10.52	1.27	7.0×10^{2}	47
Sulfur Dioxide	SO_2	64	8.6×10^{-5}	8.85	0.92	9.9×10^{3}	560
Ethylene	C_2H_4	28	3.0×10^{-4}	10.54	1.35	6.1×10^{2}	41
Air		29					

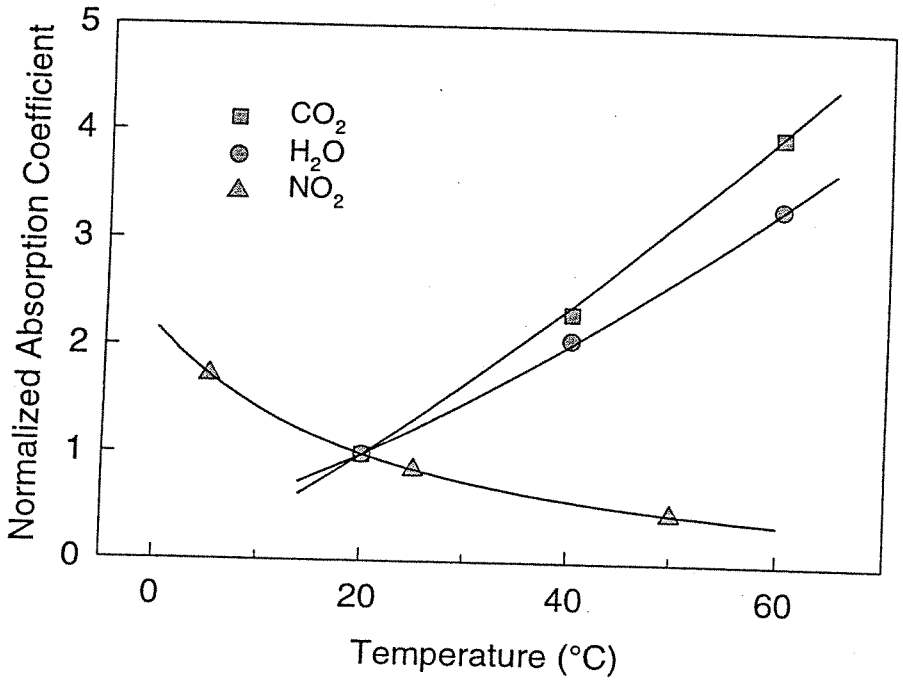

Figure 1. Temperature dependence of carbon dioxide, water vapor, and nitrogen dioxide spectral absorption coefficients.

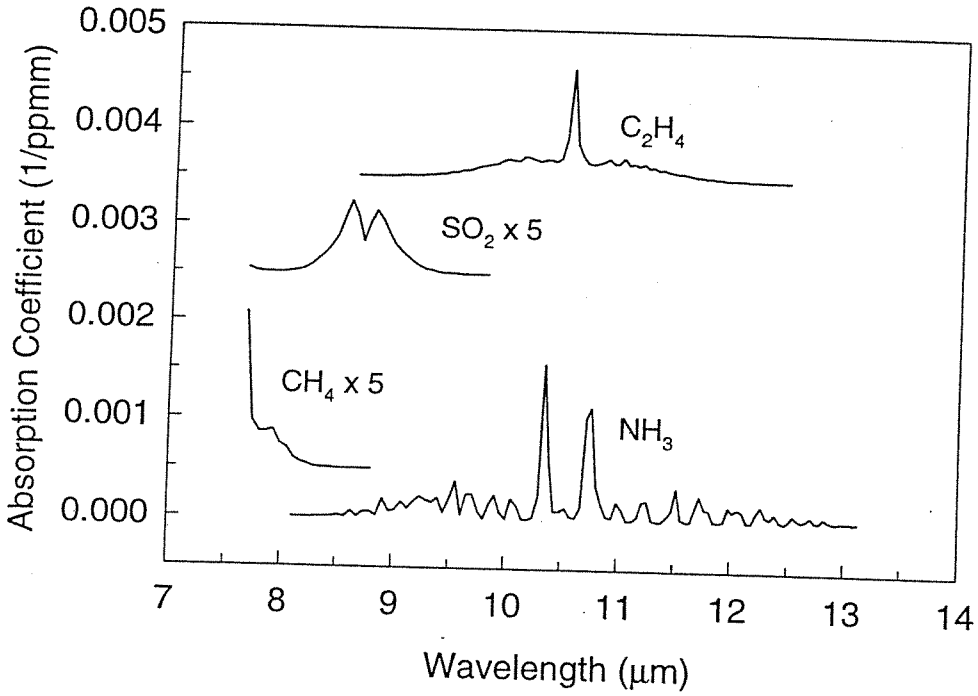

Figure 2. Spectral absorption coefficients for ammonia, methane, sulfur dioxide, and ethylene. The spectra are offset and scaled.

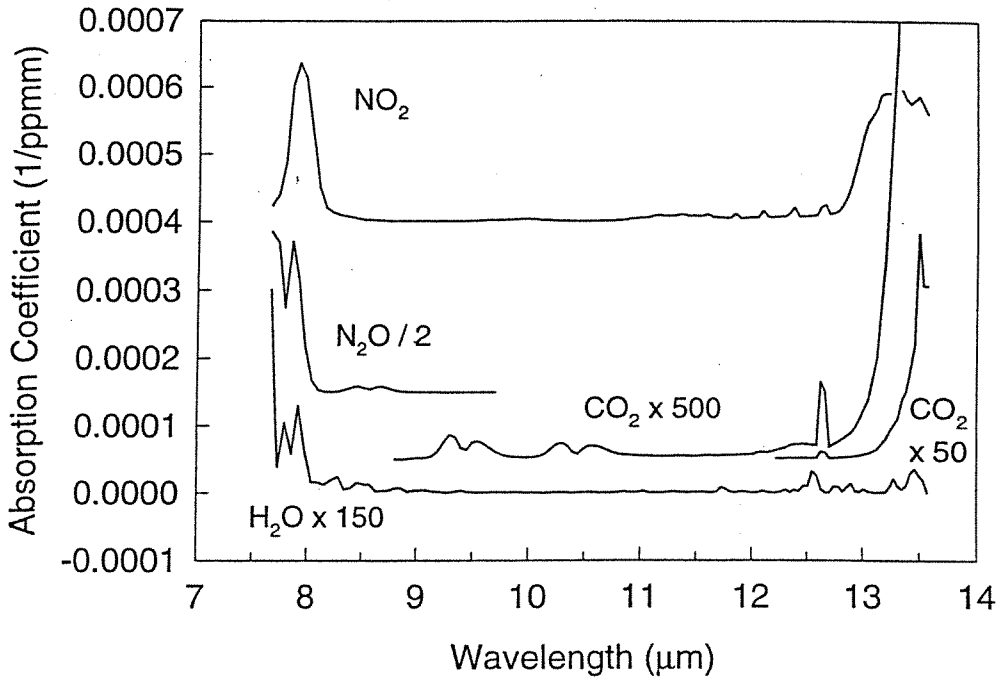

Figure 3. Spectral absorption coefficients for water vapor, carbon dioxide, nitrous oxide, and nitrogen dioxide. The spectra are offset and scaled.

A tabulation of *characteristic* absorption parameters for these gases is provided in Table 2. The parameters are defined by

$$k_C = \overline{k^2}/\overline{k} \tag{6}$$

$$\delta\lambda = W\left(\overline{k}/k_C\right) \tag{7}$$

$$\overline{\lambda} = \overline{\lambda k}/\overline{k}\,, \tag{8}$$

where k_c is a characteristic absorption strength, $\overline{\lambda}$ is a characteristic bandcenter, and $\delta\lambda$ is a characteristic bandwidth. The averaging is over the extent of the window band W (*e.g.*, 7–14 μm). An advantage of these particular definitions over other possible definitions is that they are relatively insensitive to W so long as it is sensibly chosen. These parameters are useful in making estimates of relative absorption effects among gases. Note that the characteristic bandcenter (8) does not necessarily coincide with the position of peak absorption if the spectrum is not unimodal. The bandcenter parameter is discussed further in the next section. The *MDC* entries in the table are the minimum gas contrasts likely to be detectable against the clutter inherent to the current collection site (*MDC* is defined in Appendix 1). The relationship between *MDC* expressed in radiance and temperature units is given by (4) and (5) with $T = 300$K and $\lambda = \overline{\lambda}$. The remaining column in Table 2 is atomic mass. This parameter is used later in mass flow rate analyses (Subsection 6.9).

4. Radiance Model

The spectral radiance model is derived in this section. Account of atmospheric absorption and emission effects and spectral correlation between plume emission and atmospheric attenuation spectra are addressed.

4.1 Derivation

A complete derivation of the model for observed spectral radiance in the thermal hyperspectral regime is complicated. Here, the simplest version of the model is derived that describes the significant aspects of the present application. It follows the derivation of *Hayden et al.* [1996] and involves three significant simplifications. The first simplification is the neglect of reflected downwelling atmospheric and plume radiation by the underlying surface and the neglect of reflected downwelling atmospheric radiation by the plume. The underlying surface is assumed to be a graybody with low reflectance. This is a good assumption for all ground surfaces at the current site. There are no extensive regions of silicate surfaces (natural or pavement), which can sometimes provide measurable reflection of downwelling radiation in the quartz reststrahlen band between ~8.0 and ~9.6 μm. Even most of the structures at the site are quite gray. A few structures, presumably those with metal roofs, reveal their reflective nature by the presence of reflected downwelling atmospheric ozone radiation in the 9.2 to 10.1 μm region, and water vapor radiation throughout the window band, but most noticeably near 11.7 and 12.6 μm. Care is taken not to make quantitative assessments of data taken over reflective surfaces.

With this neglect of reflected radiation, the spectral radiance at the sensor aperture when there is no plume in a pixel field of view (FOV) is

$$L_0(\lambda) = \varepsilon_S(\lambda) B_S(\lambda) \tau(\lambda) + L_u(\lambda). \tag{9}$$

Throughout the development, all spectral quantities represent mean values within a spectral channel. The first term in (9) is the radiance contribution from the surface. $\varepsilon_S(\lambda)$ is the surface emissivity, and as noted above, is assumed to be close to unity. $B_S(\lambda)$ is the Planck function (2) evaluated at the surface temperature, T_S. $\tau(\lambda)$ is the atmospheric transmission for the slant path between the sensor and the surface. The second term, $L_u(\lambda)$, is the upwelling atmospheric radiance from the slant path. The atmospheric transmission and radiance spectra are considered further in Subsection 4.3. With the additional assumptions that the temperature is constant along a line of sight (LOS) through the plume and that the plume lies close to the underlying surface, the spectral radiance at the aperture when a plume fills a pixel FOV is

$$\begin{aligned} L(\lambda) = {} & \varepsilon_S(\lambda) B_S(\lambda) \tau_P(\lambda) \tau(\lambda) + \varepsilon_P(\lambda) B_P(\lambda) \tau(\lambda) + L_u(\lambda) \\ & + \varepsilon_A [B_P(\lambda) - B_A(\lambda)] \tau(\lambda). \end{aligned} \tag{10}$$

The first term in (10) is the surface radiance attenuated by the plume transmission $\tau_P(\lambda)$. The second term is the radiance contribution from the plume. $\varepsilon_P(\lambda)$ is the plume emissivity. $B_P(\lambda)$ is the Planck function (2) evaluated at the plume temperature T_P. With the assumption that the temperature is constant along a LOS through the plume, the plume emissivity and transmittance are related by $\varepsilon_P(\lambda) = 1 - \tau_P(\lambda)$. The third term is upwelling atmospheric radiance. The last term accounts for entrainment of ambient gases into the plume, and is significant in this study only for water vapor and carbon dioxide. This particular form of the term obtains for the assumption that ambient air is rapidly entrained and uniformly mixed with stack gases. ε_A is the plume emissivity arising from the ambient-gas contribution to the plume. The factor in square brackets adjusts the radiance contribution from that given by the ambient air temperature, T_A, to that given by the plume temperature, T_P. The spectral products $\tau_P(\lambda)\tau(\lambda)$, $\varepsilon_P(\lambda)\tau(\lambda)$, and $\varepsilon_A(\lambda)\tau(\lambda)$ in (10) are discussed further in Subsection 4.2.

The *radiance contrast* spectrum is the difference between (9) and (10):

$$\Delta L(\lambda) = L(\lambda) - L_0(\lambda) =$$
$$\varepsilon_P(\lambda)[B_P(\lambda) - \varepsilon_S(\lambda)B_S(\lambda)]\tau(\lambda) + \varepsilon_A(\lambda)[B_P(\lambda) - B_A(\lambda)]\tau(\lambda). \tag{11}$$

The second major simplification is the assumption that the plume gases are optically thin. If non-thin conditions occur, they generally occur directly over hot-stack emission points where the plume is still lofting vertically and has not yet bent entirely into the wind. Far enough downwind, atmospheric dispersion will render all plumes optically thin. Again, care is taken here not to draw any quantitative conclusions from regions of a plume that are not close to optically thin conditions. The assumption of optical thinness circumvents the need to consider the form of the absorption curve-of-growth of the gases, i.e., whether the variation of $\varepsilon_P(\lambda)$ and $\varepsilon_A(\lambda)$ with optical depth is governed by Beer's Law or some narrow-band-model law. The thin-gas limit for any absorption model yields

$$\varepsilon_P(\lambda) = \sum_{n=1}^{N} c_{nP}\, k_n(\lambda) \qquad \varepsilon_A(\lambda) = \sum_{n=1}^{N} c_{nA}\, k_n(\lambda). \tag{12}$$

The summation in (12) is over all optically active gases in the plume. c_{nP} *and* c_{nA} are the stack and ambient contributions to the column density of the nth gas in the LOS. If a pixel is not completely filled with plume gas, then c_{nA} and c_{nP} are the column densities multiplied by the fractional fill factor f. $k_n(\lambda)$ is the spectral absorption coefficient for the nth gas. If gas absorption spectra overlap, the total absorption by all gases is assumed to be thin. Comments on radiance models for non-thin gases are made in Section 7.

With (11) and (12), the modeled signal at the entrance aperture with a plume in the pixel FOV becomes

$$L(\lambda) = \sum_{n=1}^{N} C_n(\lambda)\tau(\lambda)k_n(\lambda) + L_0(\lambda), \tag{13}$$

where $C_n(\lambda)$ is the *thermal contrast* spectrum for the nth gas.

$$C_n(\lambda) = c_{nP}[B_P(\lambda) - \varepsilon_S(\lambda)B_P(\lambda)] + c_{nA}[B_P(\lambda) - B_A(\lambda)]. \tag{14}$$

The third major simplification of the model is made in this thermal contrast factor. Compared to both $k_n(\lambda)$ and $\tau(\lambda)$, $C_n(\lambda)$ is a slowly varying function of λ. Its spectral variation is governed primarily by the Plank function. It is approximated by its mean spectral value in the following way:

$$C_n(\lambda) \approx C_n = c_{nP}[B_P(\bar{\lambda}_n) - \varepsilon_S(\bar{\lambda}_n)B_S(\bar{\lambda}_n)] + c_{nA}[B_P(\bar{\lambda}_n) - B_A(\bar{\lambda}_n)]. \tag{15}$$

λ_n is the wavelength that yields the best approximation to the equality for the nth gas. For this work, c_{nA} was set to zero. It was determined for a wide range of $k_n(\lambda)$ spectra, and a few $\varepsilon_S(\lambda)$ spectra (graybodies, silicate surfaces, and carbonate pavements), that $\bar{\lambda}_n$ is adequately given by

$$\bar{\lambda}_n = \overline{\lambda k_n^m} \Big/ \overline{k_n^m}. \tag{16}$$

The bar indicates an average over the full LWIR window band. In the plume temperature range T_P = 0 to 50°C and the temperature contrast range $\Delta T = T_P - T_s = -10$ to 50°C, the best-fit weighting exponent m varies from 1 to 2, although any value in this range provides an adequate approximation. When needed in the current work, $m = 1$ is used. This value of m was used previously to define the characteristic bandcenter in (8).

A consequence of (15), in the absence of ambient-gas contributions, is that if the plume temperature is equal to the surface brightness temperature, the thermal contrast is zero, and the observed radiance is just the surface radiance $L_0(\lambda)$ even though there may be considerable gas in the plume. The physical reason for this effect is that the plume gases emit exactly the same amount of radiation that they absorb from the underlying surface along the sensor LOS. This condition of *null contrast* is common in gas emission from hot stacks observed in the daytime. On exit from the stack, and as the gases just drift over surfaces adjacent to the stack, the plume temperature is higher than the underlying surface temperature, and the gases are seen in emission. As the gases cool towards the ambient air temperature, which is usually cooler than the underlying surface temperature during the day, they reach a point where their temperature equals the underlying surface brightness temperature, and the plume disappears. As the gas temperature falls further towards the ambient air temperature, the plume reappears in absorption. With ambient-gas contributions, the condition of null contrast is achieved at a temperature lower than the surface brightness temperature. If the active plume gases consist solely of entrained ambient gases, the gases remain in emission until the plume temperature falls to the ambient air temperature, T_A.

Substitution of (15) into (13) yields the final model:

$$L(\lambda) = \sum_{n=1}^{N} C_n \tau(\lambda) k_n(\lambda) + L_0(\lambda) + \delta(\lambda). \tag{17}$$

The additional term $\delta(\lambda)$ in (17) is the residual error spectrum. With the approximation (15), the radiance model becomes a linear equation.

4.2 Spectral Correlation

The model developed so far is adequate for many gas detection problems. It is deficient if the plume gases are also significant atmospheric absorbers. This condition occurs in this study for water vapor, carbon dioxide, methane, and nitrous oxide. The problem enters in (10) with the products $\tau(\lambda)\tau_P(\lambda)$, $\tau(\lambda)\varepsilon_A(\lambda)$, and $\tau(\lambda)\varepsilon_P(\lambda)$ and propagates through to the product $\tau(\lambda)k_n(\lambda)$ in (13). This latter product is considered here. The subscript n is suppressed. Both $\tau(\lambda)$ and $k(\lambda)$ are mean values in a spectral channel. To emphasize this, they will be denoted in this section by $\bar{\tau}(\lambda_j)$ and $\bar{k}(\lambda_j)$. The original symbols $\tau(\lambda)$ and $k(\lambda)$ will now denote the *monochromatic* variation within the spectral channel. The proper product to use in (13) is the mean value of the product of the monochromatic spectra $\overline{\tau(\lambda)k(\lambda)}$. The use of $\bar{\tau}(\lambda_j)\bar{k}(\lambda_j)$ is an approximation that is valid only if there is no spectral correlation between the two monochromatic spectra. However, when emission from the plume and attenuation by the atmosphere are caused by the same gas, the degree of correlation between the two spectra can be very large. This *common-gas* situation is the only one of concern. The product of spectral quantities involving different gases, or of any product of a gas spectrum with a surface emissivity or Planck spectrum, is adequately approximated by the product of mean spectra. This *multiplication property* for gas spectra is well established in the literature of radiation transport by band models [*e.g.*, *Goody*, 1964]. Band model methods for treating radiation transport under conditions of high spectral correlation have been developed [*Young*, 1977].

Account of spectral correlation is handled here by defining an *effective* spectral absorption coefficient

$$\bar{k}_e(\lambda_j) = \frac{\overline{k(\lambda)\tau(\lambda)}}{\bar{\tau}(\lambda_j)}. \tag{18}$$

The Schwartz inequality establishes that $\bar{k}_e(\lambda_j) \le \bar{k}(\lambda_j)$. The atmospheric transmission spectrum can be factored into its contributions from the gas of concern and all other atmospheric gases by

$$\tau(\lambda) = \tau_k(\lambda)\tau_{other}(\lambda). \tag{19}$$

Substitution of (19) into (18) and allowing the multiplication of mean values for dissimilar gases yields

$$\bar{k}_e(\lambda_j) = \frac{\overline{k(\lambda)\tau_k(\lambda)}}{\bar{\tau}_k(\lambda_j)}. \tag{20}$$

Finally, with

$$\tau_k(\lambda) = e^{-c_{atm}k(\lambda)}, \tag{21}$$

we have

$$\bar{k}_e(\lambda_j) = \frac{\overline{k(\lambda)\, e^{-c_{atm}k(\lambda)}}}{\overline{e^{-c_{atm}k(\lambda)}}}, \tag{22}$$

where c_{atm} is the gas column density over the atmospheric slant path. For small atmospheric column density, $\bar{k}_e(\lambda_j)$ approaches $\bar{k}(\lambda_j)$. [For very large column density, asymptotic expansion of the numerator and denominator of (22) yields $\bar{k}_e(\lambda_j) \sim k_{min}$ where k_{min} is the minimum value of $k(\lambda)$ in the spectral channel.]

Account of spectral correlation was made for water vapor, carbon dioxide, methane, and nitrous oxide. Atmospheric column densities for these species and a 6000-ft collection altitude are shown in Table 3. The water vapor value was computed from the EDAS weather data. A quite comparable value of 1.4×10^7 ppmm was obtained as part of the atmospheric compensation procedure discussed in the following section. Column densities for methane and nitrous oxide were calculated using U.S. Standard Atmosphere values for the gas mixing ratios [*U.S. Standard Atmosphere, 1976*, 1976]. The carbon dioxide mixing ratio was taken as 360 ppm. The amounts of ammonia, sulfur dioxide, nitrogen dioxide, and ethylene in the atmosphere are so small that the spectral correlation effects are negligible. The effective absorption coefficients for water vapor and carbon dioxide are shown in Figures 4 and 5. The ratio $f(\lambda) = k_e(\lambda)/k(\lambda)$ is also shown for each gas. (The bar- and subscript-notation for spectral channel average is now dropped.) The effect of spectral correlation is quite large for these gases and observation geometry. A summary of the magnitude of the effect for all gases is shown in Table 3. k_{eC} is the characteristic value of $k_e(\lambda)$ derived from (6). The ratio k_C/k_{eC} provides an estimate of the magnitude of the effect. k_C values are from Table 2. For example, without account of spectral correlation, a retrieved water-vapor concentration would be underestimated by a factor of 16. These estimates are supported by the ratio of *MDC*s calculated with and without account of correlation. The temperature dependence of $k_e(\lambda)$ for water vapor and carbon dioxide is the same as shown in Figure 1 for $k(\lambda)$.

The notation continues to use $k(\lambda)$ for gas absorption coefficient, but it is understood that $k_e(\lambda)$ is implied if spectral correlation is strong.

Table 3. Spectral Correlation Parameters and Results

Gas	c_{atm} (ppmm)	k_{eC} (ppmm^{-1})	k_C/k_{eC}	MDC_e (ppmm-°C)	MDC_e/MDC
Water Vapor	1.1×10^7	2.2×10^{-8}	16.0	2300000	10.4
Carbon Dioxide	6.2×10^5	4.5×10^{-7}	3.9	190000	3.1
Methane	3.0×10^3	5.0×10^{-5}	2.6	4800	3.7
Nitrous Oxide	5.6×10^2	2.9×10^{-4}	1.2	590	1.2

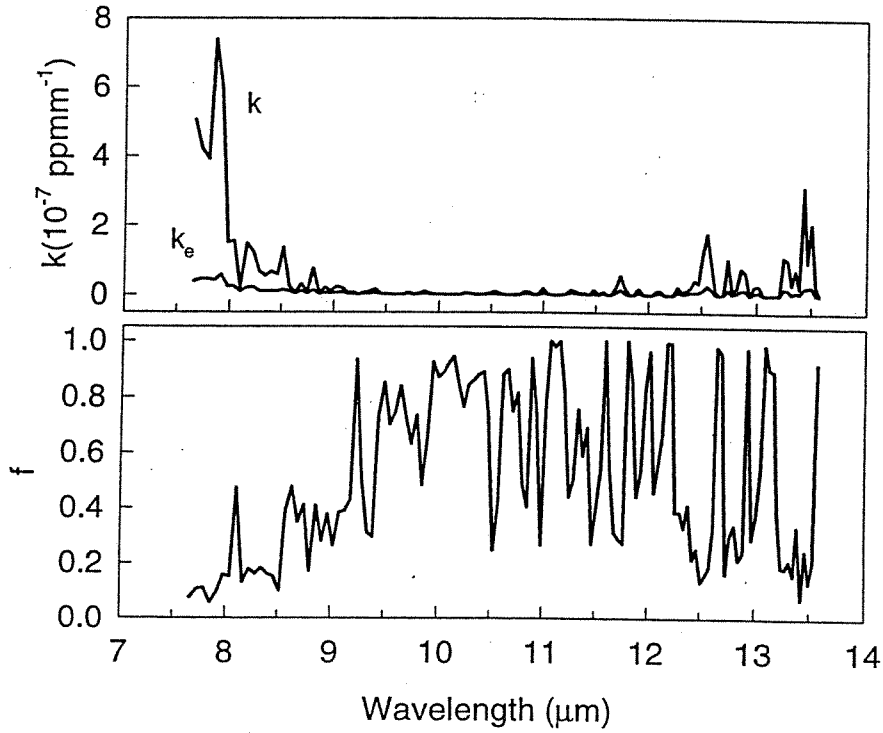

Figure 4. Effective spectral absorption coefficient for water vapor.

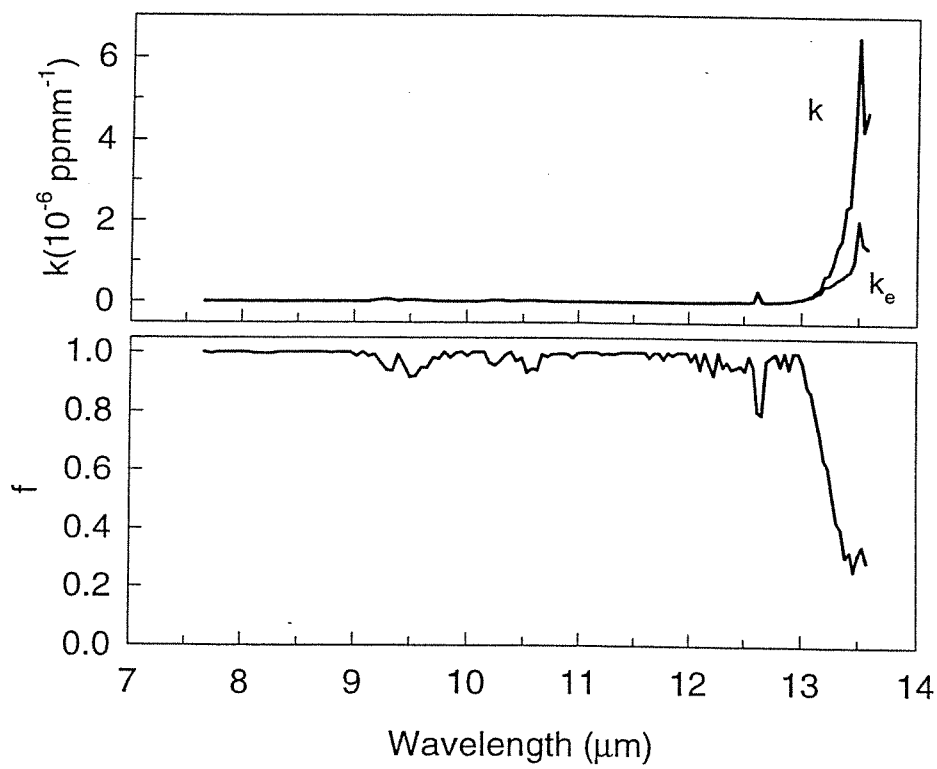

Figure 5. Effective spectral absorption coefficient for carbon dioxide.

4.3 Atmospheric Compensation

Some analyses considered here are more conveniently implemented on radiance data that have been compensated for emission and absorption effects of the atmosphere. The general form for atmospheric compensation with neglect of radiation reflected from the surface is

$$L_C(\lambda) = [L(\lambda) - L_u(\lambda)]/\tau(\lambda), \tag{23}$$

where $L_u(\lambda)$ and $\tau(\lambda)$ are the upwelling atmospheric radiance and transmittance spectra introduced in the previous section. These spectra were extracted directly from the hyperspectral radiance data without recourse to ancillary data using the ISAC (Inscene Atmospheric Compensation) algorithm described by *Young et al.* [2002]. (As part of this application, an estimate of water vapor column density is made from the degree of absorption in the 11.7-μm band. This procedure yields the column-density estimate quoted in the previous section.) Example compensation spectra derived from Shot 96 are shown in Figure 6. An example compensation of the blackest pixel in that collection is illustrated in Figure 7. (Subsequent use of the single word *compensation* or its variations will always imply *atmospheric compensation*.)

Application of (23) to (17) yields the compensated form of the spectral radiance model.

$$L_C(\lambda) = \sum_{n=1}^{N} C_n k_n(\lambda) + L_{C0}(\lambda) + \delta_C(\lambda), \tag{24}$$

where, with (9)

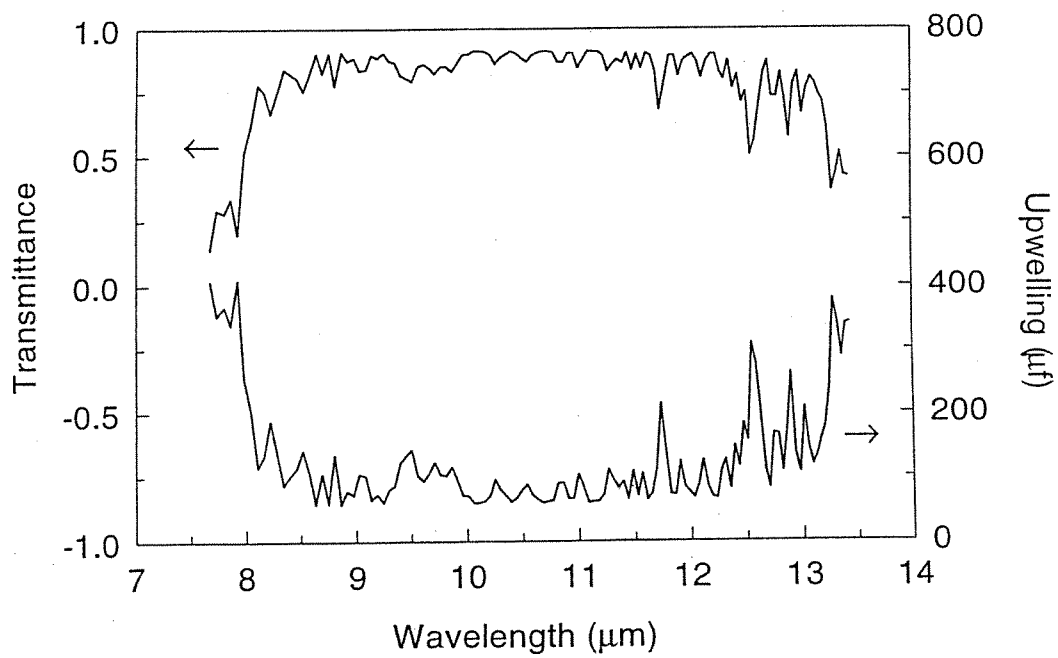

Figure 6. Atmospheric compensation spectra obtained with ISAC for Shot 96.

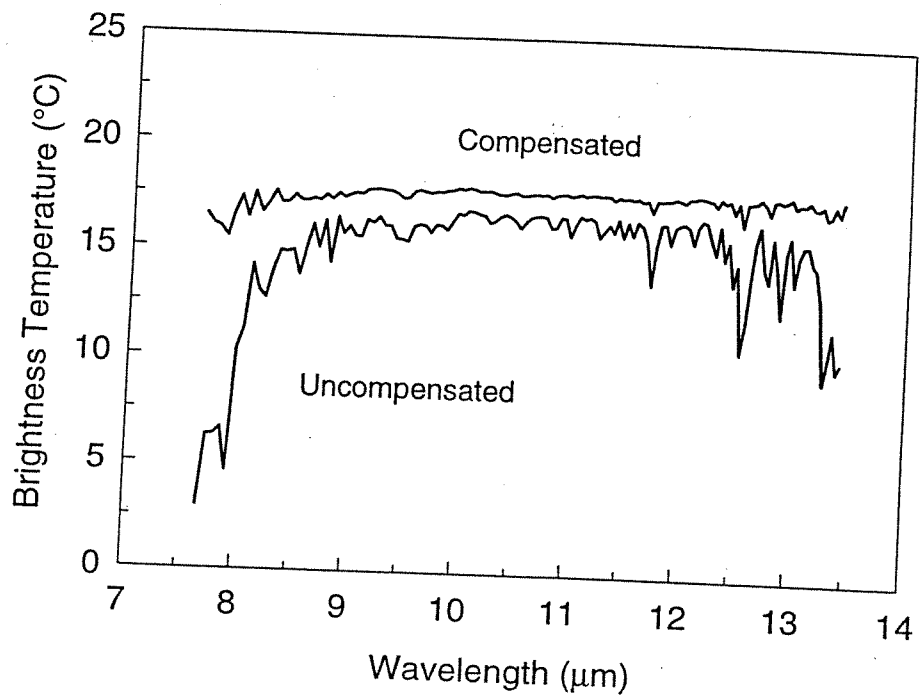

Figure 7. Example compensation of a graybody pixel spectrum from Shot 96.

$$L_{C0}(\lambda) = \left[L_0(\lambda) - L_u(\lambda)\right]/\tau(\lambda) = \varepsilon_S(\lambda)B_S(\lambda), \tag{25}$$

and $\delta_c(\lambda) = \delta(\lambda)/\tau(\lambda)$.

Two analysis options are possible. With (17) we can look for signals described by the product spectrum $\tau(\lambda)k_n(\lambda)$ in uncompensated data, and subsequently compensate the retrieved results. With (24) we can look for signals described by $k_n(\lambda)$ in compensated data. The following discussion shows that these options are not necessarily equivalent. In Section 6, analysis methods are considered in which the underlying surface radiance terms in (17) or (24) are approximated by series expansions on physical spectra (*e.g.*, spectra drawn directly from the imagery). Expansion of $L_{C0}(\lambda)$ in the compensated model (24) gives

$$L_C(\lambda) = \sum_{n=1}^{N} C_n k_n(\lambda) + \sum_{m=1}^{M} \beta_m B_{Cm}(\lambda) + \delta_C(\lambda), \tag{26}$$

where $B_{Cm}(\lambda)$ are the compensated spectra.

$$B_{Cm}(\lambda) = \left[B_m(\lambda) - L_u(\lambda)\right]/\tau(\lambda), \tag{27}$$

and β_m are expansion coefficients. A similar expansion in the uncompensated model (17) using uncompensated $B_m(\lambda)$ spectra yields

$$L(\lambda)=\sum_{n=1}^{N} C_n \tau(\lambda) k_n(\lambda)+\sum_{m=1}^{M} \beta'_m B_m(\lambda)+\delta(\lambda), \tag{28}$$

where β'_m are a different set of expansion coefficients. Compensation of (28) with (23) gives

$$L_C(\lambda)=\sum_{n=1}^{N} C_n k_n(\lambda)+\sum_{m=1}^{M} \beta'_m B_{Cm}(\lambda)+\delta_C(\lambda)-\left(1-\sum_{m=1}^{M} \beta'_m\right)\frac{L_u(\lambda)}{\tau(\lambda)}. \tag{29}$$

The upshot is that expansion in terms of uncompensated background spectra, with subsequent compensation, does not give the same functional form as expansion in terms of compensated background spectra unless the constraint is imposed that the expansion coefficients β'_m in (29) sum to unity. The inconvenience of imposing this constraint, or of calculating the final term in (29), is circumvented by always using (24) and (26) with compensated data in analyses involving expansion approximations to the underlying surface radiance spectrum. Two analysis techniques are employed in which the use of (17) or (24) are equivalent—off-plume background subtraction and spectral matched filtering. These techniques are considered in Subsection 5.2. In each case, the background term in (28) is approximated by a single spectrum with $\beta'_1 \equiv 1$. Consequently, the condition of the constraint is met.

5. Detection Analyses

This section treats two analysis methods that are of primary use in detecting plume gases in hyperspectral imagery: principal-component projection and spectral matched filtering. Use of principal components is strictly a detection method and requires no prior knowledge of what gases might be present. Spectral matched filtering is applied with a set of target gas spectra and provides a coarse quantification of any detections that might be made.

5.1 Principal Components

Principal-component image analysis will often reveal the locations of moderate to strong plumes. This detection method is useful in initial surveys of data to decide whether the collection contains plume-like features and is worthy of a more detailed analysis. It is, therefore, reasonable to apply the technique to uncompensated data. The analysis here employs principal components constructed on the *clutter spectral covariance matrix* **C** of the datacube. This matrix is defined in Appendix 1. Let $\mathbf{U}_i$ and e_i ($i = 1, 2, ..., J$) be the ordered eigenvectors and eigenvalues of the matrix. $\mathbf{U}_i$ is of length J. These vectors were computed with the singular-value decomposition (SVD) algorithm described by *Press et al.* [1990, p. 52]. Let $\mathbf{L}_p$ be a column-vector representation of $L(\lambda)$ for image pixel p. The ith principal component image is constructed by projecting each pixel spectrum onto the ith eigenvector

$$I_p(i) = \mathbf{U}_i \cdot \mathbf{L}_p \qquad p = 1,2,\ldots,P\,. \tag{30}$$

P is the number of image pixels. Example plume detections using this approach are shown in Figure 8 for the Shot 6 collection. [Principal component and contrast images are displayed with an intensity contrast stretch set to enhance visual perception. The stretch runs from $-n\sigma$ to $+n\sigma$, where n is ~4 to ~8, and σ is the root-mean-square (RMS) variation of the image values. Both principal-component and contrast images have a mean value near zero. Regions close to zero will appear medium gray. Pixels with values beyond the stretch limits will appear saturated at white or black.] **C** was constructed from the entire 128,000 pixels of the image (and includes the cloud cover in the upper fourth of the image). Three plumes are readily evident for component index $i = 11$. Two of these plumes are also fully evident for $i = 15$. A fourth plume is apparent for $i = 47$. As previously mentioned, these projections were made with uncompensated data. With compensated data, these same plumes are revealed, but at different values of the component index. One example projection from the compensated datacube is shown in Figure 8e. All four plumes are evident at $i = 8$. Detection of these plumes is effected solely by a visual search for plume-like spatial structures in the projections. In addition to plumes, many other spatial structures (*e.g.*, pipelines and buildings) are evident. A simple thresholding on some value of the projection is not sufficient to separate out plumes.

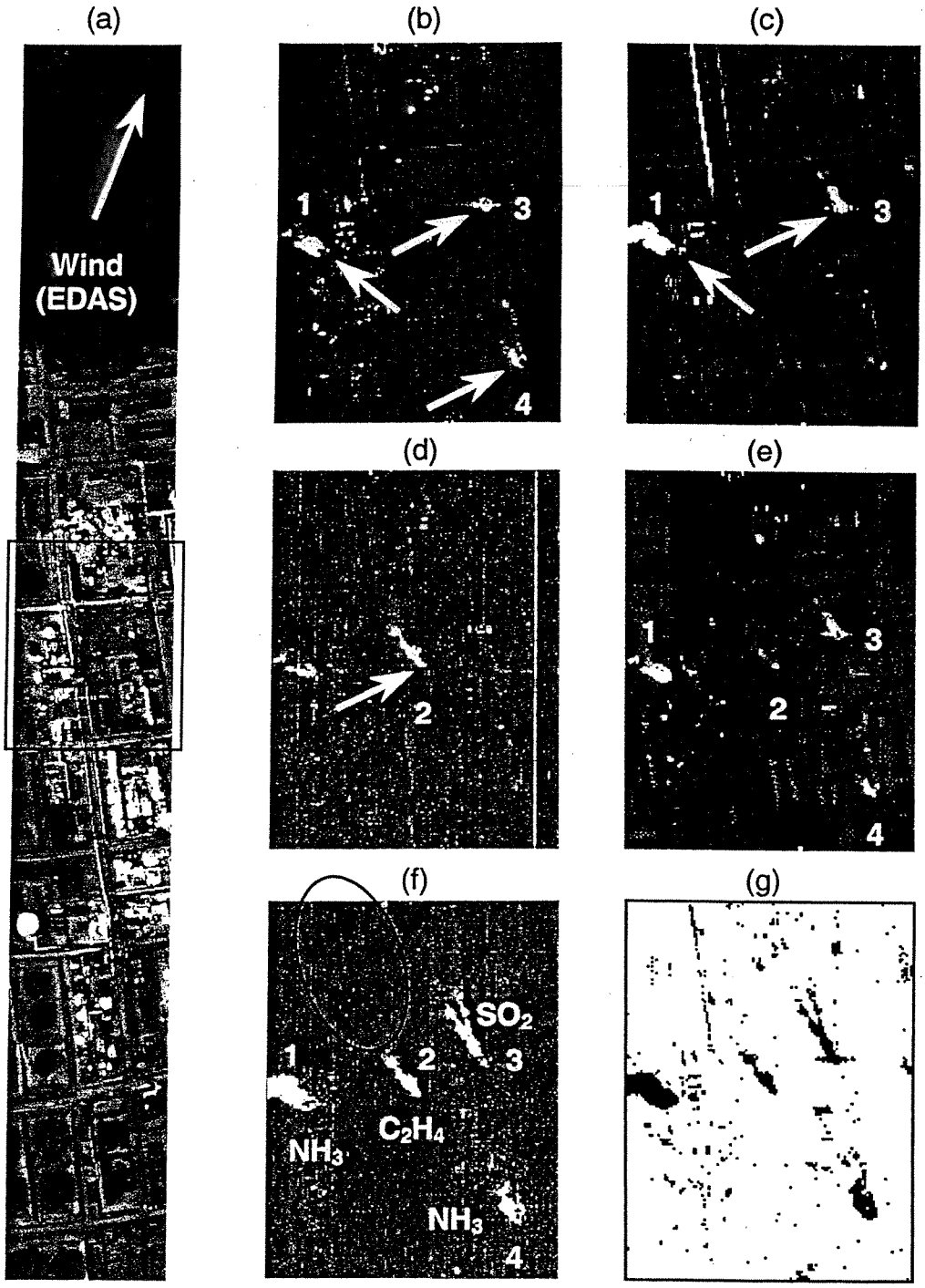

Figure 8. Plume detection in Shot 6. (a) Thermal image from a spectral bin near 12 μm showing the full 1000-frame length of the collection. All detected plume activity occurs within the overlaid rectangle. The remaining images show enlargements of this region. Numbers are plume identifiers. Principal component projections: (b) $i = 11$ (c) $i = 15$ (d) $i = 47$ (e) $i = 8$ of atmospherically compensated datacube. (f) Montage of spectral matched filter detections of ammonia, sulfur dioxide and ethylene. (g) Plume exclusion mask.

While providing the capability of locating plume structures, principal-component projections cannot be used to ascertain whether the plume appears in absorption or emission. The eigenvectors of the covariance matrix are undetermined in sign. Indeed, different methods for constructing eigenvectors will yield different signs to the same eigenvector.

Principal components can also be constructed on other matrices of the image data. The clutter *correlation* matrix, for example, provides a standardization of the data clutter by dividing each element of the covariance matrix by $\sigma_i\sigma_j = [C(i,i)C(j,j)]^{1/2}$. Use of this matrix substantially reduces the incidence of identifiable plumes in the projections. Other principal-component approaches use matrices designed to standardize the covariance matrix to sensor noise, rather than data clutter. *Roger* [1996a] provides citations to some of these *noise-adjusted* approaches. As for the correlation matrix, use of these matrices diminishes plume detection. A more promising principal-components approach would appear to be the *projection-pursuit* method reported by *Ifarraguerri and Chang* [2000]. The goal of this method is to enhance, rather than diminish, data variance. This approach was not applied in the current study.

5.2 Spectral Matched Filtering

Target detection by spectral matched filters is an application of linear least-squares regression to the solution of (17) or (24). The implementation used here is derived and discussed in Appendix 1. The application of spectral matched filtering requires a set of potential target gas spectra. If it is not known what gases are present, spectral matched filtering can be applied for the entire set of spectra in a spectral library. Two such libraries are readily available: the commercial library of *Hanst and Hanst* [1993] and the Environmental Protection Agency (EPA) library [*EPA*; *Lay and Plummer,* 1992; *Plummer and Lay*, 1992]. Occasionally, a gas can be identified in an eigenvector spectrum that produces a strong principal-component plume projection. In the current study, signal strengths of some of the gases in the plumes identified in Shot 6 are strong enough that their identities are readily evident in the compensated datacube spectra. (All spectra in this report are shown with atmospheric compensation applied.) Spectra from Plumes 1, 2, and 3 of Shot 6 are shown in Figure 9.

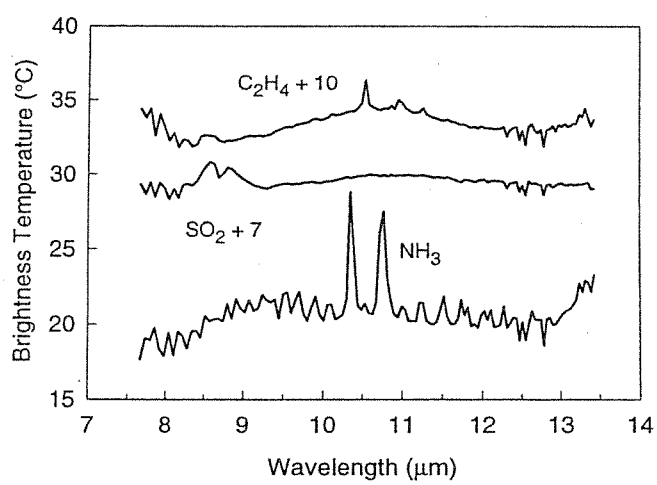

Figure 9. Plume spectra from Shot 6. The top spectrum is from Plume 2. The middle spectrum is from Plume 3. The bottom spectrum is from Plume 1. The top two spectra are offset.

Ammonia is evident in Plume 1. Sulfur dioxide is evident in Plume 3. Ethylene is just evident in Plume 2. The ethylene spectrum is enhanced in Figure 10 as a *contrast spectrum.* This spectrum was obtained by subtracting the spectrum of an off-plume pixel that matches the on-plume pixel spectrum on the *spectral guard mask* that excludes the ethylene absorption feature from 9.2 to 12.2 μm. Additionally, pixels on the *spatial plume exclusion* mask shown in Figure 8g were excluded from consideration. This mask is an overlay of principal component images for i = 11, 15, and 47, which were thresholded to exclude regions of strong plume-like projection and then converted to binary format. The mask extends over the whole 1,000 frames of the image. Only the portion containing the plumes is shown. The contrast spectrum is displayed as radiance. The upturns in the wings of the ethylene contrast spectrum below ~8.3 and above ~12.8 μm suggest the presence of carbon dioxide, water vapor, nitrogen dioxide, and nitrous oxide. Although not shown, these spectral features also appear in the contrast spectra for ammonia and sulfur dioxide. The source of the spectral features at 10.9 and 11.2 μm in the ethylene spectra is unidentified.

Spectral matched filter output images were constructed for all of the species discussed in Section 3 and listed in Table 2. The uncompensated datacube was used. Target gas spectra were multiplied with the atmospheric transmission $\tau(\lambda)$ spectrum to construct the effective target spectrum. The results for ammonia, sulfur dioxide, and ethylene in Shot 6 are shown in Figure 8f as an overlaid montage. The ethylene in Plume 2 appears in emission near the stack and in absorption (inside oval) far down the plume. Two segments of null contrast are evident. All of these detections are strong. Maximum *signal-to-noise ratio* (SNR) magnitudes range from ~20 to ~80.

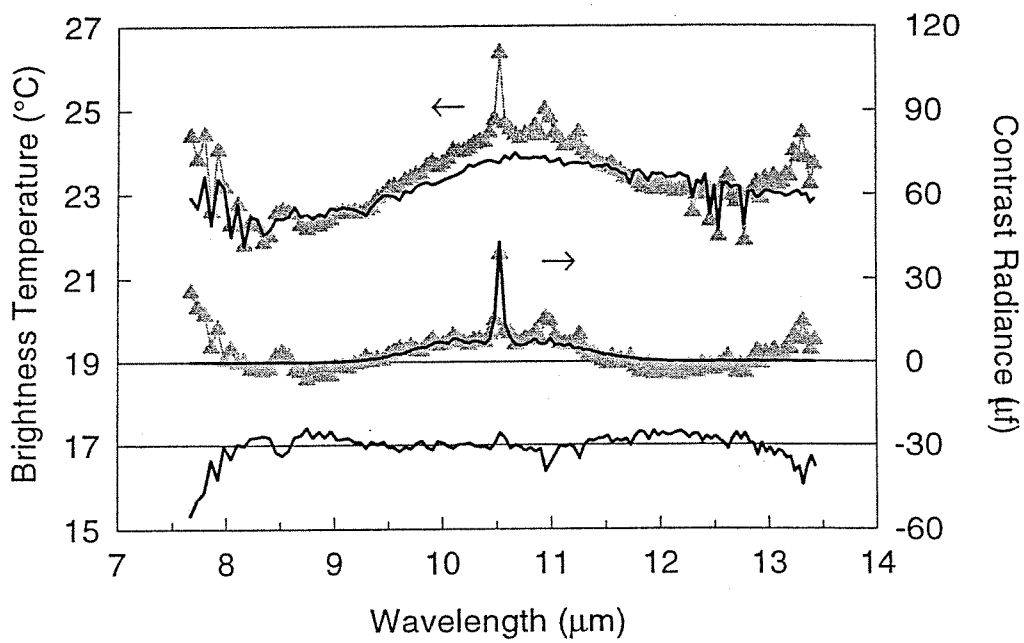

Figure 10. Ethylene spectra in Shot 6. The upper spectrum with gray symbols is from a pixel in Plume 2. The solid line is an off-plume background spectrum. The lower spectrum with gray symbols is the difference (contrast) between the top two spectra. The solid curve through the contrast spectrum is the ethylene absorption spectrum multiplied by 3.9×10^4 ppmm-μf. The lowest curve is the difference (residual) between the contrast spectrum and the fit. The RMS of the residual spectrum is $\sigma = 4.8$ μf.

Matched filter results for Shots 76, 83, and 96 of 5 April are shown in Figure 11. An *iterative* application of matched filters was used for these collections. In Shot 6 of 3 April, the plumes are small, and the collection length is 1,000 frames. On 5 April, the wind direction has changed so that Plume 1 now crosses over the full width of some of the images. Because of this change in direction, and because the 5 April collection lengths are only 500 frames, the plumes occupy a sizable fraction of the image. Consequently, the covariance matrix from which the matched filters are constructed is significantly contaminated with plume signature, and the fidelity of detection is diminished. The matched filter images built on the covariance matrix for the whole scene are used to construct *plume exclusion masks*. A new covariance matrix is constructed excluding pixels where the absolute value of the matched filter SNR for selected gases exceeds a threshold value θ. New filters and matched filter images are constructed, and the process repeated. This procedure, if allowed to continue, will eventually exclude all pixels. Termination is forced by increasing the exclusion threshold at each iteration to

$$\theta_n^{(i)} = \frac{MDC_n}{MDC_n^{(i)}}\theta_n, \tag{31}$$

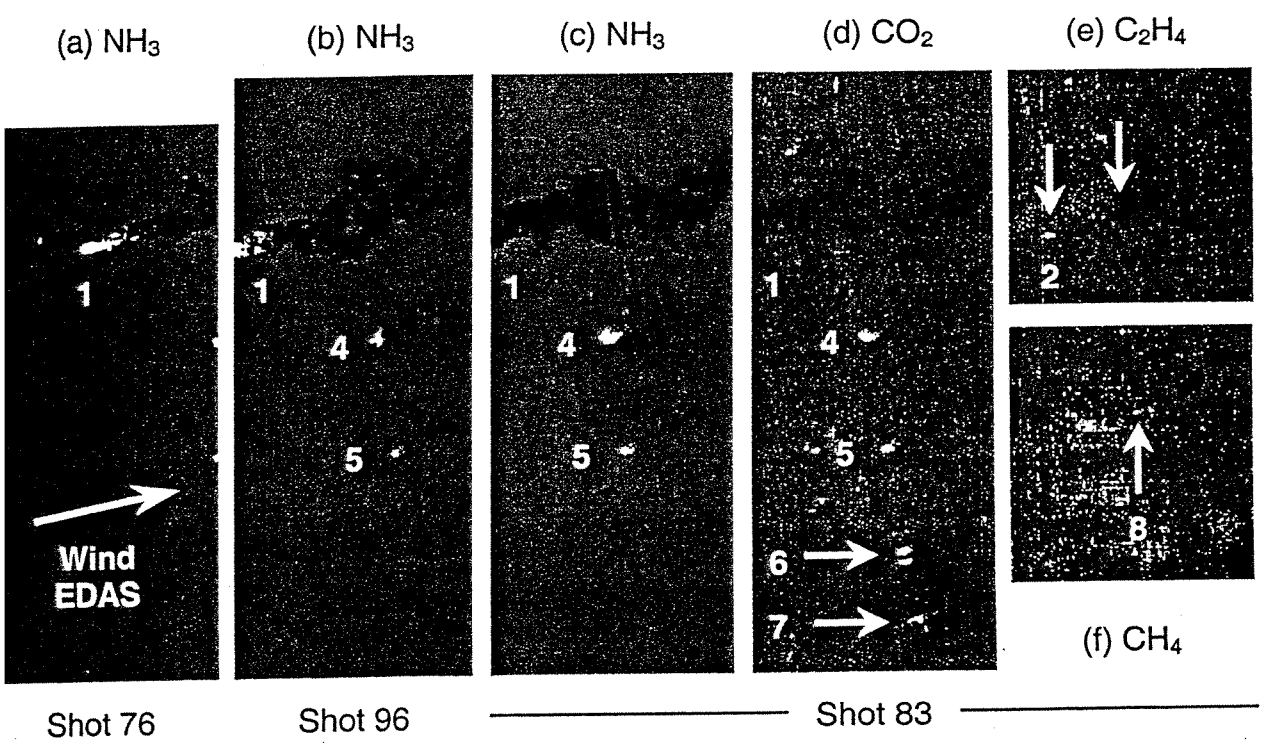

Figure 11. Spectral matched filter detection images for shots 76, 83, and 96. The images have been stretched slightly in the scan direction and registered so that spatial features line up horizontally across the figure. The collection flight line progresses to the right in the Shot order 76, 96, 83. Numbers are plume identifiers. (a) Ammonia detection in Shot 76, (b) Ammonia detection in Shot 96, (c) Ammonia detection in Shot 83, (d) Carbon dioxide detection in Shot 83, (e) Ethylene detection in Shot 83, (f) Methane detection in Shot 83.

where n is the gas species index, i is the iteration index, MDC_n is the *minimum detectable quantity* (see Appendix 1) for the nth gas that obtains with the whole scene, and $MDC_n^{(i)}$ is the minimum detectable quantity that obtains at the ith iteration. An initial threshold value of $\theta_n = 2$ for each selected gas usually yields a good exclusion mask. Termination usually occurs in ~8 to ~12 iterations. Early termination at three iterations generally produces a mask that excludes 95% or more of the pixels that would be excluded if the process were allowed to terminate on its own.

Exclusion masks were constructed in this manner for Shots 76, 83, and 96. Methane, carbon dioxide, ammonia, and ethylene were the selected gases. An initial threshold value of $\theta_n = 2$ was set for each gas. Iteration was allowed to terminate naturally. Covariance matrices were constructed on the exclusion masks and used to construct the filters for the generation of the output images shown in Figure 11. The exclusion mask for Shot 96 is shown in Figure 12a. The iteration for this case terminated naturally at $i = 8$ with 10,155 pixels eliminated. In addition to providing increased matched

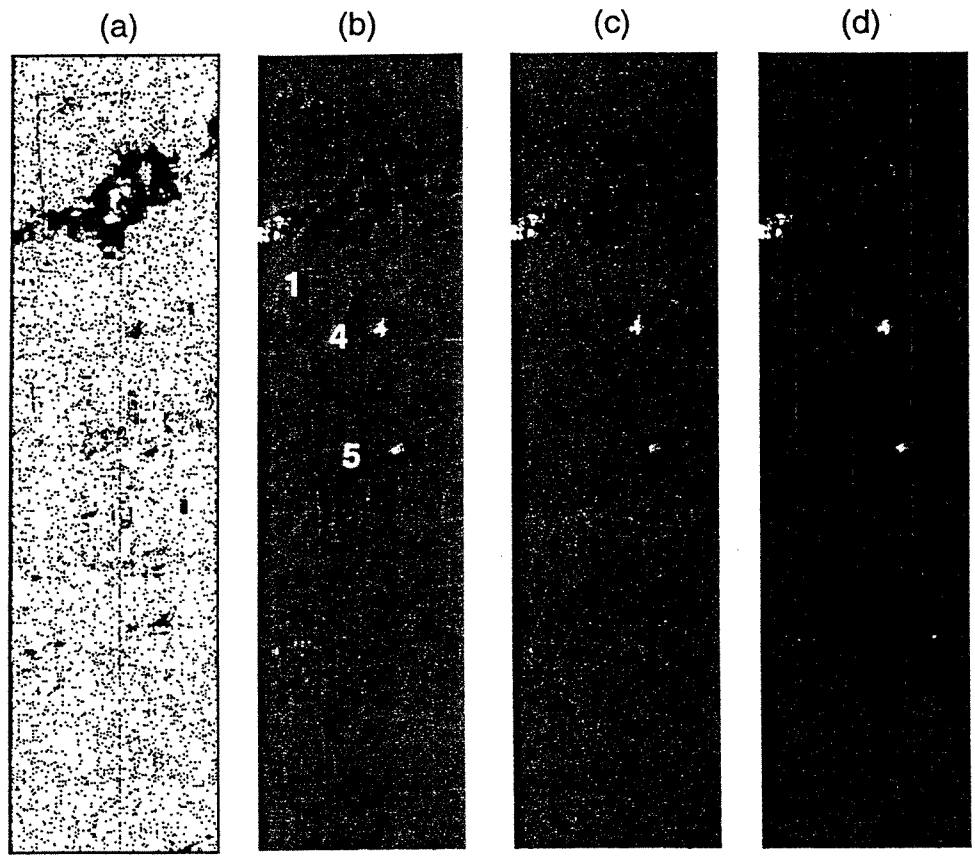

Figure 12. Unconstrained regression detection of ammonia in Shot 96. (a) Plume exclusion mask used for cluster and eigenvector analyses. (b) Contrast obtained with 15 background pixels selected manually from the image. The RMS regression residual for the scene is $\sigma = 4.0$ µf. (c) Contrast obtained with 70 cluster spectra generated with the $(OP)^2$ algorithm ($\sigma =$ 1.3 µf). (d) Contrast obtained with 114 eigenvectors of the scene clutter covariance matrix ($\sigma = 2.3$ µf).

filter detection fidelity, plume exclusion masks will be used in subsequent analyses whenever it is required to differentiate between plume and non-plume (background) pixels.

In addition to Plume 1, which was seen in Shot 6, two much smaller plumes (Plumes 4 and 5) containing ammonia are evident in Figure 11. All of these ammonia plumes are seen in emission near the stack and in absorption far downwind. The transition is so sharp for Plumes 1 and 4 that the region of null contrast is almost absent. The region of null contrast is substantial in Plume 5. Carbon dioxide is seen at the same three locations as ammonia (Plumes 1, 4, and 5), and at (at least) two other location (Plumes 6 and 7). Ethylene is seen at the same location at which it was seen in Shot 6 (Plume 2). It is now embedded in Plume 1. Sulfur dioxide is not seen at the location at which it was seen in Shot 6 (right arrow in Figure 11e), although the ethylene detection is enhanced as the plume passes over the hot stack located there. All of these detections are strong. Maximum SNR magnitudes range from ~10 to ~400. The prevailing value for carbon dioxide over most of Plume 1 is ~ –5.

A weak methane plume (Plume 8) is evident in Figure 11f. The arrow points to the most likely emission point. The contrast spectrum shown in Figure 13 confirms the presence of methane. This spectrum was obtained by subtracting the spectrum of a close-fitting, off-plume pixel spectrum as described above for ethylene. The spectral guard mask excluded the region below 8.3 μm. This methane detection emphasizes the value of visual inspection for plume activity. Only about five pixels in the plume display $SNR > 3$. Throughout most of the plume, $SNR < 2$. Unsupervised thresholding, even at a value as low as $SNR = 2$, would suppress detection of this plume.

A few very small plumes, consisting of only a single hot-stack pixel and one or two downwind pixels with identifiable gas activity, are evident in the spectral matched filter imagery. They were not examined.

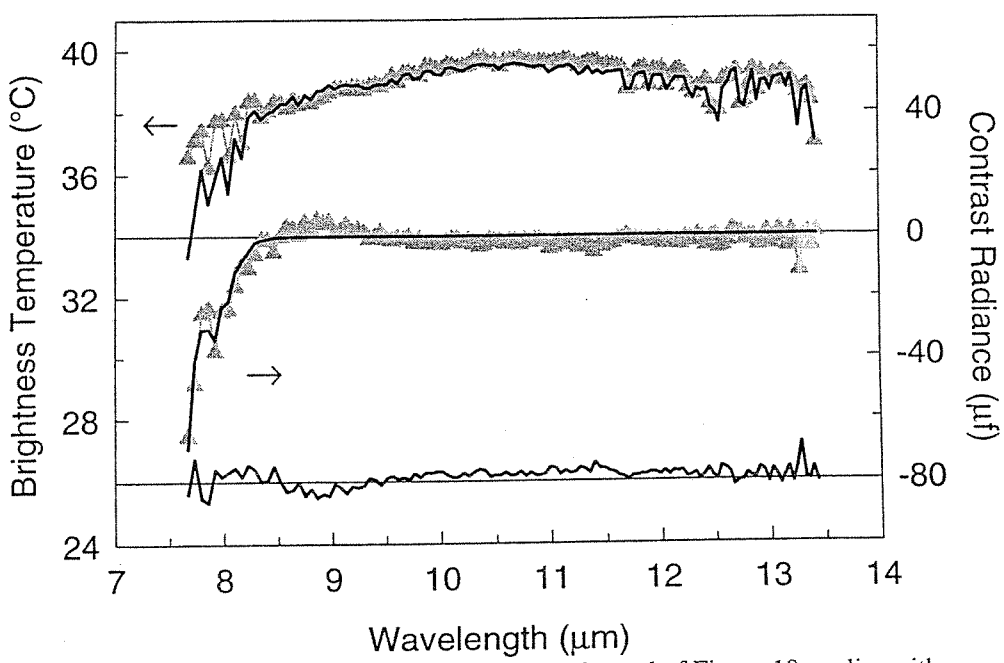

Figure 13. Methane spectra in Shot 83. The legend of Figure 10 applies with the exception that the detection is in Plume 8, the scaling constant is -6.8×10^5 ppmm-μf and the RMS of the residual is $\sigma = 2.9$ μf.

6. Regression Analyses

Analyses in this section treat gas detection and quantification by traditional linear least-squares regression methods. The compensated spectral radiance model (24) is used here. It is repeated in (32) without the encumbrance of the compensation subscript C, but with the understanding that the data have been compensated for atmospheric effects.

$$L(\lambda)=\sum_{n=1}^{N} C_n k_n(\lambda)+L_0(\lambda)+\delta(\lambda). \tag{32}$$

The two significant issues in using (32) are how to approximate the background radiance term $L_0(\lambda)$ and what regression implementation to employ. The option of measuring $L_0(\lambda)$ when the plume is not present is rarely possible and is not considered here. In the current collections, for example, it was not possible to loiter in wait of a significant change in wind direction. Even if it had been possible, the underlying surface temperature would surely have changed from its value when the plume measurements were made. Additionally, a tedious and accurate registration of the two images would be required.

The background problem is treated here by expanding $L_0(\lambda)$ on a basis set of compensated spectra $B_m(\lambda)$

$$L_0(\lambda)=\sum_{m=1}^{M} \beta_m B_m(\lambda). \tag{33}$$

Then (32) becomes

$$L(\lambda)=\sum_{n=1}^{N} C_n k_n(\lambda)+\sum_{m=1}^{M} \beta_m B_m(\lambda)+\delta(\lambda). \tag{34}$$

Basis sets consisting of spectra drawn directly from the imagery, cluster spectra constructed from the imagery, and eigenvectors of the scene covariance matrix are considered. Two regression implementations are used for the determination of the C_n and β_m amplitude coefficients: unconstrained and constrained linear least-squares regression. The regression methods employed, and a general discussion of linear least-squares regression methods, is given in Appendix 1.

6.1 Manual Background Selection

Use of a basis set of pixel spectra selected manually from the datacube is considered briefly subsection. The method is not readily amenable to unsupervised automation. Justification is that, with experience, it is fast, effective, and ultimately produces detections of the highe fidelity. Generally, a basis set constructed manually will contain fewer members than sets c structed with other methods because each member can be chosen specifically to suppress an sive background feature (*e.g.*, an expanse of carbonate pavement or all buildings with a part reflective roofing material). A basis set of 15 manually selected background spectra is show Figure 14. The spectra represent graybody spectra (the very top and bottom spectra) and otl ground surface and roofing material spectra that comprise the primary backgrounds of the sc Saturated hot-surface spectra are not included. Detection of ammonia using this set in an un strained regression is shown in Figure 12b. The image is of the contrast coefficient C_n for a that obtains for each pixel. Despite the small number of members in the basis set, the visual of the detection is high. A measure of the quality of the regression over the whole image is

$$\sigma^2 = \frac{1}{P}\sum_{p=1}^{P}\sigma_p^2 ,$$

where σ_p is the magnitude of the residual spectrum for the pth pixel, and P is the number of i pixels. In Figure 12b, this RMS residual is $\sigma = 4.0$ µf. Smaller residuals, down to the level c sensor NESR (Table 1), are obtained with larger basis sets.

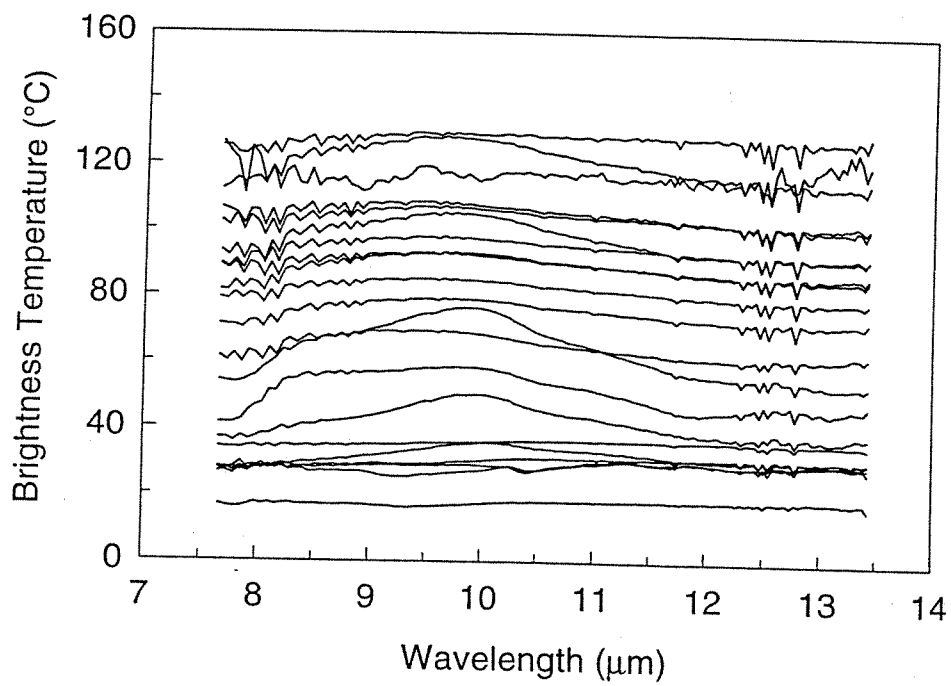

Figure 14. Basis set of 15 manually-selected backgrounds from Shot 96.

6.2 Background Endmember Extraction

Classification of surface material spectra in hyperspectral imagery is a subject of active research. The object of these studies is to formulate unsupervised algorithms that search for a small set of *endmember* spectra in a scene that allows a complete description of all scene spectra by linear superposition. The goal of these methods is superficially similar to that required here in the gas detection problem. The difference is that here we are not trying to construct an accurate *classification* of the surfaces; we are trying to suppress them. We care little whether or not we have modeled them accurately, or in as fundamental a manner as possible, so long as their influence is removed. Introductions to the literature of endmember extraction in hyperspectral data are provided by the citations in *Tompkins et al.* [1997] and *Theiler et al.* [2000]. Note, however, that this literature deals predominantly with endmember extraction from data collected in the *reflective* spectral regime ($\lambda < 3$ μm) where the signal source is reflected sunlight. The extracted endmembers are reflectance spectra. In the *thermal* regime ($\lambda > 4$ μm) where the signal is direct thermal emission from the surface, the additional dimension of temperature variation over the scene becomes an important consideration. A single endmember that represents an expanse of carbonate pavement, for example, might not be sufficient. Spectra of the surface at the highest, lowest, and possibly some intermediate, temperatures in the scene are needed to allow an accurate representation of a spectrum at an arbitrary temperature. It is not clear that existing endmember extraction algorithms are designed to handle thermal variation. No analyses using extracted endmembers are carried out here. Further discussion on endmember extraction is provided in Section 7.

6.3 Background Cluster Construction

Clustering provides an alternative to the use of spectra selected from the imagery, either by manual selection or by endmember extraction. In clustering, the various spectra in the imagery are grouped together according to some *similarity* criterion. The mean spectra of the clusters comprise the background basis set. Optionally, one of the spectra in a cluster can serve as a representative, or *exemplar*, of the cluster. Two clustering methods employed with hyperspectral data are the non-hierarchical K-Means [*Hartigan and Wong*, 1979] and ISODATA [*Hall and Khanna*, 1977] algorithms. The grouping criterion is the distance between spectra (*e.g.*, Euclidian distance or the covariance-adjusted Mahalanobis distance). One goal of these algorithms is to construct a set of M clusters that minimizes the *total within-cluster sum-of-squares*, Σ^2. Example analysis using K-Means clusters will be made. Most of the clustering work presented here, however, is done with the algorithm outlined in Figure 15. This algorithm is fast and produces clusters with characteristics much like background spectra drawn manually from the scene. In particular, it is sensitive to temperature variability and will construct clusters of similar spectral structure but different magnitude. The number of clusters generated is controlled by a single parameter, the dispersion threshold θ. This threshold sets the maximum dispersion allowed in any spectral channel for the spectra comprising a cluster. The standard deviation is used as the dispersion measure. The algorithm sometimes operates a bit faster if the loop over clusters is done backwards. This option takes advantage of the fact that a pixel spectrum is likely to belong to the same cluster as the most recently processed pixel spectrum. No attempt is made to minimize Σ^2. Adherence to this minimization criterion might be useful if the goal were an accurate classification of the surfaces, but as mentioned in the previous subsection, that is not the goal here. Because the algorithm employs only one parameter and requires only one pass through the data, it is referred to here as the $(OP)^2$ algorithm.

Make an initial cluster consisting of the single pixel whose spectrum is closest to the mean scene spectrum

Loop over all other pixels in the scene

Loop over existing clusters

If pixel will fit into cluster without increasing the maximum dispersion in any spectral channel beyond the maximum cluster dispersion threshold value θ, then

Add pixel to cluster, recompute cluster mean and dispersion, exit cluster loop

Continue loop over clusters

If pixel was not added to an existing cluster, create a new cluster and add pixel to it

Continue loop over pixels

Figure 15. $(OP)^2$ Clustering Algorithm.

Characteristics of the clustering algorithm applied to Shot 96 are shown in Figures 16 and 17. Clusters were constructed with the plume exclusion mask of Figure 12a so that no pixels representing

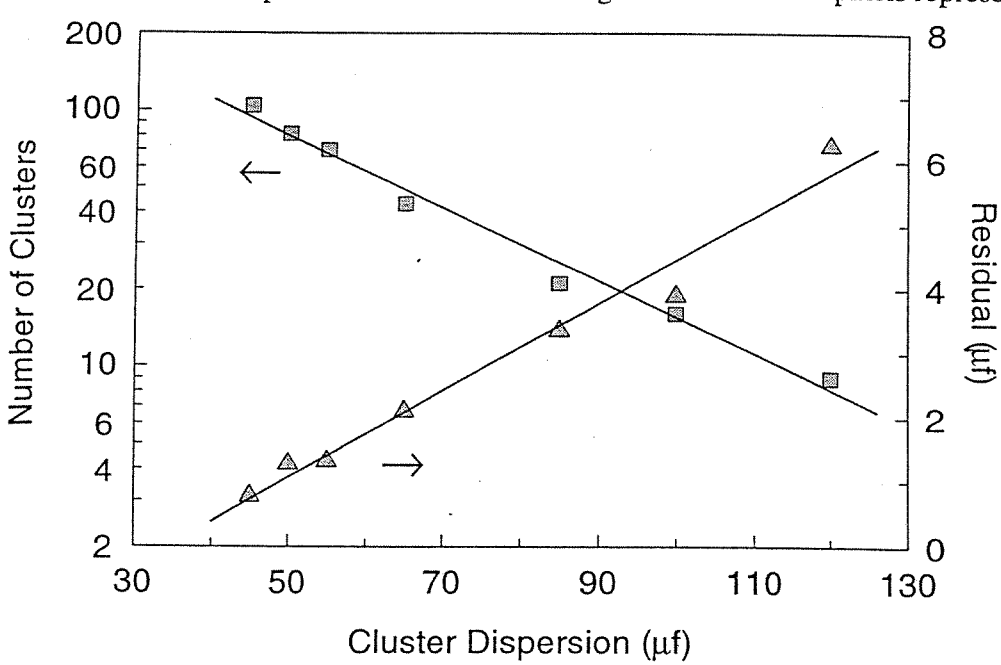

Figure 16. Variation of number of clusters and regression residual with cluster dispersion parameter θ for Shot 96.

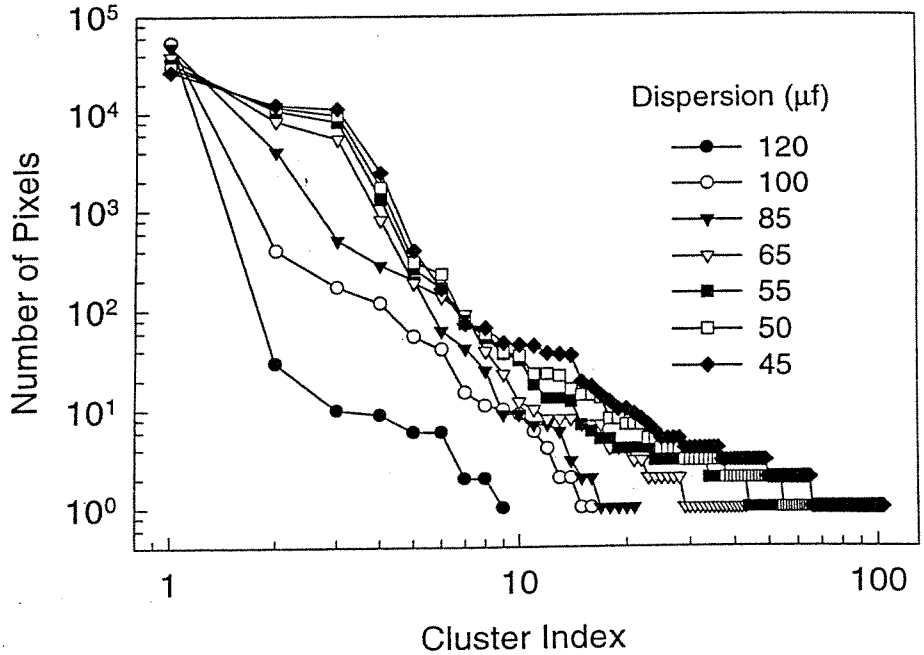

Figure 17. Variation of cluster population distribution with cluster dispersion parameter θ for Shot 96.

plume-like spectra were included. Figure 16 shows the variation in number of clusters generated as a function of the dispersion threshold θ. For regression purposes, it is necessary to limit the number of clusters to $M < J - N$. (Other uses of clusters allow larger numbers. Examples are data compression, dimensionality reduction, and *closest-cluster* background subtraction.) Figure 17 shows the sorted cluster distributions (number of pixels per cluster) for each value of θ. Many clusters for small θ consist of a single pixel spectrum. These clusters are retained. Figure 18 shows the 21 mean cluster

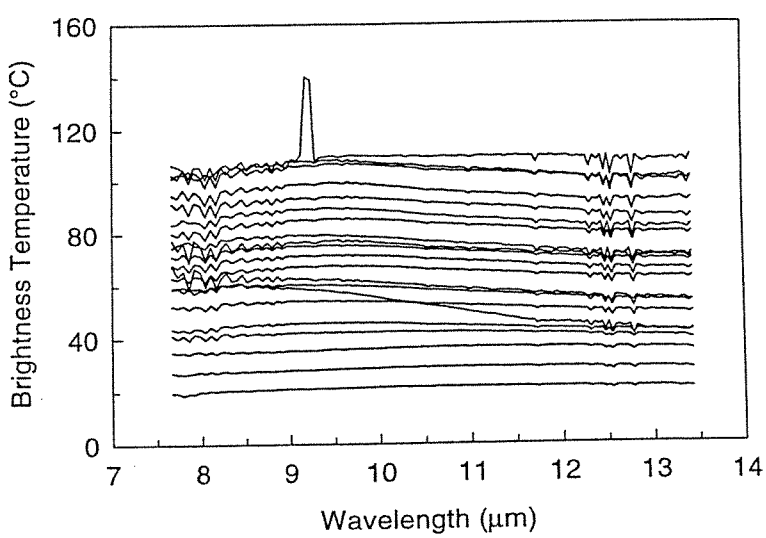

Figure 18. $(OP)^2$ mean cluster spectra for $\theta = 85$ μf in Shot 96.

spectra that were generated for $\theta = 85$ μf. One of the spectra contains an instrument artifact near 9.2 μm that occurs in some pixels from spatial column 13 of the datacube. Unconstrained regressions with ammonia as the only target gas were made using each of these seven cluster sets as the background basis set. The visual fidelity of the detection images is about the same for each set. The image for $\theta = 55$ μf (70 clusters) is shown in Figure 12c. The RMS magnitudes of the residuals for the whole image are shown in Figure 16. At $\theta = 45$ μf (104 clusters), the RMS scene residual approaches the noise level of the data (Table 1).

A comparison was made of regression results obtained with $(OP)^2$ cluster sets and K-Means cluster sets. The $(OP)^2$ clusters were used as the initial cluster centers for the K-Means iteration algorithm. Clustering was carried out with the routine KMEAN of the IMSL commercial mathematical-routines library. This routine implements the K-Means algorithm of *Hartigan and Wong* [1979]. K-Means clusters that result from the $\theta = 85$ μf $(OP)^2$ set (21 clusters) are shown in Figure 19. A reorganization of the cluster spectra of Figure 18 results from the minimization of Σ^2. For the $(OP)^2$ cluster sets, Σ^2 is of order 10^{10} μf^2. K-Means reduced this by a factor of ~20. Despite the aesthetic improvement offered by K-Means, unconstrained regressions employing the K-Means clusters as background basis sets and ammonia as the only target gas yield results that are virtually the same, both in visual fidelity of the detection images and in the total scene regression residual, as those obtained with the $(OP)^2$ clusters. This result supports the contention that the minimization of the total within-cluster sum-of-squares is not important in constructing background basis sets for gas detection. Additionally, K-Means adds substantially to computation time.

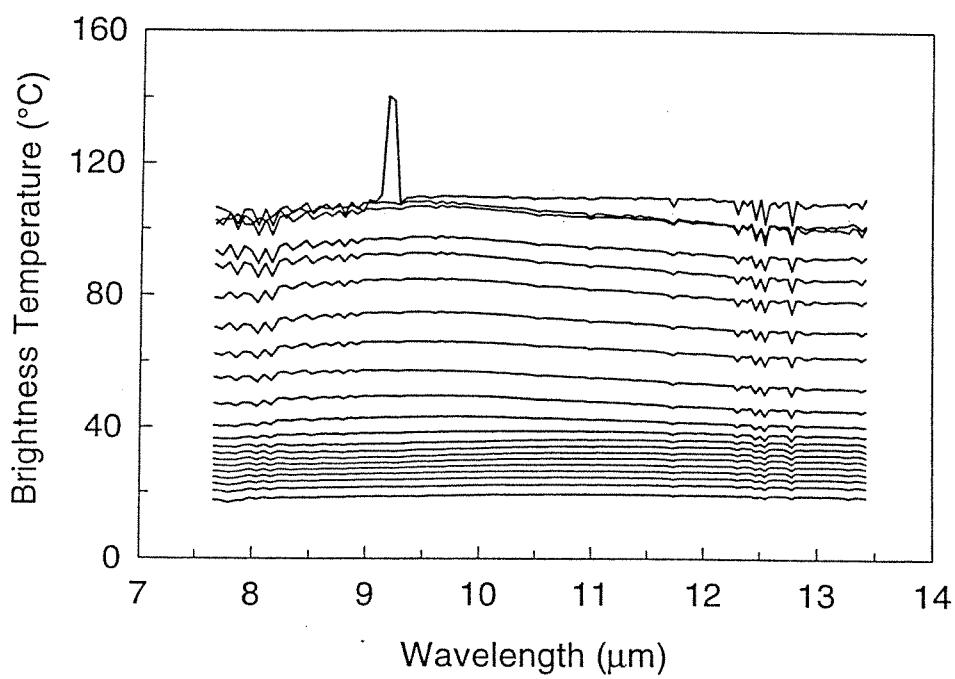

Figure 19. K-Means clusters obtained with the $(OP)^2$ clusters for $\theta = 85$ μf as the initiating clusters.

6.4 Eigenvectors as Background Basis Functions

Eigenvectors of the scene covariance matrix comprise a complete basis set of functions that spans the dimensionality of the hyperspectral datacube. Eigenvectors that generate large plume-like projections (Subsection 5.1) need to be excluded from the basis set. In application here, eigenvectors were extracted from a covariance matrix constructed on the plume exclusion mask of Figure 12a. This pixel-exclusion process goes a long way in providing eigenvectors that are free of the influence of plume-like spectra, but not far enough. Despite the exclusion of these pixels, principal-component projections still occur with significant plume-like spatial features. Without pixel exclusion, the first strong plume-like projection occurs at $i = 12$. With pixel exclusion, the first plume projection is delayed to $i = 21$, but still occurs strongly. One further step is taken to eliminate offensive eigenvectors. The spectral absorption coefficient, $k(\lambda)$, for each of the target gases in the regression is expanded in terms of the eigenvectors. In vector notation,

$$\mathbf{k} = \sum_{i=1}^{J} a_i |\mathbf{k}| e_i^{1/2} \mathbf{U}_i \,. \tag{36}$$

The expansion coefficients are

$$a_i = \frac{\mathbf{k} \cdot \mathbf{U}_i}{|\mathbf{k}| e_i^{1/2}} \,. \tag{37}$$

The square root of the eigenvalue and the magnitude of the absorption coefficient vector are included in (36) to keep all a_i of the same order of magnitude. Expansion coefficients for the ammonia spectral absorption coefficient are shown in Figure 20. Eigenvectors corresponding to large coefficients

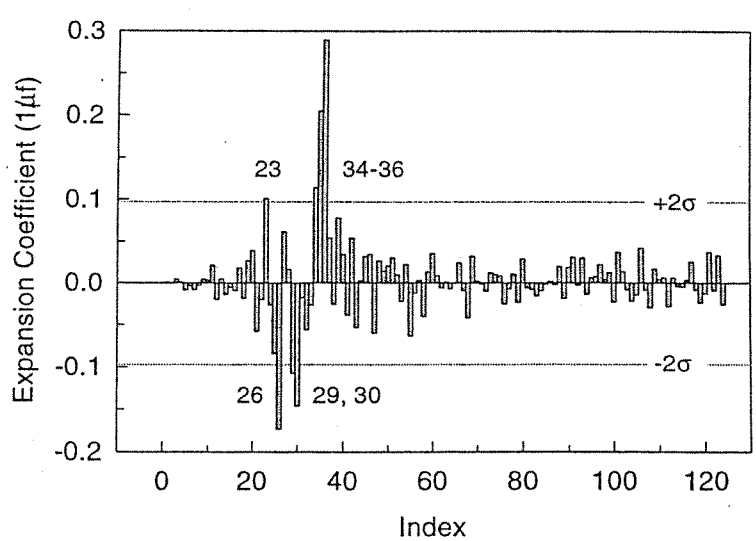

Figure 20. Eigenvector expansion coefficients for ammonia spectral absorption coefficient.

contribute significantly to the spectral structure of the gas absorption coefficient, and if allowed to participate in the expansion for the background term $L_0(\lambda)$, will spoil the target detection. The ith eigenvector is excluded from the background basis if $|a_i|$ is greater than a threshold value. The threshold value $\theta\sigma_a$ with $\theta = 2$ and

$$\sigma_a^2 = \frac{1}{J}\sum_{j=1}^{J} a_j^2 \tag{38}$$

generally provides a good exclusion. Figure 20 shows that seven eigenvectors have coefficients that exceed the threshold. The unconstrained regression that results when these seven eigenvectors are excluded from the background basis set is shown in Figure 12d. It has the same visual fidelity as the results obtained with manual-background and cluster-background selection.

This *eigenvector-deletion* procedure is a good candidate for unsupervised batch application. Along with a set of candidate target gases, only a few parameters need to be specified: a threshold value θ_n for each gas used in constructing the plume exclusion mask (31) and a threshold setting θ for deleting eigenvectors. A default value of 2 for each of these thresholds generally produces good results. As pointed out later, however, unconstrained regression with eigenvectors as background basis spectra is suitable only for detection.

6.5 Spectral Extractions

Results so far have dealt with visual images of plume detection using unconstrained linear least-squares regression. In this section, pixel contrast spectra that result from regression analyses are considered. When regression on a pixel spectrum is completed, the modeled background spectrum $L_0(\lambda)$ can be calculated from (33):

$$L_0(\lambda) = \sum_{m=1}^{M} \beta_m B_m(\lambda). \tag{39}$$

The contrast spectrum is

$$C(\lambda) = L(\lambda) - L_0(\lambda). \tag{40}$$

The modeled regression fit to the contrast spectrum is

$$C_R(\lambda) = \sum_{n=1}^{N} C_n k_n(\lambda). \tag{41}$$

The residual spectrum is

$$\delta(\lambda) = L(\lambda) - [C_R(\lambda) + L_0(\lambda)]. \tag{42}$$

Application to a single pixel from Plume 4 in Shot 96 is considered here. The pixel is about 2 m downwind of the hot stack. Results for an amalgamation of plume pixels are presented in Subsection 6.7.

A preliminary off-plume-background analysis was made. The background pixel was selected by searching the entire image outside the plume exclusion mask of Figure 12a and on a spectral guard mask that deleted the spectral regions below 8.2, above 12.8, and between 10.2 and 11.0 μm. The plume, background, and contrast spectra are shown in Figure 21. The contrast spectrum indicates the presence of ammonia, carbon dioxide, water vapor, and nitrogen dioxide. Additionally, nitrous oxide was included as a tentative species. (A discussion on the selection of candidate gases for regression modeling is made in the next subsection.) The contrast coefficients C_n obtained with a least-

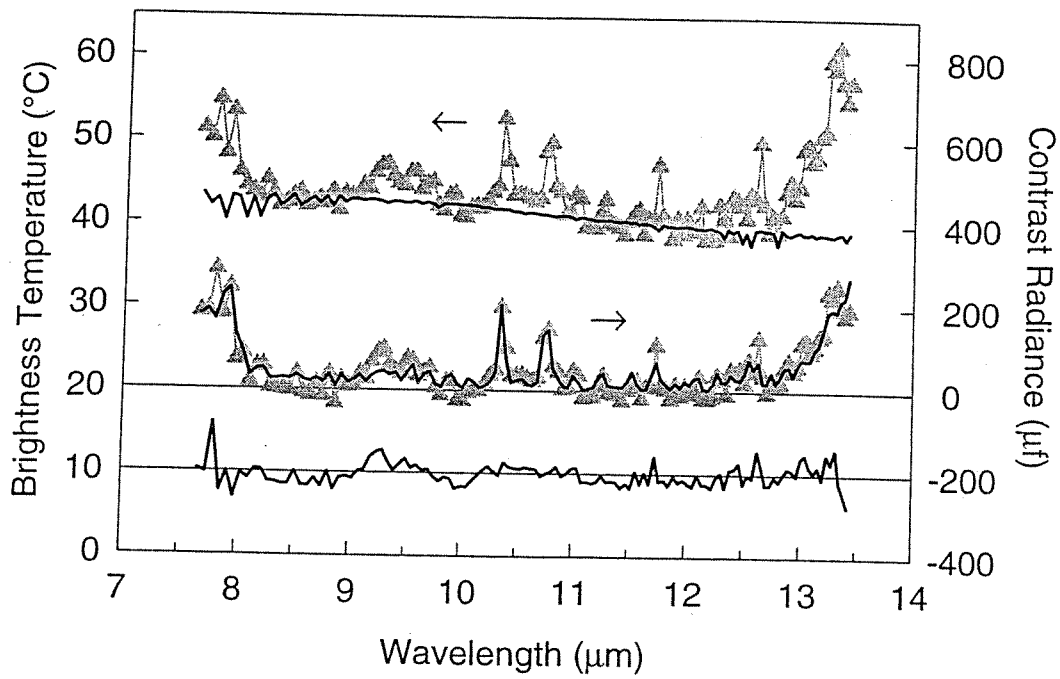

Figure 21. Off-plume background subtraction on a single pixel in Plume 4 of Shot 96. The upper spectrum with gray symbols is the pixel spectrum. The solid line is an off-plume background spectrum. The lower spectrum with gray symbols is the difference (contrast) between the two upper spectra. The solid line through the contrast spectrum is a regression fit to the contrast spectrum. The lowest curve is the residual spectrum of the fit. It is offset for clarity. The RMS of the residual spectrum is $\sigma = 26.3$ μf.

squares fit to the functional form (41) are tabulated in the upper section of Table 4. The significance of the results is indicated by the detection SNR and the *T*-Test probability that the detection is not accidental (Appendix 2). All five gases are detected in emission with significant detection probability. The residual of the fit is $\sigma = 26.3$ μf.

Unconstrained regression was carried out on this same pixel. The target set consisted of the same five gases identified above. The background basis set was the $\theta = 45$ μf cluster set (104 clusters) constructed in Subsection 6.3. Two clusters displaying the instrument artifact mentioned in Subsection 6.3 were deleted from the set. The regression results are shown in Figure 22 and the middle section of Table 4. These results are fundamentally inconsistent with the result obtained in the off-plume pixel-subtraction analysis—the contrast coefficients for water vapor and nitrous oxide are negative and the detection probability for nitrous oxide is insignificant. The significance of all species except ammonia is less than compelling. The reason for this vast discrepancy is evident in the background spectrum generated by the unconstrained regression (Figure 22)—it is unrealistic. There are no off-plume spectra anywhere in the imagery that resemble this fabricated spectrum. The problem is caused by the extreme flexibility allowed in the unconstrained use of background spectra in linear combination. Examination of the expansion coefficients β_m reveals that many of them are negative. This contradicts the realistic expectation that the basis spectra should be represented with positive coefficients. This contradiction and the inconsistent sign of the water vapor and nitrous oxide coefficients are corrected by implementing a constrained regression in which all of the target coefficients are required to have the same sign, and the background coefficients are required to be nonnegative. The method for implementing this constrained regression is discussed in Appendix 1.

Table 4. Single-Pixel Contrast Coefficients for Plume 4 in Shot 96

Gas	*C* (ppmm-μf)	*SNR*	P_T
Closest ($\sigma = 26.34$ μf)			
N_2O	$2.29 \pm 0.57 \times 10^5$	4.0	1.00
H_2O	$2.14 \pm 0.35 \times 10^9$	6.1	1.00
CO_2	$2.28 \pm 0.27 \times 10^8$	8.4	1.00
NO_2	$2.37 \pm 0.68 \times 10^5$	3.5	1.00
NH_3	$1.24 \pm 0.10 \times 10^5$	11.9	1.00
Unconstrained ($\sigma = 4.41$ μf)			
N_2O	$-0.09 \pm 2.10 \times 10^5$	-0.05	0.01
H_2O	$-1.36 \pm 0.66 \times 10^9$	-2.1	0.55
CO_2	$1.60 \pm 0.43 \times 10^8$	3.8	0.82
NO_2	$3.57 \pm 0.84 \times 10^5$	4.2	0.86
NH_3	$9.73 \pm 0.59 \times 10^4$	16.6	1.00
Constrained ($\sigma = 22.54$ μf)			
N_2O	$1.33 \pm 0.53 \times 10^5$	2.5	0.97
H_2O	$2.71 \pm 0.38 \times 10^9$	7.1	1.00
CO_2	$1.93 \pm 0.24 \times 10^8$	8.2	1.00
NO_2	$2.19 \pm 0.60 \times 10^5$	3.6	1.00
NH_3	$1.36 \pm 0.10 \times 10^5$	13.1	1.00

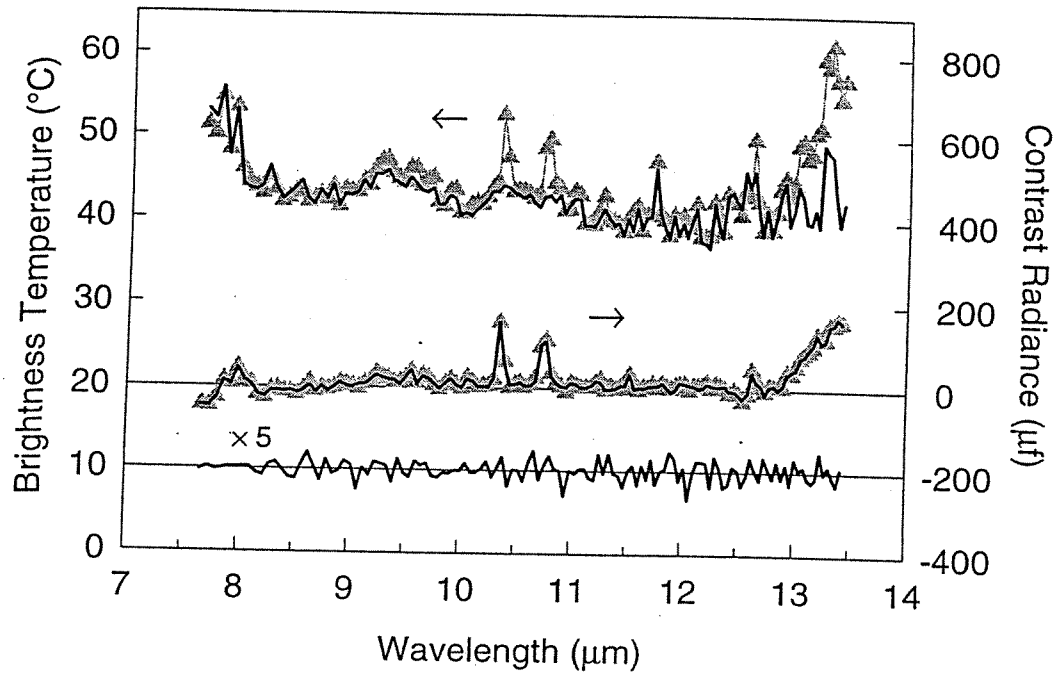

Figure 22. Unconstrained regression on a single pixel in Plume 4 of Shot 96. The upper spectrum with gray symbols is the pixel spectrum. The solid line is the regression background spectrum (Equation 39). The lower spectrum with gray symbols is the contrast spectrum (Equation 40). The solid line through the contrast spectrum is the fit to the contrast spectrum (Equation 41). The lowest curve is the residual spectrum of the fit (Equation 42). It is offset for clarity. The RMS of the residual spectrum is $\sigma = 4.4$ μf. The residual spectrum is magnified by a factor of 5.

The constrained regression results are shown in Figure 23 and the lower section of Table 4. The tabulated results are consistent with those of the off-plume pixel-subtraction analysis. The contrast coefficients are statistically unchanged (Appendix 2), and the RMS residual of the fit ($\sigma = 22.5$ μf) is only slightly smaller. Both residuals are, however, much larger than the value obtained with the unconstrained regression. Only $M = 3$ of the 102 cluster spectra survived the regression with positive coefficients.

A study was made of the shortcomings of unconstrained regression. The main findings are: 1) If a gas in the target suite is not present in the plume, it will nevertheless often be found with a non-insignificant probability; 2) If a gas is not in the target suite, but is present in the plume, its absence from the suite will not be evident in the spectral structure of the residual spectrum. An extreme example illustrates this latter point. Results for both an unconstrained and a constrained regression with *no* gases in the target suite are shown in Figures 24 and 25. The unconstrained regression has contrived to model the underlying surface spectrum as the observed spectrum. The contrast spectrum is zero. Most revealing is the absence of any spectral clue in the residual spectrum that the regression has been grossly mis-modeled. The residual spectrum for the constrained regression shown in Figure 25, on the other hand, clearly reveals the effects of the mis-modeling.

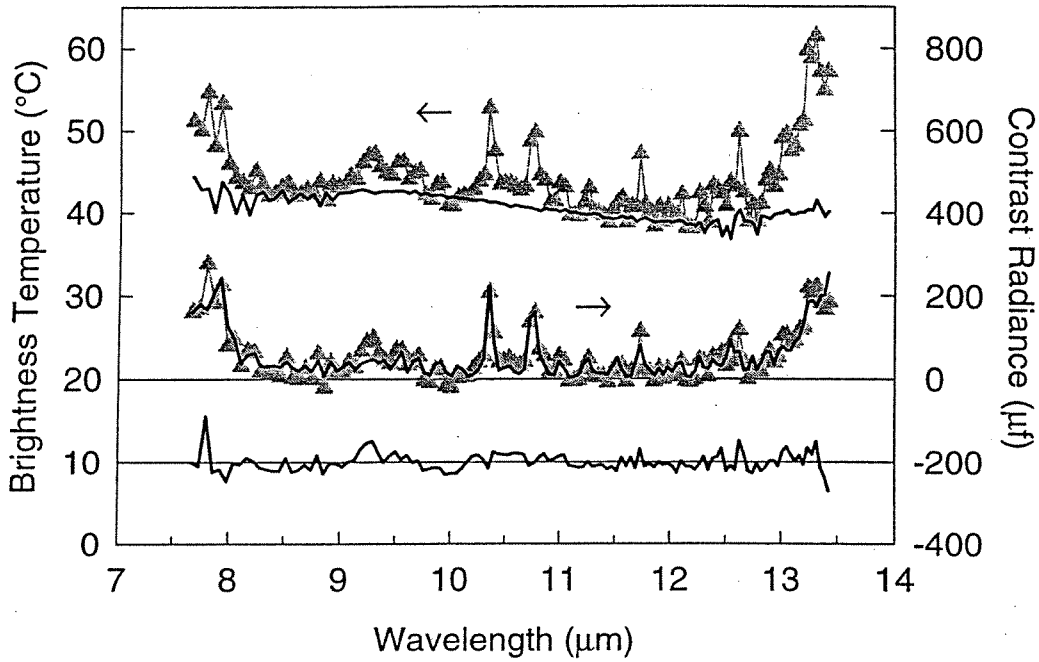

Figure 23. Constrained regression on a single pixel in Plume 4 of Shot 96. The legend of Figure 22 applies with the exception that the RMS of the residual spectrum is $\sigma = 22.5$ μf, and the residual spectrum is not magnified.

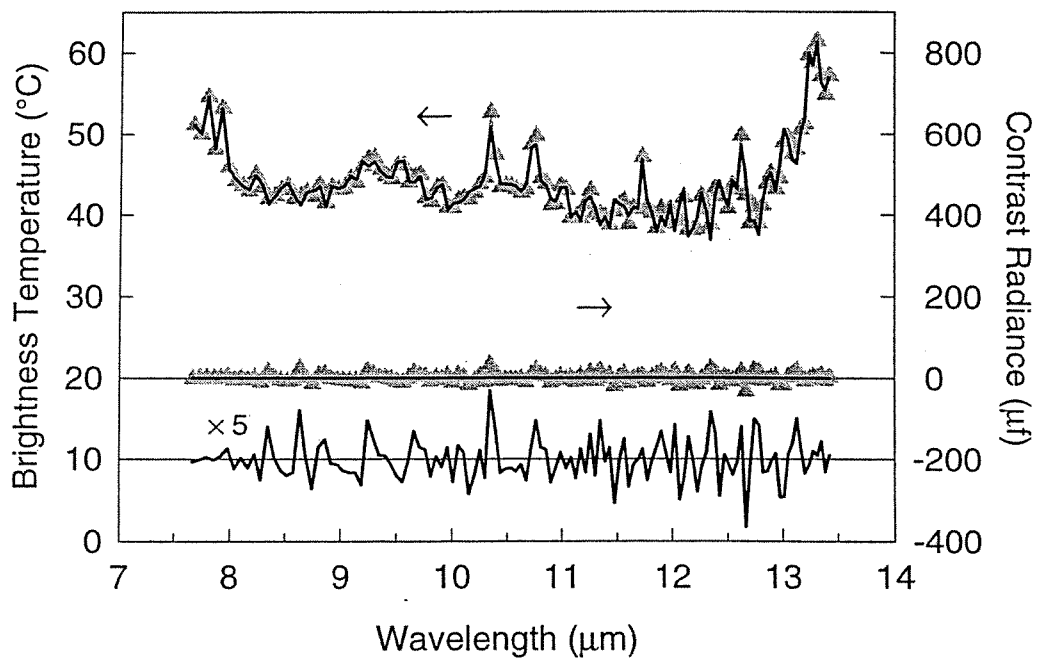

Figure 24. Unconstrained regression on a single pixel in Plume 4 of Shot 96 with no target gases included in the regression. The legend of Figure 22 applies with the exception that the RMS of the residual spectrum is $\sigma = 10.3$ μf.

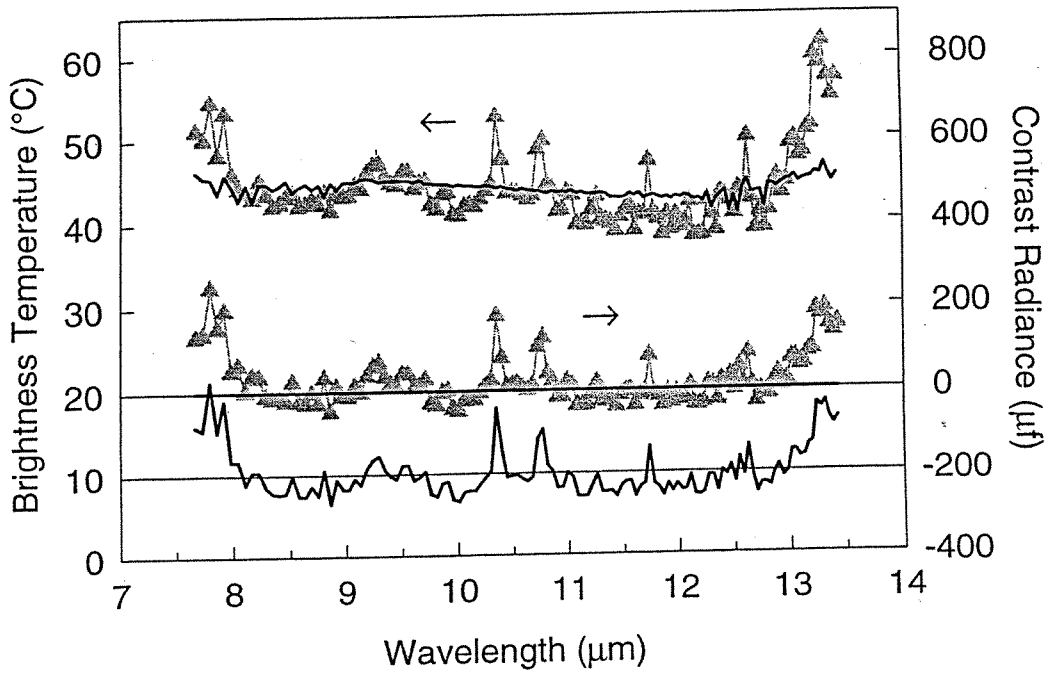

Figure 25. Constrained regression on a single pixel in Plume 4 of Shot 96 with no target gases included in the regression.' The legend of Figure 22 applies with the exception that the RMS of the residual spectrum is $\sigma = 59.4$ μf and the residual spectrum is not magnified.

The need for non-negative regression constraint has long been recognized in surface classification applications. It was not initially evident that this constraint would be required when the surface spectra are used to suppress backgrounds in the gas detection problem. The evidence now is that they must be constrained. With cluster spectra, direct pixel spectra, or endmember spectra used as background basis functions, constrained regression can be implemented in a natural manner by requiring that their regression coefficients be non-negative. With eigenvectors as the basis functions, there is no obvious way to impose physically meaningful constraints. This inability to impose constraints demotes regression on eigenvectors to the status of a detection method with questionable value in providing quantitative target information. The remaining analyses will continue to show unconstrained results along with constrained results to further demonstrate the inadequacy of unconstrained regression for quantitative gas analysis.

6.6 Significance Tests

In this subsection, statistical tests are applied to assess the quality of the regressions made in the preceding subsection. These tests rely on the assumption of random normal deviates. The validity of this assumption was tested by application of the Kolmogorov-Smirnov procedure to the residual spectra obtained in the regressions. The method of application is presented in Appendix 2. Results of the application for the unconstrained and constrained regressions are shown in Figures 26 and 27. The plots compare the cumulative probability distribution for the residual spectra with the cumulative probability distribution for the normal distribution. The test statistic D_{KS} is the maximum abso-

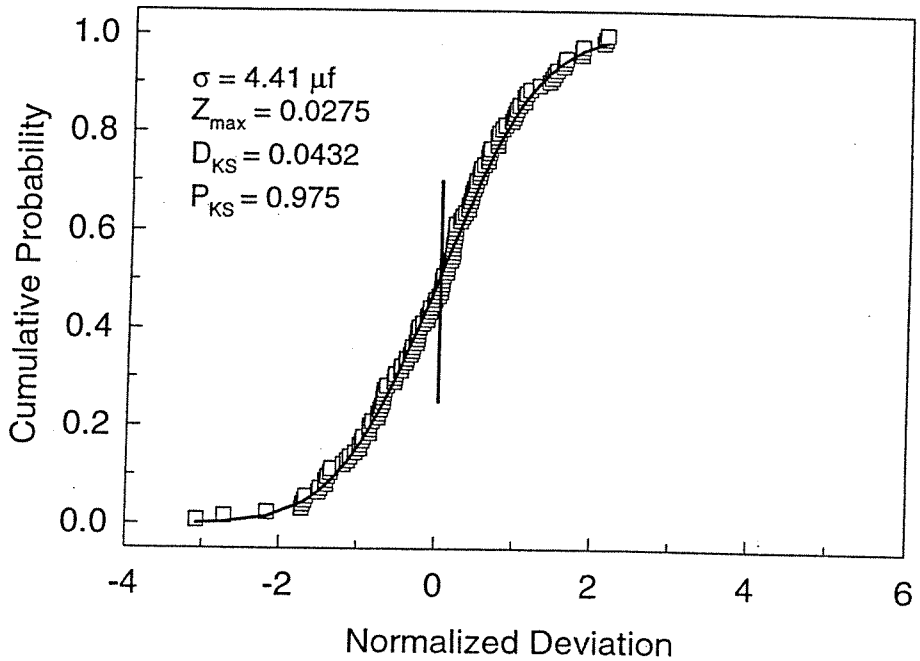

Figure 26. Cumulative probability distributions in unconstrained regression on a single pixel in Plume 4 of Shot 96. The residual distribution is shown with symbols. The normal distribution is shown as a solid line. The vertical bar marks the position of maximum difference between the distributions.

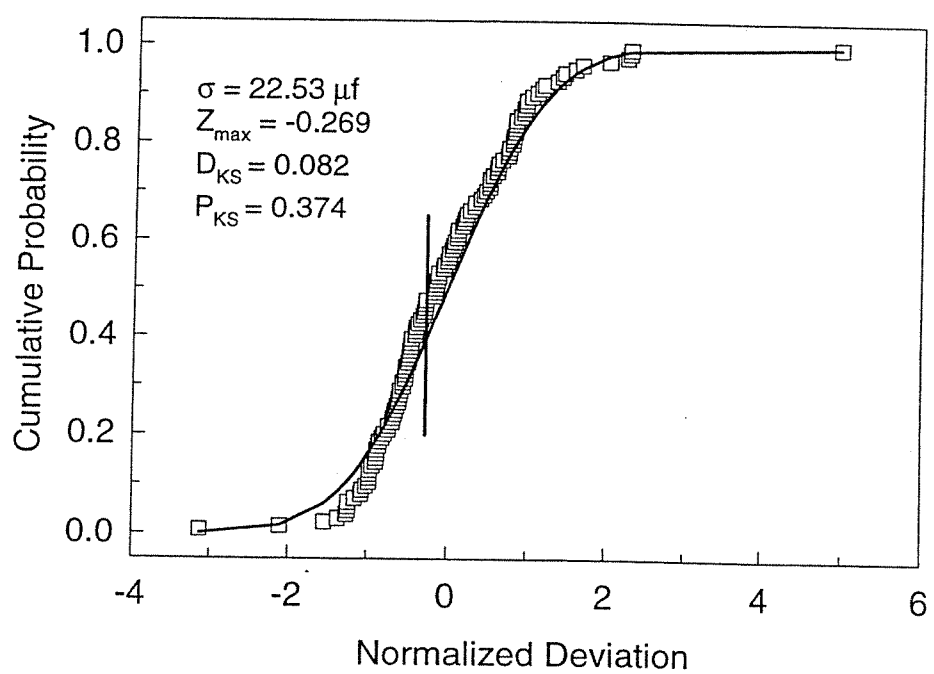

Figure 27. Cumulative probability distributions in constrained regression on a single pixel in Plume 4 of Shot 96. The legend of Figure 26 applies.

lute difference between the two cumulative distributions. The significance level $P_{KS} = 0.98$ for the unconstrained regression confirms compliance with the assumption of normal deviates. The significance level $P_{KS} = 0.37$ for the constrained regression does not confirm compliance, but is not so low as to refute compliance; i.e., a fit this bad can still occur 37% of the time even with random normal deviates. The assumption of normal deviates is accepted for both regressions.

The construction of a regression model that accurately describes the presence and absence of candidate regression terms is a subjective exercise. No single robust technique applies to all cases. The guidance of *Draper and Smith* [1966] is used here. To test the inclusion or exclusion of target gases against a fixed set of background basis functions, we start with the assumption that we know what gases are likely to be present. We then delete them one at a time in a *backward elimination* process and test the significance of the deletion. The significance can be assessed equivalently with either an *F*-Test or a *T*-Test (Appendix 2). The latter is used here. An important consideration in this procedure is account of large correlations among the target spectra. The correlation matrix for the eight gases considered here is shown in Table 5. Two groups of gases display high intercorrelation. Methane, nitrous oxide, and water vapor comprise one group. Carbon dioxide and nitrogen dioxide comprise another. The remaining gases are not strongly correlated with any of the others. The importance of correlation is that, in the end, it might not be possible to decided unambiguously which of the correlated species is actually detected. Table 6 shows the backward elimination process for the constrained regression of the preceding subsection. The first column of P_T values is obtained when all gases are included in the regression. Within the first group of correlated gases, the presence of water vapor is assured. The significance levels for methane and nitrous oxide are small, but these species are retained for further consideration. In the second correlated group, the presence of both carbon dioxide and nitrogen dioxide is assured. Within the uncorrelated group, ethylene has a low significance and is deleted, ammonia has a high significance and is retained. Sulfur dioxide did not survive the positive constraint and is eliminated. The second column of P_T values shows the results when the regression is made with the six retained gases. The third and fourth columns of P_T values show the results for deleting either nitrous oxide or methane from the six-gas set. The results display the ambiguity that can arise with correlated gases. If both gases are retained, then neither is significant. If either is removed, the other becomes significant. Here, nitrous oxide is retained in favor of methane solely on the basis of the 1-part-in-2200 smaller residual that results with its retention.

Table 5. Absorption Spectra Correlation Matrix

	CH_4	N_2O	H_2O	CO_2	NO_2	NH_3	SO_2	C_2H_4
CH_4	1.000	**0.936**	**0.766**	-0.092	-0.296	-0.132	-0.062	-0.138
N_2O	**0.936**	1.000	**0.779**	-0.086	0.314	-0.121	-0.031	-0.128
H_2O	**0.766**	**0.779**	1.000	0.101	0.459	-0.217	0.017	-0.277
CO_2	-0.092	-0.086	0.101	1.000	**0.699**	-0.120	-0.129	-0.145
NO_2	-0.296	0.314	0.459	**0.699**	1.000	-0.222	-0.172	-0.254
NH_3	-0.132	-0.121	-0.217	-0.120	-0.222	1.000	-0.098	0.205
SO_2	-0.062	-0.031	0.017	-0.129	-0.172	-0.098	1.000	-0.197
C_2H_4	-0.138	-0.128	-0.277	-0.145	-0.254	0.205	-0.197	1.000

Table 6. Test for Significant Gases in Constrained Regression for Plume 4 in Shot 96

Gas	SNR	P_T	SNR	P_T	SNR	P_T	SNR	P_T
N	7		6		5		5	
M	4		3		4		4	
σ (μf)	22.35		22.48		22.55		22.54	
CH_4	0.5	0.37	0.8	0.54	2.5	0.98	—	—
N_2O	0.8	0.56	0.8	0.58	—	—	2.5	0.98
H_2O	7.0	1.00	7.1	1.00	7.2	1.00	7.1	1.00
CO_2	8.3	1.00	8.2	1.00	8.1	1.00	8.2	1.00
NO_2	3.7	1.00	3.7	1.00	3.7	1.00	3.6	1.00
NH_3	13.1	1.00	13.1	1.00	13.0	1.00	13.1	1.00
SO_2	0.0	0.00	—	—	—	—	—	—
C_2H_4	1.2	0.73	—	—	—	—	—	—

Application of this procedure to the contrast spectrum obtained in the preceding subsection by subtracting a close, off-plume background spectrum yields the same qualitative result as the constrained regression. Application to the unconstrained regression, although only of academic interest, is shown in Table 7. Here we obtain the result in a single elimination step that only ammonia and carbon dioxide are highly significant.

Table 8 shows the results for testing the addition of background basis functions to the regression. A series of regressions was made with the $(OP)^2$ cluster sets described in Subsection 6.3. The first column of the table identifies the cluster set by its dispersion parameter θ. The target set consisted of the $N = 5$ gases used in the regressions of the previous subsection (*i.e.*, water vapor, carbon dioxide, nitrogen dioxide, ammonia, and nitrous oxide). The number of basis spectra M in the unconstrained regressions is the number of spectra in the cluster set. The number in the constrained regressions is the number that survives the positive constraint. The significance of the increased number of spectra in the unconstrained regression is assessed with the addition F-Test (Appendix 2). The application of this test assumes that the mean cluster spectra in the larger of two cluster sets comprise a superset of the smaller cluster set, *i.e.*, the larger set contains all of the cluster spectra of the smaller set. This

Table 7. Test for Significant Gases in Unconstrained Regression for Plume 4 in Shot 96

Gas	SNR	P_T
$\sigma = 0.41$ μf		
CH_4	-2.58	0.66
N_2O	1.25	0.34
H_2O	-0.94	0.25
CO_2	5.15	0.95
NO_2	1.78	0.48
NH_3	16.03	1.00
SO_2	3.44	0.81
C_2H_4	-0.81	0.21

Table 8. Test for Significant Background Basis Functions in Regressions for Plume 4 in Shot 96

θ (μf)	Unconstrained			Constrained	
	M	σ (μf)	P_F	M	σ (μf)
120	9	23.47		3	25.52
100	16	18.77	1.00	3	24.58
85	21	15.83	1.00	3	24.33
65	43	10.28	1.00	3	24.37
55	70	7.05	0.99	4	22.26
50	81	6.00	0.75	4	22.26
45	104	4.32	0.13	5	22.26

assumption holds quite well for all of the $(OP)^2$ cluster sets constructed here. The F-Test is not applicable to constrained regression. In Table 8, the RMS regression residuals are shown for both the constrained and unconstrained regressions. The P_F values for the unconstrained regression indicate that increasing the number of cluster spectra from 70 to 81 is the last addition that provides any sensible improvement to the regression. The reduction in residuals for the constrained regression suggests that the last important change occurs in the transition from 43 to 70 spectra. Apparently, ~70 spectra adequately describe the scene background. This observation is supported by the fact that the number of principal-component singular values larger than the sensor NESR is also ~70.

6.7 Pixel Amalgamation

The spectral results presented in the previous two subsections were for a single pixel. In this subsection, spectral results are presented for the amalgamation of a large number of pixel spectra covering a large spatial extent of a plume. The expectation is that the amalgamation will improve the extraction statistics for gas contrast coefficients. The amalgamation is carried out in the following manner. Regression (constrained or unconstrained) is performed for each pixel in a selected set of pixels. The modeled contrast spectrum (40) and residual spectrum (42) are constructed and averaged over the selected pixels:

$$C_{RA}(\lambda)=\frac{1}{P}\sum_{p=1}^{P}\left|C_{Rp}(\lambda)\right| \tag{43}$$

$$\delta_A(\lambda)=\frac{1}{P}\sum_{p=1}^{P}\delta_p(\lambda). \tag{44}$$

The amalgamated *data* spectrum is taken as

$$C_A(\lambda)=C_{RA}(\lambda)+\delta_A(\lambda). \tag{45}$$

Use of the absolute value in (43) allows pixel results that appear either in emission or in absorption to be accumulated together. A straightforward averaging of pixel spectra does not allow this. The accumulation of the residual spectra diminishes the effects of sensor noise. If the selected pixels cover a region of sufficiently different underlying spectra, clutter is also suppressed If the underlying surface material is nearly the same under all selected pixels, little clutter suppression results. The final step is a regression of the data spectrum (45) on the model (41) to obtain the gas contrast coefficients. This regression is a straightforward, N-parameter unconstrained regression since all constraints (if any) have been applied in the regression on each pixel.

Another amalgamation approach is to perform a straightforward averaging of the gas regression coefficients obtained at each pixel

$$C_n = \frac{1}{P}\sum_{p=1}^{P}\left|C_{np}\right|. \tag{46}$$

The error in C_n can be estimated either as an accumulation of coefficient errors at each pixel

$$\sigma_n = \frac{1}{P}\sqrt{\sum_{p=1}^{P}\sigma_{np}^2}\ , \tag{47}$$

or as the standard deviation of the mean

$$\sigma_n = \frac{1}{P}\sqrt{\sum_{p=1}^{P}\left(C_{np} - C_n\right)^2}\ . \tag{48}$$

Mean values and error estimates obtained from the three approaches are comparable. Of the three error estimates, the one obtained by the method embodied in (43–45 and 41) is generally the most conservative, *i.e.*, it produces the largest estimates.

Pixel amalgamation was applied to Plume 1 in Shot 83. Spatial regions relevant to the application are shown in Figure 28. Clusters were constructed in the large upper rectangle surrounding the plume, but outside (on white pixels) the exclusion mask. This mask was constructed as outlined in Subsection 5.2. A cluster parameter of $\theta = 25$ µf resulted in 62 clusters. Two clusters containing the sensor artifact mentioned in Subsection 6.3 were removed from the set. The selected pixels for the amalgamation consisted of all pixels, both inside the smaller of the two upper rectangles and inside the plume mask (on the black pixels). The set contains 3,513 pixels. Unconstrained and constrained regressions with backward elimination of gases were applied. The starting target suite consisted of all eight gases. Unconstrained regression results are shown in Figure 29a and the upper left section of Table 9. Backward elimination removed nitrous oxide ($P_T = 0.50$) and ethylene ($P_T = 0.23$). The

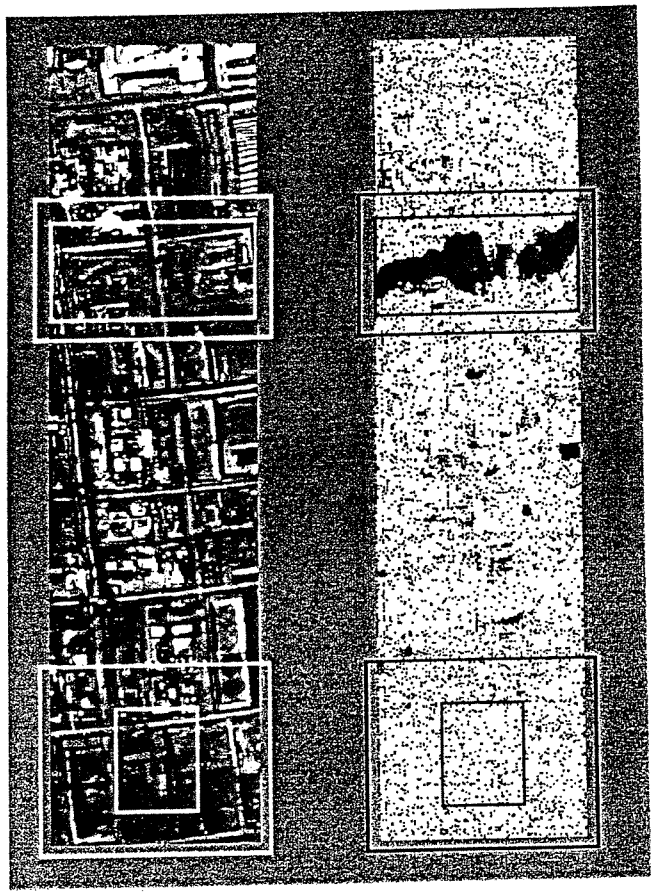

Figure 28. Cluster analysis regions for Shot 83. Regions of cluster and pixel-amalgamation analysis are shown superposed on both the 12-μm thermal image (left) and the plume exclusion mask (right).

remaining six gases survived the final regression with $P_T = 1.00$. Unlike the single-pixel results of Table 4, all gases were detected here with positive contrast coefficients in the final regression. Constrained regression results are shown in Figure 30a and the upper right section of Table 9. Backward elimination removed only nitrous oxide ($P_T = 0.73$). All remaining gases survived with $P_T = 1.00$. In this regression, different numbers of target gases and background basis spectra survive the constraints at each pixel. The amalgamation averages are $N = 4.75$ and $M = 6.33$. The RMS residual is 0.92 μf and is close to the NESR of the sensor (Table 1). The amalgamation is providing near-optimum regression. Statistical tests (Appendix 2) reveal that the gas-contrast coefficients for carbon dioxide and ammonia are unchanged between the unconstrained and constrained regressions. With the exception of methane, coefficients obtained with constrained regression are 1.7 to 3.4 times larger than those obtained with the unconstrained regression. This increase is consistent with the increased *stiffness* resulting from the constraint that the background coefficients be positive.

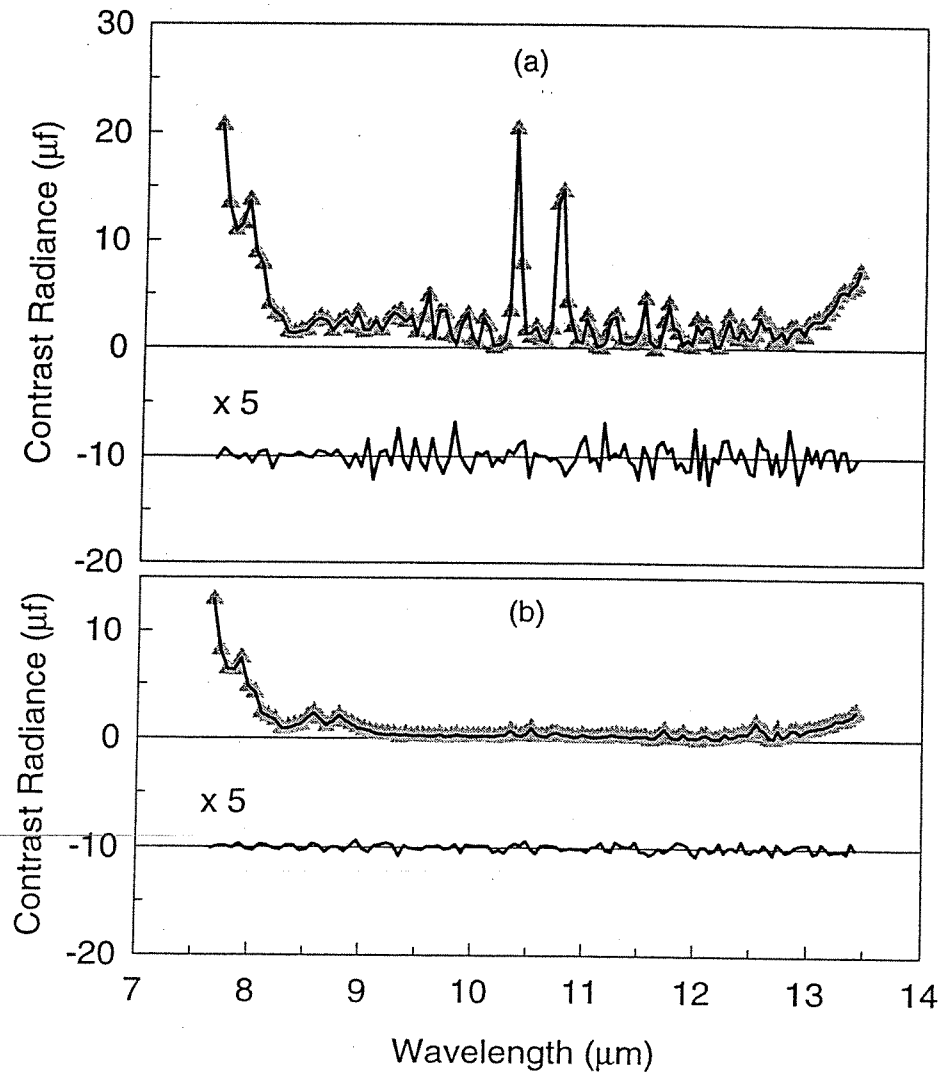

Figure 29. Pixel amalgamation on Plume 1 of Shot 83 using unconstrained regression. (a) The spectrum with gray symbols is the data spectrum (Equation 45). The solid line through the points is the regression fit (Equation 43). The lowest curve is the residual spectrum (Equation 44). The RMS of the residual spectrum is $\sigma =$ 0.22 μf. The residual spectrum is magnified by a factor of 5. (b) Pixel amalgamation on an upwind region free of plume activity using unconstrained regression. The legend is the same as (a) with the exception that the RMS of the residual spectrum is $\sigma = 0.07$ μf.

Table 9. Pixel Amalgamation Contrast Coefficients for Plume 1 in Shot 83

Gas	|C| (ppmm-μf)	SNR	|C| (ppmm-μf)	SNR
On Plume	**Unconstrained** $N = 6$ $M = 61$ $\sigma = 0.22$ μf		**Constrained** $N = 4.75$ $M = 6.33$ $\sigma = 0.92$ μf	
CH_4	$1.80 \pm 0.03 \times 10^5$	67.8	$1.55 \pm 0.09 \times 10^5$	16.7
H_2O	$4.74 \pm 0.34 \times 10^7$	13.8	$1.04 \pm 0.12 \times 10^8$	8.6
CO_2	$5.57 \pm 0.25 \times 10^6$	22.8	$6.66 \pm 0.85 \times 10^6$	7.8
NO_2	$8.63 \pm 0.63 \times 10$	13.8	$1.46 \pm 0.22 \times 10^4$	6.7
NH_3	$1.26 \pm 0.01 \times 10^4$	132.1	$1.31 \pm 0.04 \times 10^4$	36.6
SO_2	$1.15 \pm 0.08 \times 10^4$	15.1	$3.93 \pm 0.27 \times 10^4$	14.8
C_2H_4	—	—	$3.50 \pm 0.59 \times 10^3$	6.0
Off Plume	**Unconstrained** $N = 6$ $M = 61$ $\sigma = 0.07$ μf		**Constrained** $N = 1.71$ $M = 6.56$ $\sigma = 0.80$ μf	
CH_4	$1.09 \pm 0.02 \times 10^5$	66.4	—	—
N_2O	—	—	$6.52 \pm 1.10 \times 10^3$	5.9
H_2O	$3.17 \pm 0.21 \times 10^7$	14.9	—	—
CO_2	$2.11 \pm 0.15 \times 10^6$	14.0	—	—
NO_2	$2.00 \pm 0.39 \times 10^3$	5.2	$3.12 \pm 1.12 \times 10^3$	2.8
NH_3	$3.30 \pm 0.63 \times 10^2$	5.2	—	—
SO_2	$1.28 \pm 0.05 \times 10^4$	27.3	—	—
C_2H_4	$6.25 \pm 1.03 \times 10^2$	6.1	$1.68 \pm 0.49 \times 10^3$	3.4

Pixel amalgamation was repeated on an upwind region of the image free of plume activity. The analysis was carried out as above, but on the lower set of rectangles in Figure 28. A cluster dispersion parameter of $\theta = 27$ μf resulted in 76 cluster spectra of which two containing the reoccurring sensor artifact were eliminated. The number of pixels in the amalgamation is 3,315. Spectral results for unconstrained and constrained regressions are shown in Figures 29b and 30b and the lower section of Table 9. Despite the extreme unlikelihood that plume gases occur at this site, unconstrained regression has contrived to detect all gases except nitrous oxide with $P_T > 0.99$. Most disconcerting are the large coefficients obtained for methane and water vapor. They are greater than half the corresponding values obtained in the on-plume regression. These gases account for the large signal in the wing below ~8 μm in Figure 29b. Carbon dioxide provides a noticeable, but smaller wing above ~13 μm. With constrained regression, only three plume gases (nitrous oxide, ethylene, and nitrogen dioxide) are deemed significant. For all three gases, $P_T > 0.99$. The contrast spectrum is shown in Figure 30b and is not nearly so egregious as that obtained with unconstrained regression. The wings below ~8 and above ~13 μm are quite small and not noticeably larger than the residual spectrum. Nevertheless, even though the background constraints provide significantly increased stiffness to the regression, there is still enough flexibility to provide bogus detection. This flexibility suggests that gas concentrations may still be somewhat underpredicted in the on-plume constrained regression.

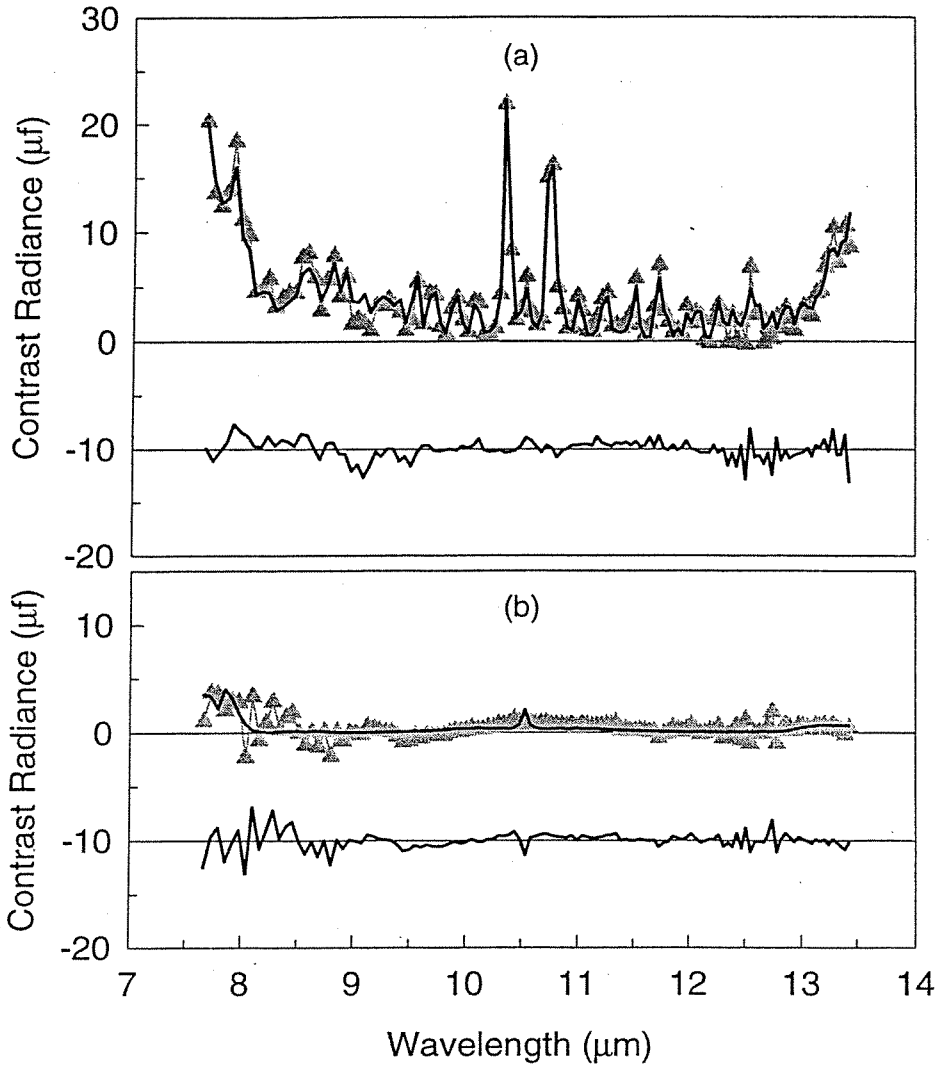

Figure 30. Pixel amalgamation on Plume 1 of Shot 83 using constrained regression. (a) The legend of Figure 29a applies with the exception that the RMS of the residual spectrum is $\sigma = 0.92$ μf and the residual spectrum is not magnified. (b) Pixel amalgamation on an upwind region free of plume activity using constrained regression. The legend of Figure 29b applies with the exception that the RMS of the residual spectrum is $\sigma = 0.80$ μf and the residual spectrum is not magnified.

6.8 Column Density and Plume Temperature Extraction

The target extraction results to this point have been the gas contrast coefficient defined by (15). For a single gas, and with (25), the contrast can be written as

$$C = c_P\left[B_P(\bar{\lambda}) - L_0(\bar{\lambda})\right] + c_A\left[B_P(\bar{\lambda}) - B_A(\bar{\lambda})\right]. \tag{49}$$

The contrast is a function of two unknown quantities: the column density, c_P, and the plume radiance, $B_P(\lambda)$. The ambient values c_A and $B_A(\lambda)$ are presumed known. With contrast results from a single pixel, solution for these two parameters is not possible since there is only one equation. Some extra information is required to solve the problem. In this section, a spatial-degradation approach is taken to obtain estimates of these separate quantities. In effect, the information needed is obtained by sacrificing spatial resolution.

Equation (49) is a linear relationship between the contrast C and the underlying surface radiance $\overline{L}_0$ with slope $b = -c_P$ and intercept $a = c_P B_P + c_A(B_P - B_A)$. (The dependence on $\overline{\lambda}$ has been suppressed.) Consider a spatial subregion $n \times m$ pixels in extent surrounding a pixel. Assume that the plume temperature and column density are constant within this subregion. Then we have $n \times m$ equations to determine two parameters, so long as the set of equations is not ill conditioned. The set will be ill conditioned if the subregion contains degenerate underlying spectra. The condition of the extraction, therefore, relies on the presence of underlying surface clutter. A least-squares line fit is made to the set of $n \times m$ pairs of C and $\overline{L}_0$ to obtain a and b and corresponding error estimates σ_a and σ_b. The independent variable $\overline{L}_0$ can be obtained in general from (33) with interpolation to $\overline{\lambda}$. An alternative method is to determine the surface brightness temperature by (3) in a spectral channel free of gas activity and convert it to radiance at $\overline{\lambda}$ with (2). This latter method was used here and justified by the fact that the site consists primarily of graybody spectra. The column density and plume radiance are then given by $c_P = -b$ and $B_P = (a + c_A B_A)/(-b + c_A)$ with error estimates $\sigma_c = \sigma_b$ and $\sigma_{B_P} = |\sigma_a - B_P \sigma_b|/(c_P + c_A)$. The error estimate for B_P takes account of the fact that a and b are nearly perfectly anti-correlated. Results are retained only if the retrieval SNRs $SNR_c = c/\sigma_c$ and $SNR_{B_P} = B_P/\sigma_{B_P}$ are larger than a threshold value. The extracted value of B_P is converted to temperature using the inverse Planck function relationship (3) with $\overline{\lambda}$ as the wavelength.

An application of the separation was made on Plumes 1, 4, and 5 in Shot 96. Unconstrained regression was made with ammonia as the only target gas and with the 70 spectra of the $\theta = 55$ µf cluster set (Subsection 6.3) as the background basis set. Unconstrained regression is acceptable here since ammonia is only mildly underpredicted (<15%). Additionally, $c_A = 0$ since there is no ambient ammonia contribution. A 7×7 degradation grid was used. Rejection SNRs were set at 5 for both c_P and B_P. The application was made to each pixel in the image. The linear least-squares fit that obtains for one of the pixels is shown in Figure 31. The 49 spectra of the subregion containing the pixel are shown in Figure 32. Although indicative of a common surface material, the spread in temperature of these spectra provides sufficient clutter to effect a separation of column density and temperature. The least-squares line through the data of Figure 31 yields $c_P = 70 \pm 5$ ppmm and $B_P = 850 \pm 80$µf. The implied plume temperature is $T_P = 18 \pm 6$°C. The extracted column-density and plume-temperature images are shown in Figure 33. The *blockiness* of the images results from the 7×7-pixel spatial degradation. Discontinuities occur in the extraction images wherever the plumes pass over regions of low spatial surface clutter. The extracted parameters were averaged over the downwind region of the plume where it appears entirely in absorption. The results are $c_P = 57 \pm 4.8 \pm 1$ ppmm, $B_P = 860 \pm 80 \pm 2$ µf and $T_P = 18.7 \pm 5.4 \pm 0.1$°C. The first error number is the standard deviation. The second error number is the standard deviation of the mean based on 1664 points for c_P and 773 points for B_P and T_P.

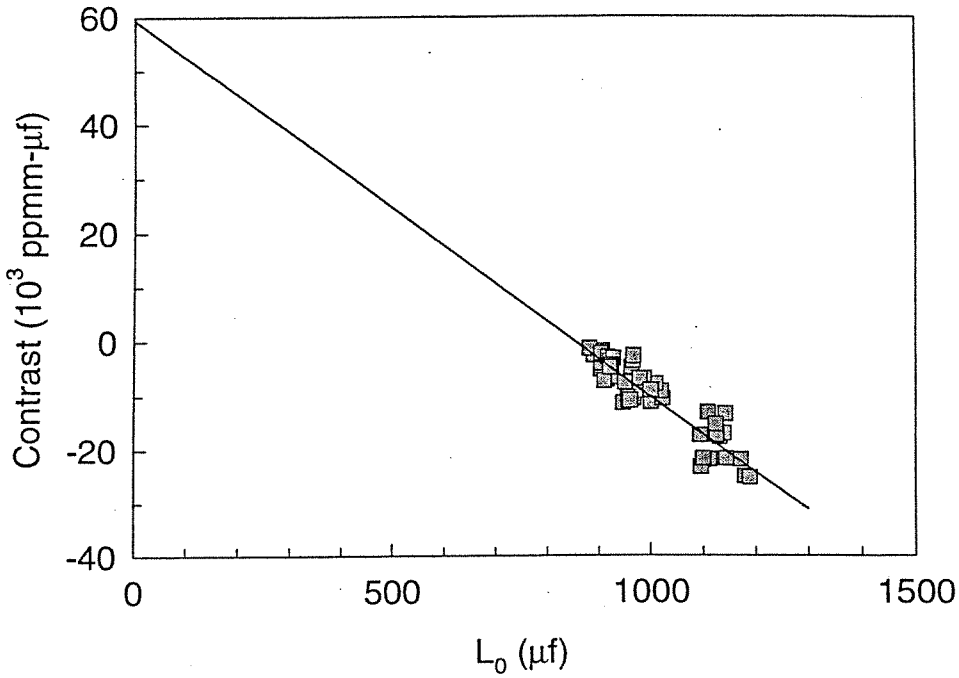

Figure 31. Gas contrast versus underlying surface radiance for a 7 x 7 spatial region around a selected example pixel in Plume 1 of Shot 96. The solid line is the least-squares regression fit to the points.

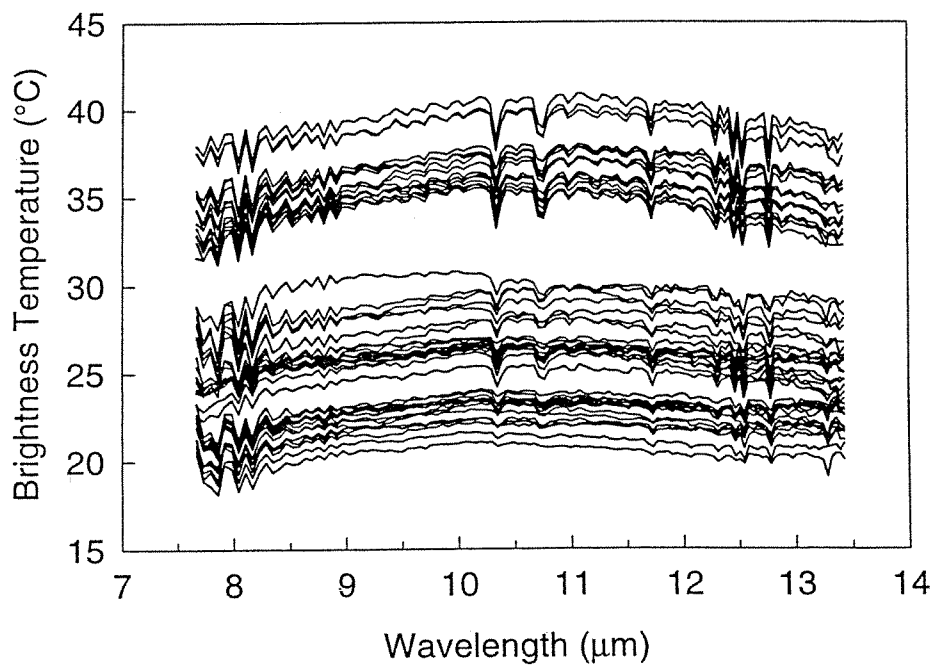

Figure 32. Spectra within a 7 x 7 sub-region around example pixel in Plume 1 of Shot 96.

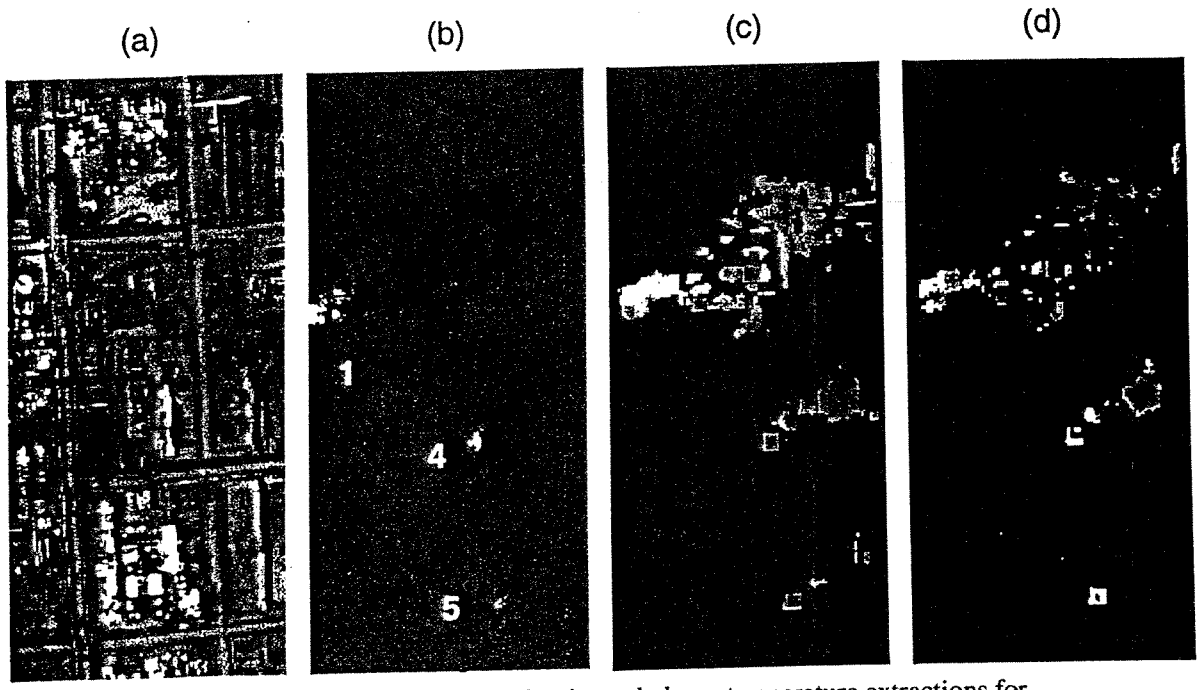

Figure 33. Ammonia column-density and plume-temperature extractions for Shot 96. (a) 12-μm thermal image. (b) Ammonia contrast image. (c) Extracted ammonia column density. This image is displayed on a logarithmic intensity scale so that the two smaller plumes can be seen. (d) Extracted plume temperature.

The downwind variations of these parameters for Plume 1 are shown in Figure 34. The results were averaged in 5-pixel (~10-m-wide) bins across the width of the image and plotted against the distance x down the plume axis from the stack location. Beyond 75 m, the column density displays a steady decrease towards zero as the plume disperses. The temperature decreases steadily towards an asymptotic value consistent with the EDAS estimate of ~14°C for the ground-level air temperature at the site. No corrections were made for stack height or plume loft [*Hanna et al.*, 1982].

6.9 Plume Gas Properties

Results obtained from the pixel amalgamation analysis of Subsection 6.7 on Shot 83 and the extraction results of the preceding subsection on Shot 96 were used to estimate gas concentrations and mass flow rates within Plume 1. Shots 83 and 96 were taken within 6 min of each other. It is assumed that the plume conditions are the same for each Shot.

Mass Flow Rate. The column-density and plume-temperature data of Figure 34 were fit to a simple plume model in which the stack gases mix uniformly with entrained ambient air within a circular cone and rapidly equilibrate to the wind speed (Figure 35). (Other plume models are discussed by *Hanna et al.* [1982] and *Kuo et al.*, [2000].) The plume model diameter is $d = d_0 + 2x\sin(\alpha/2)$ where d_0 is the diameter of the cone at $x = 0$, and α is the full cone-expansion angle. Mass density and temperature within the plume are modeled as

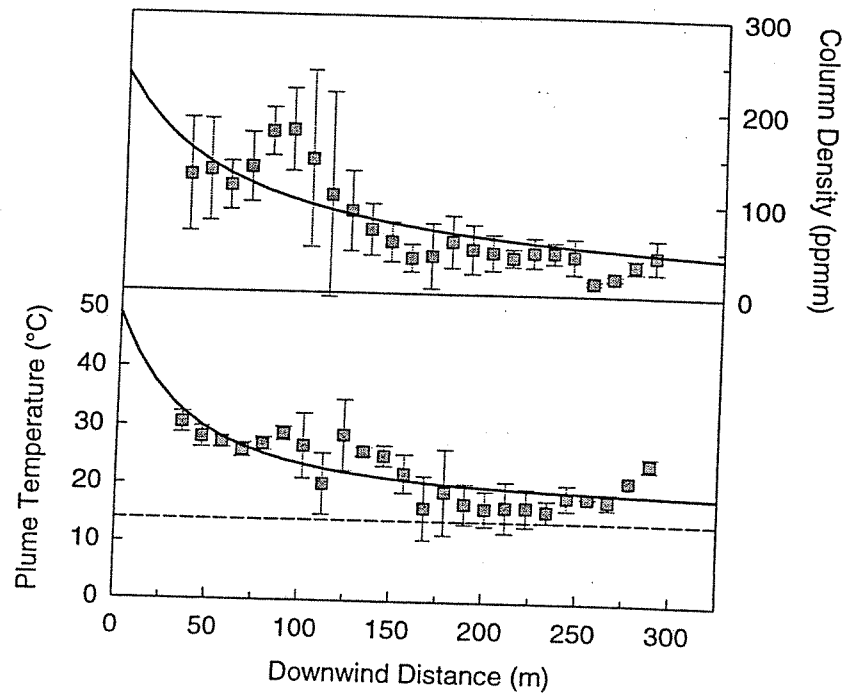

Figure 34. Downwind variation of ammonia mean column density and mean plume temperature across the transverse dimension of Plume 1 in Shot 96. The curves are variations for a cone-dispersion model (Equations 51 and 52). The dashed line is the EDAS estimate of surface air temperature (14 °C).

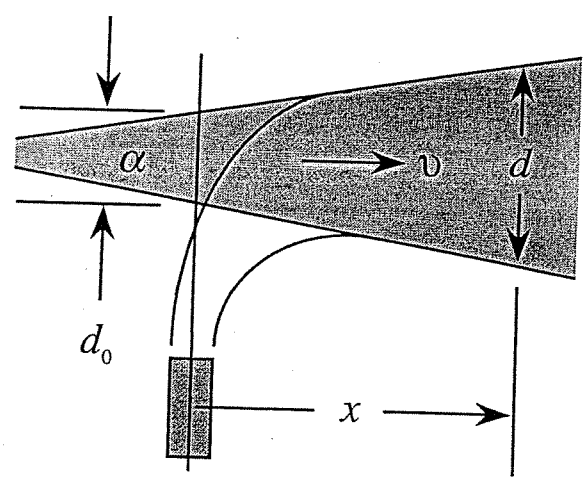

Figure 35. Cone-Dispersion Plume Model.

$$\rho = \left(\frac{d_0}{d}\right)^2 \rho_0 + \left[1 - \left(\frac{d_0}{d}\right)^2\right] \rho_A \tag{50}$$

$$T_P = \left(\frac{d_0}{d}\right)^2 T_0 + \left[1 - \left(\frac{d_0}{d}\right)^2\right] T_A . \tag{51}$$

ρ_0 and T_0 are the density and temperature at $x = 0$. ρ_A and T_A are ambient atmospheric values. For ammonia, $\rho_A = 0$. Molecular number density is $n = \rho N_A / \mu$, where $N_A = 6.023 \times 10^{23}$ molecules/mole, and $\mu = 17$ g/mole is the atomic weight of ammonia from Table 2. The total gas pressure is assumed to be 1 atm. The total molecular number density is $n_T = 2.686 \times 10^{25} (T_{STP}/T)$ molecules/m^3. $T_{STP} = 273.15$K. Column density (in ppmm) averaged over the transverse dimension of the plume is

$$c = 10^6 \left(\frac{n}{n_T}\right) \frac{\pi}{4} d . \tag{52}$$

A nonlinear fit of the data for c and T_P to the functional forms (51) and (52) gave parameter values $\alpha = 15°$, $d_0 = 21$ m, $\rho_0 = 8.9 \times 10^{-6}$ kg/m^3, $T_0 = 49$°C and $T_A = 17$°C. (d_0, ρ_0 and T_0 describe conditions within the plume model at $x = 0$. They are *not* conditions at the stack exit plane.) The dispersion angle and mean plume width (65 ± 20 m) are consistent with estimates made directly from the imagery. The ambient temperature is consistent with the EDAS estimate of 14°C. The model result for c and T_P are shown in Figure 34. The RMS residuals of the fit are 28 ppmm for c and 3.1°C for T_P. The mass flow rate is $\dot{m} = (\pi/4) d^2 \rho \ \upsilon = (\pi/4) d_0^2 \rho_0 \upsilon$, where υ is the ambient wind speed. With the EDAS estimate $\upsilon \sim 3$ m/s (and an arbitrary error estimate of ± 1 m/s), the ammonia flow rate is $\dot{m} = 0.009 \pm 0.003$ kg/s = 70 ± 30 lb/h.

Gas Concentrations. Table 10 displays concentration results for Plume 1. The second column repeats the gas contrast radiances, C, obtained in the pixel amalgamation analysis of Subsection 6.7 (the *constrained, on-plume* entries in Table 9). The contrast values are tabulated as negative to reflect the fact that the plume is seen almost entirely in absorption. The mean plume temperature, obtained from the extraction analysis of Subsection 6.8, is $T_P = 18.7 \pm 0.1$°C. This temperature is close enough to the reference temperatures for the water vapor, carbon dioxide, and nitrogen dioxide spectral absorption coefficients (Figure 1) that no temperature scalings of the contrast radiances were made. The third column shows the contrast radiances transformed to temperature units with (4), the $\bar{\lambda}$ values of Table 2, and the mean plume temperature. An advantage of this unit is that molar ratios can be obtained directly as ratios of contrast radiance. Whatever temperature contrast obtains will cancel. Because $\bar{\lambda}$ varies with gas, this cancellation does not occur with contrast radiance expressed in radiance units. The fourth column of Table 10 lists the ambient concentrations, ρ_A, for the detected gases. The water vapor entry is the mean of the EDAS and ISAC estimates. The contribution to contrast radiance from ambient gases [from (14)] is $C_A = \rho_A (T_P - T_A)$, where T_A is ambient air

Table 10. Gas Concentrations in Plume 1

Gas	C (ppmm-μf)	C (ppmm-°C)	ρ_A (ppm)	C_P (ppmm-°C)	ρ_P (ppm)	$\rho_P + \rho_A$ (ppm)
CH_4	$-1.55 \pm 0.09 \times 10^5$	$-9.5 \pm 0.6 \times 10^3$	1.5	$-1.0 \pm 0.1 \times 10^4$	12 ± 6	13 ± 6
H_2O	$-1.04 \pm 0.12 \times 10^8$	$-6.6 \pm 0.8 \times 10^6$	$10^4 \pm 500$	$-9.7 \pm 0.8 \times 10^6$	11000 ± 5000	21000 ± 6000
CO_2	$-6.66 \pm 0.85 \times 10^6$	$-6.7 \pm 0.9 \times 10^5$	360	$-7.8 \pm 0.9 \times 10^5$	900 ± 400	1300 ± 400
NO_2	$-1.46 \pm 0.22 \times 10^4$	$-1.1 \pm 0.2 \times 10^3$	0.001	$-1.1 \pm 0.2 \times 10^3$	1.3 ± 0.7	1.3 ± 0.7
NH_3	$-1.31 \pm 0.04 \times 10^4$	$-9.4 \pm 0.3 \times 10^2$	0.004	$-9.4 \pm 0.3 \times 10^2$	1.1 ± 0.5	1.1 ± 0.5
SO_2	$-3.93 \pm 0.27 \times 10^4$	$-2.5 \pm 0.2 \times 10^3$	0.001	$-2.5 \pm 0.2 \times 10^3$	2.8 ± 1.4	2.8 ± 1.4
C_2H_4	$-3.50 \pm 0.59 \times 10^3$	$-2.5 \pm 0.4 \times 10^2$	—	$-2.5 \pm 0.4 \times 10^2$	0.3 ± 0.1	0.3 ± 0.1
				Total =	12000 ± 6000	23000 ± 6000

temperature. The mean air temperature obtained from EDAS and ISAC estimates is $T_A = 14.0 \pm 0.2$°C. C_A was subtracted from the values in the third column to give the contrast radiance contribution, C_P, from stack gases alone. Only water vapor and carbon dioxide are affected to any sensible extent. The stack contribution is tabulated in the fifth column. The sixth column of Table 10 shows the stack contributions to gas densities, ρ_P, that obtain when the temperature contrast and plume diameter are divided out. Temperature contrast is the difference between the mean plume temperature and the mean underlying surface temperature. The surface temperature was obtained from the region under the plume using radiance data from the 12.15-μm spectral channel. None of the plume gases is active in this channel. The surface temperature is $T_S = 32 \pm 5 \pm 0.1$°C. The temperature contrast is thus $\Delta T = T_P - T_S = -13$°C. Because the gas contrast error already carries the pixel-to-pixel variations in both column density and thermal contrast, the error in ΔT is not included in the error propagation for ρ_P. The mean model plume diameter from Subsection 6.8 is $D = 65 \pm 20$ m. It is assumed here that the diameter of the plume is the same in the plane of the imagery as it is for a vertical LOS through the plume. The last column of Table 10 lists the total concentrations $\rho_P + \rho_A$.

The total carbon dioxide concentration is 1300 ± 400 ppm and is about a factor of 4 larger than the ambient value. The total water vapor concentration is 21000 ± 6000 ppm and is about twice the ambient value. Concentrations of the remaining gases are of order 0.1 to 10 ppm and, although much smaller than the concentrations of carbon dioxide and water vapor, are well above ambient values. The sum of all stack concentrations is 23000 ± 6000 ppm.

7. Summary and Discussions

Methods for detecting and quantifying gas effluents in industrial-stack plumes using thermal-infrared hyperspectral imagery were demonstrated. Principal-component projection provides detection capability for moderate to strong plumes when there is no prior knowledge of what gases might be present. Use of the scene spectral clutter covariance matrix for the construction of these components is superior to use of the correlation or noise-adjusted matrices in producing identifiable plume structures. Projection-pursuit methods [*Ifarraguerri and Chang*, 2000] may provide better detection capability. Traditional spectral matched filtering provides optimum detection when it is known what gases are likely to be present. If the target plume area is a sizable fraction of the total image area, an iterative application of matched filtering can increase the detection fidelity. Thresholding of principal-component projections or spectral matched filter output images provides a convenient method to construct spatial masks that differentiate between pixels containing plume-like spectral structure and those that do not. For both principal-component projection and spectral matched filtering, careful visual inspection of the output images is required to identify small or weak plumes. Thresholding of spectral matched filter outputs, even at SNR values as low as 2, will miss plumes that are readily apparent to the eye. A few very small plumes were apparent in some spectral matched filter output images. They consisted of no more than a single hot-stack pixel and one or two downwind pixels containing identifiable gas emissions. These plumes are being addressed in a study of techniques designed to detect small targets [*Schweizer and Moura*, 2000; *Schweizer and Moura*, 2001; *Yu et al.*, 1997; *Funk et al.*, 2001].

Unconstrained linear least-squares regression provides some improvement over spectral matched filtering in obtaining quantitative gas information. However, the unbridled flexibility inherent in the method mis-models the underlying surface radiance spectrum to such an extent that gas concentrations can be underpredicted by as much as a factors of 3. The largest errors result for gases with broad spectral features. Effects of mis-modeling cannot be detected in the spectral structure of the residual spectrum. These deleterious effects obtain with background basis sets composed either of spectra extracted from the imagery or eigenvector spectra of spectral covariance matrices constructed from the imagery. Quantitative results can be obtained with constrained regressions in which all gas contrast radiance coefficients are required to have the same sign, and the background basis set is required to consist of physically meaningful spectra represented by non-negative expansion coefficients. It is not immediately evident how to impose equivalent constraints in regressions using basis sets of eigenvectors. All applications of unconstrained regression employing eigenvectors must be viewed only as detection methods with little quantitative capability. As such, they have little to offer over the more easily implemented spectral matched filtering methods.

The effect of spectral line correlation was shown to be significant for plume gases that also contribute significantly to atmospheric attenuation. For the current collection geometry and humidity conditions, the effective emission coefficient for water vapor is reduced by a factor of ~15. The factor for carbon dioxide and methane is ~3. The remaining gases considered here are not seriously affected.

Background basis sets consisting of manually selected pixel spectra and spectra derived from clustering algorithms were considered. A single-pass clustering algorithm $(OP)^2$ was formulated that is amenable to unsupervised implementation, is fast, and generates spectra that account for thermal variation in the data. Unlike the K-Means or ISODATA algorithms, $(OP)^2$ does not impose total within-cluster sum-of-squares minimization. This aspect of clustering may be useful in surface-material classification applications, but is superfluous and costly in generating background basis sets used for gas detection. Regression results obtained with K-Means clusters were found to be virtually identical to regression results obtained with $(OP)^2$ clusters.

Endmember extraction methods were not employed in the current study. Application of this method to thermal data requires three steps. First, the thermal variation needs to be removed from the data. The resulting pixel spectra then need to be processed by a traditional endmember extraction algorithm. Finally, thermal variation needs to be reestablished on the endmembers to generate suitable background radiance spectra. The first and third steps are rarely addressed in the endmember-extraction literature. *Stocker and Schaum* [1997] comment on two ways the first step might be done: converting the radiance spectra to emissivity spectra and projecting out data variations in the spectral direction of the local temperature gradient. Given the success of clustering in providing suitable background spectra for gas analysis applications, endmember extraction appears overly complicated and unlikely to provide any significant advantage.

Application of constrained regression is at least a factor of 30 slower than unconstrained regression. It is usually impractical to apply constrained regression to an entire image. A practical approach is to employ unconstrained regression and then to *correct* the regression result based on results obtained with both unconstrained and constrained regressions on a smaller, selected set of image pixels. Alternatives to constrained regression are being considered. Inspection of Figures 21 and 23 and Table 4 suggests that simple off-plume background subtraction can yield results that are nearly as good as those obtained with constrained regression. A straightforward search through an entire image (hundreds of thousands of pixels) for the closest off-plume background pixel that matches every plume pixel (thousands of pixels), however, is impractical. Methods to limit the search need to be implemented. An alternative approach is to use a single cluster spectrum as the background. In this *closest-cluster* approach, the number of clusters is not limited by $M < J - N$ as it is when the clusters are used as backgrounds in regressions. Preliminary studies suggest that basis sets of order 100 to 1000 clusters would be suitable.

The T-Test was used to assess the significance of gas detection in both unconstrained and constrained regressions. The addition F-Test was used to determine that a background basis set of ~70 members is optimum in describing the clutter of the current target site.

A method was demonstrated to extract gas column density and plume temperature from measurements of gas contrast radiance in optically thin plumes. The method employs spatial degradation of the data to remove the indeterminacy inherent in trying to estimate two parameters from one measurement. The indeterminacy is removed only over regions of sufficient thermal or spectral clutter in the underlying surface. All aspects of the current study were limited to analyses of optically thin gases. Non-thin conditions occur in some of the plumes close to the stack exit points. Various linear and nonlinear methods are being examined for use in non-thin gas analysis. The radiance model for thin gases was obtained here by expanding the plume emissivity only to first order in gas column

density [see (12)]. Higher order expansions can be used for conditions not too far beyond thin. Expansion requires the selection of a suitable gas absorption law. For gases with dense vibration-rotation line structure (*e.g.*, sulfur dioxide), Beer's law is appropriate. For gases with sparse line structure (*e.g.*, ammonia), narrowband-model formulations are needed. In either case, the linear radiance model (17) can be retained by thinking of the moments $k_n(\lambda)$, $k_n^2(\lambda)$, $k_n^3(\lambda)$, ... appearing in the expansion as representing absorption spectra for different, but highly overlapping, gases. In addition to the same-sign constraint imposed for multiple target gases, regression requires the added constraint that the gas contrast coefficients satisfy the alternating sign of the expansion coefficients. *Hayden and Noll* [1997] discuss this expansion approach within the limitations of unconstrained regression (the OBS method mentioned in Appendix 1). They also note that the indeterminacy in separating column density and plume temperature does not occur in non-thin gases.

Column-density and plume-temperature data for Plume 1 in Shot 96 were fit to a cone-dispersion plume model and used to estimate gas flow rate. A flow rate of 0.009 ± 0.003 kg/s (70 ± 30 lb/h) was found for ammonia. Large errors obtain for this and other estimates owing to large errors in contrast radiance extraction, contrast temperature estimation, wind speed estimation, and plume diameter estimation. The error in diameter estimation must include the error incurred in assuming that the LOS depth through the plume is the same as the diameter obtained from the imagery. Mean gas concentrations for Plume 1 were estimated from an amalgamation of pixel spectra. The estimated total concentrations for carbon dioxide and water vapor are 1300 ± 400 and 21000 ± 6000 ppm, respectively. The concentrations of all species except carbon dioxide and water vapor range from 0.1 to 10 ppm.

References

Althouse, M.L.G. and Chang, C.-I., Target Detection in Multispectral Images Using the Spectral Co-Occurrence Matrix and Entropy Thresholding, *Opt. Eng., 34*, 2135-2148, 1995.

Bennett, C.L., Carter, M.R., Fields, D.J. and Lee, F.D., Infrared Hyperspectral Imaging Results from Vapor Plume Experiments, *Proc. SPIE, 2480*, 435-444, 1995.

Bevington, P.R., *Data Reduction and Error Analysis for the Physical Sciences*, McGraw Hill, New York, 195-202, 1969.

Carlson, R.C., Hayden, A.F. and Telfair, W.B., Remote Observations of Effluents from Small Building Smokestacks using FTIR Spectroscopy, *Applied Optics, 27*, 4952-4959, 1988.

Carr, L., Fletcher, L., Holland, P., Leonelli, J., McPherrin, D. and Althouse, M., Characterization of Filtered FLIR Systems Designed for Chemical Vapor Detection and Mapping, *Proc. SPIE, 1309*, 90-103, 1990.

Carter, M.R., Bennett, C.L., Fields, D.J. and Hernandez, J., Gaseous Effluent Monitoring and Identification Using an Imaging Fourier Transform Spectrometer, *Proc. SPIE, 2092*, 16-26, 1993.

Collins, B.H., Olsen, R.C. and Hackwell, J., Thermal Imagery Spectral Analysis, *Proc. SPIE, 3118*, 94-105, 1997.

Draper, N.R. and Smith, H., *Applied Regression Analysis*, John Wiley and Sons, New York, 1966.

Edner, H., Sandsten, J., Saito, Y., Smith, J., Svanberg, S. and Weibring, P., Novel Remote Gas Monitoring and Imaging in the IR Spectral Region, *CLEO/Pacific Rim '99. The Pacific Rim Conference on Lasers and Electro-Optics, 1999, Vol. 2*, 577-578, 1999.

EPA, http://www.epa.gov/ttn/emc/ftir/welcome.html

Funk, C.C., Theiler, J., Roberts, D.A. and Borel, C.C., Clustering to Improve Matched Filter Detection of Weak Gas Plumes in Hyperspectral Thermal Imagery, *IEEE Trans. Geosci. and Remote Sensing, 39*, 1410-1420, 2001.

Gittins, C.M. and Marinelli, W.J., AIRIS Multispectral Imaging Chemical Sensor, *Proc SPIE, 3383*, 65-74, 1998.

Goody, R.M., *Atmospheric Radiation - I. Theoretical Basis*, Clarendon Press, Oxford, 122, 1964.
Hackwell, J.A., Warren, D.W., Bongiovi, R.P., Hansel, S.J., Hayhurst, T.L., Mabry, D.J., Sivjee, M.G. and Skinner, J.W., LWIR/MWIR Imaging Hyperspectral Sensor for Airborne and Ground-Based Remote Sensing, *Proc. SPIE, 2819*, 102-107, 1996.

Hall, D.J. and Khanna, D.K., The ISODATA Method Computation for the Relative Perception of Similarities and Differences in Complex and Real Data, in *Statistical Methods for Digital Computers, Vol. III of Mathematical Methods for Digital Computers*, Enslein, K., Ralston, A. and Wilf, H. S., Editors, John Wiley and Sons, New York, 340-373, 1977.

Hanna, S.R., Briggs, G.A. and Hosker, R.P., Jr., Handbook on Atmospheric Diffusion, DOE/TIC-11223 (DE82002045), National Technical Information Service, U. S. Department of Commerce, Springfield, VA 22161, 1982.

Hanson, R.J., Linear Least Squares with Bounds and Linear Constraints, *SIAM J. Sci. Stat. Comput., 7*, 826-834, 1986.

Hanst, P.L and Hanst, S.T., Infrared Spectra for Quantitative Analysis of Gases, Infrared Analysis, Inc., 1334 North Knollwood Circle, Anaheim, CA, 92801, 1993.

Harsanyi, J.C. and Chang, C.-I., Hyperspectral Image Classification and Dimensionality Reduction: An Orthogonal Subspace Projection Approach, *IEEE Trans. Geosci. Remote Sensing, 32*, 779-785, 1994.

Hartigan, J.A. and Wong, M.A., Algorithm AS 136: A *K*-Means Clustering Algorithm, *Applied Statistics, 28*, 100-108, 1979.

Hayden, A., Niple, E. and Boyce, B., Determination of Trace-Gas Amounts in Plumes by Use of Orthogonal Digital Filtering of Thermal-Emission Spectra, *Applied Optics, 35*, 2802-2809, 1996.

Hayden, A. and Noll, R., Remote Trace Gas Quantification Using Thermal IR Spectroscopy and Digital Filtering Based on Principal Components of Background Scene Clutter, *Proc. SPIE, 3071*, 158-168, 1997.

Heinz, D., Chang, C.-I. and Althouse, M.L.G., Fully Constrained Least-Squares Based Linear Unmixing, *International Geoscience Remote Sensing Symposium, 99*, 1401-1403, 1999.

Hinnrichs, M., Infrared Hyperspectral Imaging Sensor for Gas Detection, *Proc. SPIE, 4132*, 344-355, 2000.

Ifarraguerri, A. and Chang, C.-I., Unsupervised Hyperspectral Image Analysis with Projection Pursuit, *IEEE Trans. Geosci. Remote Sensing, 38*, 2529-2538, 2000.

Kulp, T.J., Powers, P.E. and Kennedy, R., Remote Imaging of Controlled Gas Releases Using Active and Passive Infrared Imaging Systems, *Proc. SPIE, 3061*, 269-278, 1997.

Kuo, S.D., Schott, J.R. and Chang, C.Y., Synthetic Image Generation of Chemical Plumes for Hyperspectral Applications, *Opt. Eng., 39*, 1047-1056, 2000.

Lawson, C.L. and Hanson, R.J., *Solving Least Squares Problems*, Prentice Hall, Englewood Cliffs, NJ, 1974.

Lay, L.T. and Plummer, G.M., U.S. EPA Application of FTIR for Determination of Title III Air Toxic Emissions, *85th Annual Meeting of A&WMA,* Kansas City, MO, June 1992.

Lisowski, J.J. and Cook, C.A., A SVD Method for Spectral Decomposition and Classification of ARES Data, *Proc. SPIE, 2821*, 14-29, 1996.

Lucey, P.G., Williams, T.J., Winter, M. and Winter, E.M., Performance of the AHI Airborne Thermal Infrared Hyperspectral Imager, *Proc. SPIE, 4132*, 186-194, 2000.

Marinelli, W.J., Gittins, C.M., Gelb, A.H. and Green, B.D., Tunable Fabry-Perot Etalon-Based Long-Wavelength Infrared Imaging Spectroradiometer, *Applied Optics, 38*, 2594-2604, 1999.

NOAA, http://www.arl.noaa.gov/ready-bin/profileafile.pl?metdata=EDAS

Plummer, G.M. and Lay, L.T., Technical Aspects of EPA's FTIR Development Project, *85th Annual Meeting of A&WMA*, Kansas City, MO, June 1992.

Polak, M.L., Hall, J.L. and Herr, K.C., Passive Fourier-Transform Infrared Spectroscopy of Chemical Plumes: An Algorithm for Quantitative Interpretation and Real-Time Background Removal, *Applied Optics, 34*, 5406-5412, 1995.

Pratt, W.K., *Digital Image Processing*, John Wiley and Sons, New York, 1978.

Press, W.H., Flannery, B.P., Teukolsky, S.A. and Vetterling, W.T., *Numerical Recipes, The Art of Scientific Computing*, Cambridge University Press, New York, 1990.

Ramsey, M.S. and Christensen, P.R., Mineral Abundance Determination: Quantitative Deconvolution of Thermal Emission Spectra, *J. Geophys.Res., 103*, 577-596, 1998.

Roger, R.E., Principal Components Transform with Simple, Automatic Noise Adjustment, *Int. J. Remote Sensing, 17*, 2719-2727, 1996a.

Roger, R.E., Sparse Inverse Covariance Matrices and Efficient Maximum Likelihood Classification of Hyperspectral Data, *Int. J. Remote Sensing, 17*, 589-613, 1996b.

Rolph, G.D., NCEP Model Output – EDAS Archive, TD-6141, National Climatic Data Center, Asheville, NC, August 1998.

Rothman, L.S., Rinsland, C.P., Goldman, A., Massie, S.T., Edwards, D.P., Flaud, J.-M., Perrin, A., Camy-Peyret, C., Dana, V., Mandin, J.-Y., Schroeder, J., McCann, A., Gamache, R.R., Wattson, R.B., Yoshino, K., Chance, K.V., Jucks, K.W., Brown, L.R., Nemtchinov, V. and Varanasi, P., The HITRAN Molecular Spectroscopic Database and HAWKS (HITRAN Atmospheric Workstation): 1996 Edition, *J. Quant. Spectrosc. Radiat. Transfer, 60*, 665-710 (1998).

Rousseeuw, P.J. and Leroy, A.M., *Robust Regression and Outlier Detection*, John Wiley and Sons, New York, 1987.

Sandsten, J., Edner, H. and Svanberg, S., Gas Imaging by Infrared Gas-Correlation Spectrometry, *Opt. Lett., 21*, 1945-1947, 1996.

Sandsten, J., Weibring, P., Edner, H. and Svanberg, S., Real-Time Gas-Correlation Imaging Employing Thermal Background Radiation, *Optics Express, 6*, 92-103, 2000.

Schweizer, S.M. and Moura, J.M.F., Hyperspectral Imagery: Clutter Adaptation in Anomaly Detection, *IEEE Trans. Inform. Theory, 46*, 1855-1871, 2000.

Schweizer, S.M. and Moura, J.M.F., Efficient Detection in Hyperspectral Imagery, *IEEE Trans. Image Processing, 10*, 584-597, 2001.

Settle, J.J., On the Relationship Between Spectral Unmixing and Subspace Projection, *IEEE Trans. Geosci. Remote Sensing, 34*, 1045-1046, 1996.

Stocker, A.D. and Schaum, A.P., Application of Stochastic Mixing Models to Hyperspectral Detection Problems, *Proc. SPIE 3071*, 47-60, 1997.

Theiler, J., Lavenier, D.D., Harvey, N.R., Perkins, S.J. and Szymanski, J.J., Using Blocks of Skewers for Faster Computation of Pixel Purity Index, *Proc. SPIE, 4132*, 61-71, 2000.

Tompkins, S., Mustard, J.F., Pieters, C.M. and Forsyth, D.W., Optimization of Endmembers for Spectral Mixture Analysis, *Remote Sens. Environ., 59*, 472-489, 1997.

U.S. Standard Atmosphere, 1976, NOAA-S/T 76-1562, National Oceanic and Atmospheric Administration, Washington D.C., October 1976.

Warren, D.W., Hackwell, J.A. and Gutierrez, D.J., Compact Prism Spectrographs Based on Aplanatic Principles, *Opt. Eng., 36*, 1174-1182, 1997.

Young, S.J., Nonisothermal Band Model Theory, *J. Quant. Spectrosc. Radiat. Transfer, 18*, 1-28 (1977).

Young, S.J., Johnson, B.R. and Hackwell, J.A., An Inscene Atmospheric Compensation Method for Thermal Infrared Hyperspectral Imagery, Submitted for publication in *J.Geophys. Res.*

Yu, X., Hoff, L.E., Reed, I.S., Chen, A.M. and Stotts, L.B., Automatic Target Detection and Recognition in Multiband Imagery: A Unified ML Detection and Estimation Approach, *IEEE Trans. Image Processing, 6*, 143-156, 1997.

Appendix 1—Linear Least-Squares Regression

A fundamental procedure in hyperspectral data analysis is the modeling of a pixel spectrum as a linear combination of target and background spectra

$$L(\lambda)=\sum_{n=1}^{N}\alpha_n T_n(\lambda)+\sum_{m=1}^{M}\beta_m B_m(\lambda)+\delta(\lambda). \tag{1}$$

$L(\lambda)$ is a pixel spectrum, λ is wavelength, $T_n(\lambda)$ ($n = 1, ..., N$) is a set of target spectra, $B_m(\lambda)$ ($m = 1, ..., M$) is a set of background basis spectra, α_n and β_m are amplitude coefficients, and $\delta(\lambda)$ is the residual spectrum. Target spectra might be spectral gas absorption coefficients $k(\lambda)$ or material reflectance spectra $\rho(\lambda)$. Background spectra might be pixel spectra drawn directly from the imagery, spectra constructed by endmember extraction algorithms, spectra derived from clustering algorithms, eigenvector representations of any of the above, or eigenvector spectra of various spectral covariance matrices constructed from the imagery.

Equation (1) represents a set of linear equations, one for each spectral channel λ_j ($j = 1, ..., J$). When $J > N + M$, the amplitude coefficients can be determined by a variety of regression procedures. Two regression approaches are considered here. In the first approach, no constraints are placed on the amplitude coefficients. In the second approach, various constraints are placed on the target and background amplitudes. Unconstrained regression is also known as multivariate linear least-squares regression and multiple least-squares regression. Either form of regression, particularly in the geological community, is also known as *spectral unmixing* or *demixing*.

Recasting in matrix-vector notation:

$$\mathbf{Y}=\left[L(\lambda_1)\cdots L(\lambda_J)\right] \tag{2}$$

$$\mathbf{X}=\left[\alpha_1\cdots\alpha_N\,\beta_1\cdots\beta_M\right]^{\mathrm{T}} \tag{3}$$

$$\mathbf{A}=\begin{bmatrix} T_1(\lambda_1)\cdots T_N(\lambda_1)\;B_1(\lambda_1)\cdots B_M(\lambda_1) \\ \vdots \qquad\qquad\qquad \vdots \\ T_1(\lambda_J)\cdots T_N(\lambda_J)\;B_1(\lambda_J)\cdots B_M(\lambda_J) \end{bmatrix} \tag{4}$$

$$\mathbf{d}=\left[\delta(\lambda_1)\cdots\delta(\lambda_J)\right]^{\mathrm{T}}. \tag{5}$$

Y is a column-vector representation of $L(\lambda)$. **X** is column-vector representations of the amplitude coefficients α_n and β_m. **A** is a matrix representation of the target and background spectra. **d** is a column-vector representation of the residual spectrum $\delta(\lambda)$. With these correspondences, (1) becomes

$$\mathbf{Y} = \mathbf{AX} + \mathbf{d}. \tag{6}$$

In addition to **Y**, assume the covariance matrix $\mathbf{C_Y}$ describing error estimates of, and correlations between, the elements of **Y** is known.

<u>Unconstrained Regression.</u> The unconstrained regression solution to (6) is obtained by minimizing the magnitude of the error-weighted residual vector **d** with respect to variations in **X**. The error-weighted magnitude R is defined by

$$R^2 = \mathbf{d}^{\mathrm{T}}\mathbf{C}_{\mathbf{Y}}^{-1}\mathbf{d} = (\mathbf{Y} - \mathbf{AX})^{\mathrm{T}}\mathbf{C}_{\mathbf{Y}}^{-1}(\mathbf{Y} - \mathbf{AX}). \tag{7}$$

Minimization of R by $dR/d\mathbf{X} = 0$ yields the *normal equation*:

$$\left(\mathbf{A}^{\mathrm{T}}\mathbf{C}_{\mathbf{Y}}^{-1}\mathbf{A}\right)\mathbf{X} = \mathbf{A}^{\mathrm{T}}\mathbf{C}_{\mathbf{Y}}^{-1}\mathbf{Y}, \tag{8}$$

from which the formal solution,

$$\mathbf{X} = \left(\mathbf{A}^{\mathrm{T}}\mathbf{C}_{\mathbf{Y}}^{-1}\mathbf{A}\right)^{-1}\mathbf{A}^{\mathrm{T}}\mathbf{C}_{\mathbf{Y}}^{-1}\mathbf{Y}, \tag{9}$$

is obtained. The errors of, and correlations between, the elements of the solution vector **X** are described by the covariance matrix

$$\mathbf{C_X} = \left(\mathbf{A}^{\mathrm{T}}\mathbf{C}_{\mathbf{Y}}^{-1}\mathbf{A}\right)^{-1}. \tag{10}$$

If the covariance matrix $\mathbf{C_Y}$ is not known, the regression is carried out with the identity matrix $\mathbf{C_Y} = \mathbf{I}$ and $\mathbf{C_X}$ is approximated by

$$\mathbf{C_X} = \sigma^2\left(\mathbf{A}^{\mathrm{T}}\mathbf{A}\right)^{-1}, \tag{11}$$

where σ is the magnitude of the residual vector defined by

$$\sigma = \sqrt{R^2 / J}. \tag{12}$$

An option for σ^2 is the unbiased estimate of the noise variance

$$s = \sqrt{R^2 / \nu}\,, \tag{13}$$

where

$$\nu = J - (M + N) \tag{14}$$

is the number of degrees of freedom for the regression. σ is used here to report the error of the fit.

In the current application, $\mathbf{C}_\mathbf{Y}$ represents sensor noise and can be obtained from radiance calibration data. *Roger* [1996b] observes that an approximation to the inverse of the sensor noise covariance matrix $\mathbf{C}_\mathbf{Y}^{-1}$ is obtained by retaining only the diagonal elements of the inverse of the scene clutter covariance matrix $\mathbf{C}^{-1}$. Despite the availability of $\mathbf{C}_\mathbf{Y}$, error estimates are obtained in the current work from (11) and (12) because this approach gives slightly more conservative (*i.e.*, slightly larger) error estimates.

In addition to solution of the unconstrained regression problem by use of the normal equation (NEQ), at least four other methods of solution are employed. The columns of $\mathbf{A}$ comprise a set of vectors. Gram-Schmidt orthogonalization (GSO) can be applied to this set to generate a set of orthogonal filter vectors $\mathbf{F}_n$ ($n = 1, ..., N + M$) that yield the $\mathbf{X}$ coefficients by $X_n = \mathbf{F}_n \cdot \mathbf{Y}$. The application requires $N + M$ orthogonalizations with each column of $\mathbf{A}$ iteratively placed in last position. The modified Gram-Schmidt procedure described by *Lawson and Hanson* [1974, p. 129] is recommended for improved numerical accuracy. Singular-value decomposition (SVD) can also be employed [*Press et al.*, 1990, p. 52, 515]. Orthogonal subspace projection (OSP) [*Harsanyi and Chang*, 1994] and orthogonal background suppression (OBS) [*Hayden et al.*, 1996] provide two other filter-vector approaches to the solution. These four implementations are described for $\mathbf{C}_\mathbf{Y} = \mathbf{I}$. For general $\mathbf{C}_\mathbf{Y}$, the implementations need to be made against the *whitened* form of (6)

$$\left(\mathbf{C}_\mathbf{Y}^{-1/2}\right)^\mathrm{T} \mathbf{Y} = \left[\left(\mathbf{C}_\mathbf{Y}^{-1/2}\right)^\mathrm{T} \mathbf{A}\right] \mathbf{X}\,. \tag{15}$$

The matrix square root is defined by [*Pratt*, 1978, p. 660]

$$\mathbf{C}_\mathbf{Y}^{-1} = \mathbf{C}_\mathbf{Y}^{-1/2}\left(\mathbf{C}_\mathbf{Y}^{-1/2}\right)^\mathrm{T} \tag{16}$$

and computed by

$$\mathbf{C}_\mathbf{Y}^{-1/2} = \mathbf{K}\mathbf{E}^{1/2}\,, \tag{17}$$

where **K** and **E** are the eigenvectors and eigenvalues of $\mathbf{C}_{\mathbf{Y}}^{-1}$. (**K** and **E** can be calculated efficiently with SVD methods. When applied to a covariance matrix, the left- and right-eigenvectors are identical, and singular values are actually eigenvalues.) It was determined that all of these implementations, with the exception of OSP, are equivalent when applied to SEBASS data. The SVD implementation is robust against an ill-conditioned **A**, but no ill condition has ever arisen in SEBASS data. The OSP implementation employs an inordinate amount of computation [*Settle*, 1996]. Possibly because of round-off errors generated by this large amount of computation, unacceptably large error estimates for **X** are often obtained with OSP.

Unconstrained regressions in the current work were carried out with a filter-vector implementation of SVD. Following *Press et al.* [1990, p. 52], working with the whitened equation (15) and rearranging the result to effect a filter-vector implementation yields

$$X_n = \mathbf{F}_n \cdot \mathbf{Y}\,, \tag{18}$$

where $\mathbf{F}_n$ is the filter vector

$$\mathbf{F}_n = \mathbf{C}_{\mathbf{Y}}^{-1/2} \sum_{i=1}^{N+M} \left(\frac{V_{ni}}{s_i} \right) \mathbf{U}_i\,. \tag{19}$$

The elements of $\mathbf{C}_{\mathbf{X}}$ are

$$C_X(n,m) = \sum_{i=1}^{N+M} \frac{V_{ni} V_{mi}}{s_i^2}\,. \tag{20}$$

U and **V** are the left- and right-eigenvectors arrays of the matrix $\left(\mathbf{C}_{\mathbf{Y}}^{-1/2}\right)^{\mathrm{T}} \mathbf{A}$. s_i are the singular values.

<u>Spectral Matched Filters.</u> Spectral matched filtering for signal detection is common in the electrical engineering signal processing literature. Its derivation there [*e.g.*, *Pratt*, 1978, p. 560] is often from a point of view that obscures its connection to linear least-squares regression. From the regression point of view, spectral matched filtering is an unconstrained regression in which the background summation in (1) is approximated by a single term, *i.e.*, the mean scene background with fixed amplitude $\beta_1 = 1$, and in which $\mathbf{C}_{\mathbf{Y}}$ is broadened in scope and taken as the full scene clutter covariance matrix **C**. Let $\mathbf{Y}_p$ be a column vector representation of the spectrum at the pth pixel. **C** is the square $J \times J$ matrix

$$\mathbf{C} = \frac{1}{P}\sum_{p=1}^{P}\left[\mathbf{Y}_p - \overline{\mathbf{Y}}\right]^{\mathrm{T}}\left[\mathbf{Y}_p - \overline{\mathbf{Y}}\right] = \frac{1}{P}\sum_{p=1}^{P}\mathbf{Y}_p{}^{\mathrm{T}}\mathbf{Y}_p - \overline{\mathbf{Y}}\overline{\mathbf{Y}}^{\mathrm{T}}, \tag{21}$$

where $\overline{\mathbf{Y}}$ is the mean scene spectrum

$$\overline{\mathbf{Y}} = \frac{1}{P}\sum_{p=1}^{P}\mathbf{Y}_p\,, \tag{22}$$

and $\overline{\mathbf{Y}}\overline{\mathbf{Y}}^{\mathrm{T}}$ is the outer product of the mean spectrum with itself. The summations in (21) and (22) are over all, or some selected set, of pixels in the image. P is the number of pixels. J is the number of spectral channels. With the coarse approximation that the background under a pixel is the mean scene spectrum, spectral matched filtering is rarely suitable for quantitative assessment of signal strength. In gas detection, for example, it is not unusual to obtain a large positive (negative) detection signal on a pixel when the pixel spectrum clearly shows the gas in absorption (emission). Nevertheless, spectral matched filtering is a proven powerful and robust detection technique that can be applied with a minimal amount of preparation.

With the mean scene spectrum used as the background and **C** as the error-weighting function, the solution vector and error covariance matrix for **X** are

$$\mathbf{X} = \left(\mathbf{A}^{\mathrm{T}}\mathbf{C}^{-1}\mathbf{A}\right)^{-1}\mathbf{A}^{\mathrm{T}}\mathbf{C}^{-1}\left(\mathbf{Y} - \overline{\mathbf{Y}}\right) \tag{23}$$

and

$$\mathbf{C}_{\mathbf{X}} = \left(\mathbf{A}^{\mathrm{T}}\mathbf{C}^{-1}\mathbf{A}\right)^{-1}, \tag{24}$$

where now **A** contains only target spectra. Rearrangement of (23) allows the solution to be written as

$$\mathbf{X} = \mathbf{F}^{\mathrm{T}}\left(\mathbf{Y} - \overline{\mathbf{Y}}\right), \tag{25}$$

where

$$\mathbf{F} = \left(\mathbf{C}^{-1}\mathbf{A}\right)\mathbf{C}_{\mathbf{X}} \tag{26}$$

is a matrix whose columns are the spectral matched filters. It is traditional to report spectral matched filtering results as the signal-to-noise ratio (SNR) for detection of the nth target. This ratio is

$$SNR = X_n / \sigma_{X_n} , \tag{27}$$

where

$$\sigma_{X_n} = \sqrt{C_X(n,n)} . \tag{28}$$

σ_{X_n} is an estimate of the minimum detectable quantity (*MDC*), the minimum signal strength required for a detection SNR of unity. Additionally, detection on a set of targets is most often implemented one-target-at-a-time. That is, **A** contains only a single column. This is an acceptable approach only if the target spectra do not overlap significantly. All of the work here on multiple-gas detection is carried out with a full **A** matrix.

Constrained Regression. For some problems, it is necessary to place constraints on the amplitude coefficients α_n and β_m to impose physically meaningful conditions. Two constraints are relevant to the current work. First, except under unusual conditions, we expect to see all gases simultaneously either in emission or in absorption; that is, all amplitude coefficients α_n should have the same sign. Second, when the background is expanded on a set of radiance spectra drawn from the imagery, on a set of clusters constructed from the imagery, or on a set of endmembers extracted from the imagery, we expect the amplitude coefficients β_m to be nonnegative.

At least two situations exist where the same-sign constraint on gas contrast radiance does not apply and in which it is possible to see some gases in absorption and others in emission. Neither occurs in the current study. Consider gases flowing over an underlying silicate surface. If the dominant spectral feature for one gas lies directly over the depressed emissivity feature between ~8.0 and ~9.6 μm, and the dominant spectral feature of another gas does not, then there will be a narrow range of temperature contrast between the plume and the surface that renders the first gas in emission and the second in absorption. The second situation arises if two gases are emitted from a hot stack and one of them is also an ambient gas that is rapidly entrained with the stack gases. The contrast radiance for the nonambient gas is $C_1 = D\rho_{P1} (T_P - T_S)$, where D is the LOS distance through the plume, ρ_{P1} is the gas concentration in the plume from the stack contribution, T_P is the plume temperature, and T_S is the brightness temperature of the underlying surface. The contrast radiance for the ambient gas is $C_2 = D\,[\rho_{P2} (T_P - T_S) + \rho_{A2} (T_P - T_A)]$, where ρ_{P2} and ρ_{A2} are the stack and ambient entrainment contributions to the plume concentration, and T_A is the ambient air temperature. If $T_S > T_P$, C_1 will be negative. The first term of C_2 will also be negative, but the second term will always be positive or zero. If the stack contribution, ρ_{P2}, is small, the second term can dominate and produce a positive contrast.

Constrained regressions were carried out here with the NNLS algorithm described by *Lawson and Hanson* [1974, p. 158]. (A similar algorithm is available in the commercial IMSL mathematical library with [*Hanson*, 1986] as its citation.) The NNLS algorithm solves the linear least-squares regression problem with the inequality constraint that all coefficients, α_n and β_m alike, be nonnegative. The *same-sign* constraint on the target coefficients is handled by solving the constrained problem twice. The first solution is a direct application of NNLS. The second solution is obtained by changing the sign of all target column vectors in **A**. The result with the smaller regression residual is taken as the solution. NNLS constrained regression with error estimation, and with

the double application required to impose the same-sign constraint, is nearly 40 times slower than unconstrained regression. Additionally, the covariance matrix $\mathbf{C_X}$ cannot be precomputed. It is not known beforehand which members of the background set will survive the regression. Fitting residuals are also necessarily larger than those obtained in unconstrained regression.

Other solutions to the regression problem with nonnegative amplitude coefficients are obtained in an iterative application of unconstrained regression. First, the unconstrained solution is obtained. Column vectors of **A** that correspond to negative solution elements X_c are deleted. *Ramsey and Christensen* [1998] delete all of them at once. *Heinz et al.* [1999] delete only the most offensive one (after a suitable weighting). In either case, unconstrained regression is then reapplied. The process is repeated until no negative X_c remains. Although this method generally selects a final basis set that is different from the NNLS set, the residual of the fit is usually nearly as good. An objection to this method is that it is even slower than the NNLS algorithm.

Appendix 2—Statistical Tests of Regression

Test for Normal Distribution. Several statistical tests are used in the current work to assess the quality of regression. All of these tests are based on the assumption of normal random deviates. Conformity to this assumption is tested with the Kolmogorov-Smirnov procedure [*Press et al.*, 1990, p. 472] of comparing the cumulative probability distribution of a regression residual spectrum $\delta(\lambda)$ with the cumulative probability distribution for the normal distribution. The cumulative distribution of the residual spectrum is

$$P_C(j) = j/J \qquad j = 1, 2, \ldots, J \tag{1}$$

at the abscissa positions

$$Z(j) = \delta_S(j)/\sigma \qquad j = 1, 2, \ldots, J\,. \tag{2}$$

$\delta_S(j)$ is the array of residual spectrum elements $\delta(\lambda_j)$ sorted by ascending value. σ is the RMS value of the spectrum. The cumulative normal distribution is

$$P_C(j) = P[Z(j)] \qquad j = 1, 2, \ldots, J\,, \tag{3}$$

where

$$P(Z) = \frac{1}{\sqrt{2\pi}} \int_{-\infty}^{Z} e^{-t^2/2} dt\,. \tag{4}$$

The Kolmogorov-Smirnov statistic D_{KS} is the maximum absolute difference between distributions (1) and (3). For each j, the value of P_C from (3) needs to be compared to the value from (1) at both j and $j-1$. For $j = 1$, the second comparison is with zero. The maximum absolute difference is tested for significance by

$$P_{KS} = Q_{KS}\left(\sqrt{J}\, D_{KS}\right), \tag{5}$$

where

$$Q_{KS}(\gamma)=2\sum_{i=1}^{\infty}(-1)^{i-1}e^{-2i^2\gamma^2}\,. \qquad (6$$

P_{KS} ranges from zero to unity as the agreement with a normal distribution improves. Application of this test is made in Subsection 6.6.

<u>*T*-Test for Significance of *X*.</u> A standard (Student's) *T*-Test is used to assess the significance of a regression coefficients X with respect to its error estimate σ_X. The test statistic is

$$Z=\frac{X}{\sigma_X}\sqrt{\frac{\nu}{J}}=SNR\sqrt{\frac{\nu}{J}}, \qquad (7$$

where ν is the degrees of freedom of the regression $\nu = J - N - M$. The radical factor in (7) adjusts the standard error estimate to be an unbiased estimate (see Equation 13 of Appendix 1). The probability that a value greater than or equal to X could have been obtained by statistical fluctuations for the case that its true value is zero is $2[1-T(Z|\nu)]$, where $T(Z|\nu)$ is the cumulative *T*-distribution

$$T(Z|\nu)=\frac{\Gamma[(\nu+1)/2]}{\sqrt{\pi\nu}\,\Gamma(\nu/2)}\int_{-\infty}^{Z}\left(1+\frac{t^2}{\nu}\right)^{-(\nu+1)/2}dt=1-\frac{1}{2}I_{\frac{\nu}{\nu+Z^2}}\left(\frac{\nu}{2},\frac{1}{2}\right). \qquad (8)$$

$I_Z(a,b)$ is the incomplete beta function [*Press et al.*, 1990, p. 168]. The probability that X is significant is therefore

$$P_T=1-2[1-T(Z|\nu)]=2T(Z|\nu)-1. \qquad (9)$$

For all applications in this work, ν is large enough that $T(Z|\nu)$ is adequately approximated by the normal distribution (4).

<u>*T*-Test for Significance of Change in *X*.</u> A *T*-Test can be made to test whether a coefficient has changed between two regressions. Let X_1, σ_{X_1} and X_2, σ_{X_2} be the coefficients and standard errors obtained in the two regressions. The test statistic is

$$Z=\frac{|X_1-X_2|}{\sqrt{(J/\nu_1)\sigma_{X_1}^2+(J/\nu_2)\sigma_{X_2}^2}}\,. \qquad (10)$$

The probability that X_1 and X_2 are different is given by (9) with $\nu = \nu_1 + \nu_2$.

Goodness of Fit F-Test. A measure of the *goodness of fit* of a regression is given by an F-Test [*Rousseeuw and Leroy*, 1987] with the statistic

$$F_R = \frac{R^2/(N+M)}{\left(1-R^2\right)/(J-N-M)}. \tag{11}$$

R is the *multiple regression coefficient.* Its square (the *coefficient of determination*) is

$$R^2 = 1-\sigma^2 \Bigg/ \left(\frac{1}{J}\sum_{j=1}^{J} Y_j^2 \right), \tag{12}$$

where **Y** is the data spectrum. The measure of the goodness of fit is

$$P_R = 1 - P_F\left(F_R \middle| N+M, J-N-M\right), \tag{13}$$

where $P_F(F,\nu_1,\nu_2)$ is the cumulative F-distribution

$$P_F\left(F \middle| \nu_1,\nu_2\right) = I_{\frac{\nu_2}{\nu_2+\nu_1 F}}\left(\frac{\nu_2}{2},\frac{\nu_1}{2}\right), \tag{14}$$

and $I_z(a,b)$ is the incomplete beta function.

In the current study, this test is not particularly revealing. The total data spectrum consists of a weak trace-gas signal superimposed on a strong thermal background signal. For any reasonable estimate of the thermal signal, regardless of the target gas selection, the test assesses the goodness of fit as excellent. Here, the test was heuristically modified by replacing the total signal **Y** with the gas contrast spectrum (equation 40 of the main text). With this modification, the test assesses the goodness of fit provided by the selection of gases. For all regression carried out here, the final selection of gases gave goodness-of-fit probability $P_R = 1.00$.

Addition F-Test. The significance of changing the number of target or background terms in a regression can be assessed with an F-Test using a statistic derived from the change in the regression residual [*Bevington*, 1969]. The following development is for including additional terms. Application for deleting terms obtains by changing the subscripts 1 and 2. The F-statistic is

$$F_\chi = \frac{\left(\sigma_1^2 - \sigma_2^2\right)/(\nu_1-\nu_2)}{\sigma_2^2/\nu_2}. \tag{15}$$

σ_1 is the regression residual that results with N_1 targets and M_1 backgrounds. σ_2 is the regression residual for N_2 targets and M_2 backgrounds. In unconstrained regression, $\sigma_2 \leq \sigma_1$. The degrees of freedom for the two regressions are $\nu_1 = J - N_1 - M_1$ and $\nu_2 = J - N_2 - M_2$. The test requires

$$N_2 + M_2 > N_1 + M_1 \tag{16}$$

so that $\nu_1 - \nu_2 > 0$. This test is most commonly used to assess the addition of a single new term. Then, $N_2 = N_1 + 1$ and $\nu_1 - \nu_2 = 1$. The measure of significance of the addition of terms is

$$P_\chi = 1 - P_F\left(F_\chi \middle| \nu_1 - \nu_2, \nu_2\right), \tag{17}$$

where $P_F\left(F \middle| \nu_1, \nu_2\right)$ is given by (14).

All of these tests except the addition F-Test are directly applicable to both constrained and unconstrained regressions. The addition F-Test is not applicable to constrained regressions. In constrained regressions, N is not necessarily the number of gases in the target suite, and M is not necessarily the number of background spectra in the basis set. N is the number of gases that survive the same-sign constraint with nonzero coefficients, and M is the number of backgrounds that survive with positive coefficients. Amplitude coefficients of zero do not contribute to a reduction in the degrees of freedom of the regression. This result is readily established by noting that an *unconstrained* regression using only the surviving targets and backgrounds will give the same result as the constrained regression. The upshot is that the condition (16) is not necessarily satisfied. For example, the addition of a single gas to the target suite might change the number of backgrounds used in the regression so that the difference $\nu_1 - \nu_2$ is zero or negative. This condition destroys the validity of the statistic (15). Even if the number of backgrounds does not change, the set of backgrounds selected might change. This change also destroys the validity of the test. Additionally, in constrained regression, there is no guarantee that $\sigma_2 \leq \sigma_1$. Application of the addition F-Test is made in Subsection 6.6 to assess the improvement in unconstrained regression as the number of background cluster spectra is increased.